Ion Transport in Nano-Engineered Ion Exchange Membranes and Their Applications for Redox Flow Batteries

By

TONGSHUAI WANG

B.S & M.S, East China University of Science and Technology, 2008

THESIS

Submitted in partial fulfillment of the requirements
For the degree of Doctor of Philosophy in Chemical Engineering
in the Graduate College of the
University of Illinois at Chicago, 2020
Chicago, Illinois

Defense Committee:

Dr. Sangil Kim, Chair and Advisor, Department of Chemical Engineering
Dr. Vikas Berry, Department of Chemical Engineering
Dr. Brian P. Chaplin, Department of Chemical Engineering
Dr. Said Al-Hallaj, Department of Chemical Engineering & AllCell Technologies LLC
Dr. Jordi Cabana, Department of Chemistry

ACKNOWLEDGMENTS

My deepest gratitude goes first to my advisor, Dr. Sangil Kim, who expertly guided me and financially supported me through my Ph.D. study. This thesis would not have been possible without the help, support, and patience from Dr. Kim. Over the years, Dr. Kim continually and convincingly conveyed a spirit of adventure regarding research and scholarship, which is the major driving force through my graduate career at the University of Illinois at Chicago. From him, I learned how to perform research as a real scientist instead of a technician.

I am extremely grateful to my thesis committee members, Dr. Brian P. Chaplin, Dr. Vikas Berry, Dr. Said Al-Hallaj, and Dr. Jordi Cabana. Dr. Chaplin opened the electrochemistry world to me. From his class, I learned valuable knowledge about electrochemistry, which is greatly beneficial to understand the systems used in my research. Dr. Berry provided his insightful suggestions and scientific guidance on 2D materials. I also thank Dr. Berry for providing high-quality graphene that is substantial for my experiment. Dr. Al-Hallaj let me have a better understanding of the real battery industry as well as a deeper comprehension of the structure of industrial-scale batteries. Dr. Cabana provided the instruction on the fundamentals of lithium-sulfur batteries and offered his lab space for coin cell assembly.

I would like to thank our collaborators from Rensselaer Polytechnic Institute (RPI) and Lawrence Livermore National Laboratory (LLNL). Dr. Chulsung Bae and his group members in RPI provide important research materials and shared their knowledge of material properties. Dr. Jianchao Ye in LLNL offered me a valuable opportunity for the summer internship in the national laboratory and taught me practical experiment skills.

My appreciation also extends to my laboratory colleagues. I sincerely thank Aaditya Pendse, who joined the group together with me and gave me continuous support and encouragement over the years. I am thankful to Jannice Lee and Yuechen Gao, who assisted my experiments and manuscript revising. Thanks also to other lab members and those who have helped me in the experiment and studying: Victor Nieto, Kun Wang, Donglin Li, Purnima Barua, Hyang Seol, Li Si Lai, Doo Sung Hwang, and Allison Nordvall.

Thanks to all my friends and my parents for encouraging, motivating, and inspiring me, especially during difficult times.

Finally, I would like to acknowledge the support from the National Science Foundation and the Department of Energy for funding my research projects and conference expenses.

CONTRIBUTION OF AUTHORS

Chapter 1 represents an overview of my dissertation, which also includes the research objectives and sets up the outline of this dissertation. Chapter 2 is a literature review where the state of knowledge is presented, and the significance of my research questions is highlighted. Chapter 3 represents two related works, one is published and the other is under revision, in which I was the first author and major contributor to the research. My research mentor, Dr. Sangil Kim conceived the project and contributed to the manuscript revision and scientific discussion. Our collaborators from Dr. Chulsung Bae's group in Rensselaer Polytechnic Institute provide the materials and contributed to polymer characterizations as well as manuscript revision. Dr. Klaus-Dieter Kreuer and Andreas Munchinger from Max-Planck-Institute, Germany, contribute to the SAXS measurement, data analysis, and scientific discussion. Dr. Yoong-Kee Choe from AIST, Japan, contributed to DFT calculation, data analysis, and scientific discussion. Chapter 4 represents a published work of which I was the first author and one of the major contributors to the research. Collaborators in Dr. Young Moo Lee's group from Hanyang University synthesized the membrane, performed the AFM measurements and membrane mechanical tests. Dr. Sangil Kim conceived the project and contributed to the manuscript revision and scientific discussion. Chapter 5 represents a manuscript of which I am the first author and major contributor to the research. Dr. Sangil Kim conceived the project and contributed to manuscript preparation, revision, and scientific discussion. Collaborators from Dr. Chulsung Bae's group in RPI contributed to polymer synthesis and scientific discussion. Chapter 6 represents a manuscript of which I am the first author and one of the major contributors to the research. Dr. Sangil Kim conceived the project and contributed to manuscript preparation, revision, and scientific discussion. Dr. Jianchao Ye, Dr. Shiwei Liang and other collaborators from LLNL contributed to the concept design, fabrication, and manuscript preparation, and scientific discussion, Chapter 7 represents a concluding remark of the dissertation and the future directions of this field are also discussed.

TABLE OF CONTENT

LIST OF TABLES

LIST OF TABLES_CONTINUED

LIST OF FIGURES

LIST OF FIGURES---continued

LIST OF FIGURES---continued

LIST OF ABBREVIATIONS

AEM	Anion Exchange Membrane
AFM	Atomic Force Microscopy
CNT	Carbon Nanotube
CV	Cyclic Voltammetry
CE	Coulombic Efficienc
DFT	Density Functional Theory
EE	Energy Efficiency
EIS	Electrochemical Impedance Spectroscopy
LIB	Lithium Ion Battery
LSB	Lithium Sulfur Battery
LIPS RFB	Lithium Polysulfide Redox Flow Battery
MWCO	Molecular Weight Cutoff
MWCNT	Multi-wall Carbon nanotube
OCP	Open Circuit Potential
PEM	Proton Exchange Membrane
RFB	Redox Flow Battery
SAXD	Small Angle X-Ray Diffraction
SEM	Scanning Electron Microscopy
TGA	Thermogravimetric Analysis
VE	Voltage Efficieny
VRFB	Vanadium Redox Flow Battery

I. INTRODUCTION

1.1 Background

The ever-growing demand for electricity necessities the development of energy storage technologies to efficiently utilize renewable energies. The proverbial energy storage technology is the battery, which generally conducts electrons extracted from a solid-state material through a precisely defined conduit which creates electricity. However, the use of existing batteries such as lithium-ion batteries (LIBs) on the scale needed for the electrical power grid is not practical because of the lack of flexibility in cell design and unsatisfying durability [1, 2]. Redox flow batteries (RFBs) offer an alternative for energy storage and have attracted recent attention due to design flexibility in decoupling power and energy capacity, easy scalability, and their safe operation at large-scale [3, 4].

As the core element in most RFBs systems, ion exchange membranes (IEMs) play a critical role in preventing electrolyte crossover between the catholyte and anolyte, while still allowing the transport of charged ions (e.g. H^+, SO_4^{2-}, Li^+) to complete the circuit. Over the past decade, IEMs have been studied extensively for the separation of redox-active species, as well as for charge carrier transfer during battery operation. Commercial perfluorinated membranes, such as DuPont's Nafion®, have been most widely investigated and implemented as membrane separators in RFBs due to their favorable chemical stability and commercial availability. However, Nafion® membranes can consume about 41% of the RFB stack's total cost due to their high cost [5]. A relatively high active species cross-over flux (poor ion selectivity) is another critical issue with the Nafion® membranes, leading to a lower coulombic efficiency (CE) and severe capacity loss in the standby state [6]. Numerous efforts have been devoted either to modify the Nafion® or to find alternative low-cost materials [7, 8]. Nevertheless, the cost of the modified Nafion membranes is still restricted by the high price of pristine Nafion®, while the alternative membranes exhibit inferior chemical or mechanical properties. More importantly, the trade-off limitation between ionic membrane resistance and ion selectivity remains to be overcome. To successfully implement RFBs as a large-scale electrochemical storage technique, it is essential to develop superior new membranes with high ion selectivity, sufficient stability, and low-cost.

Invoked by the rapid progress in nanoscience and nanotechnology, nano-engineered membranes with the building blocks tailored on the nanometer scale have achieved progress in various fields of science and engineering, such as water treatment [9], gas separation [10] and fuel cells [11, 12]. Attributing to their unique properties, the nano-engineered membranes usually exhibit unprecedented high selectivity or permeability compared to the conventional pure polymer membranes [13]. Despite the excellent properties of nano-

engineered membranes, their potential as IEMs in the RFBs has not been fully exploited. In addition, there is a lack of fundamental understanding of the structure-performance relation of the nano-engineered membrane which has impeded the reached progress.

1.2 Research objectives

The general goal of this research is to develop high-performance nano-engineered membranes to address the current limitations of RFB technologies. To achieve this goal, not only an advance in material design and membrane fabrication is required, it is of the same importance to have a comprehensive understanding of the fundamental ion transport mechanisms. The specific objectives of this research are summarized as follows:

(1) Develop nano-engineered IEMs to overcome the trade-off limitation of conventional membranes.
The conventional IEMs used for RFBs are restricted by a trade-off between ion selectivity and permeability. To overcome this limitation, we have developed several types of IEMs with ultra-high ion selectivity using different approaches. One approach focusses on enhancing ion selectivity of the pure polymer membranes by optimizing their molecular structure, such as polymer backbone, sidechain, and ion exchange groups. In another approach, we have improved the electrochemical performance of IEMs by introducing nano-engineered selective surfaces and functional materials, such as 2D-graphene and carbon nanotubes.

(2) Investigate the structure-performance relation of the nano-engineered IEMs
A fundamental understanding of the correlation between membrane transport properties and its structure is essential for developing high-performance IEMs. In this study, we have systematically investigated the effect of membrane structure (polymer chemistry, membrane architectures, and morphologies) on the ion transport properties via various experimental and numerical methods. The membrane morphology was characterized experimentally by scanning electronic microscope (SEM), atomic force microscope (AFM), and small-angle X-ray scattering (SAXS). The ion transport properties of the membrane were measured by a number for diffusion-based measurements and electrochemical methods. Numerical methods, such as density functional theory (DFT) calculation, were also employed to help investigate the interaction between membranes and the ions species. These results lead to an in-depth understanding of the structure-performance relation of the nano-engineered IEMs and helped to provide design criteria for the development of high-performance membranes in RFB application.

(3) Examination of the membrane performance in RFB systems.

To demonstrate the effectiveness of the nano-engineered membranes, their performance was evaluated on the redox flow batteries. Due to the well-understood working mechanism and the availability of chemicals, the vanadium redox flow battery (VRFB) was chosen as a proof-of-concept system for most of our works. However, the practical application of VRFB is limited due to its relatively low energy density and high raw material cost. Therefore, we have also extended our research scope to novel non-aqueous systems that possess higher energy density and lower raw material cost, e.g. Lithium-polysulfide (Li-PS) RFBs.

1.3 Outlines of thesis

The thesis is comprised of 7 chapters in total. **Chapter 2** introduces the current state of knowledge of redox flow batteries, ion exchange membranes, transport phenomena in the membrane phase, and limitations on the developing high-performance membranes for redox flow batteries. **Chapter 3** presents the work on how to improve the electrochemical performance of VRFB cells using pure polymeric membranes that are constructed with a series of aromatic proton exchange and anion exchange polymers. The work on AEM was published in Journal of Membrane Science in 2019 entitled "*Poly(terphenylene) Anion Exchange Membranes with High Proton Conductivity and Selectivity for Vanadium Redox Flow Batteries (VRFBs)*". The results on PEM were included in a submitted article entitled "*Suppressing Vanadium Crossover Using Sulfonated Aromatic Ion Exchange Membranes for High Performance Flow Batteries*", which is currently under review. In **Chapter 4**, we further investigated the potential of using 2D inorganic/organic hybrid membranes to overcome the trade-off limitation of between ionic membrane resistance and ion selectivity. This chapter is separated into two parts. The first part comprises the work that was published in Journal of membrane science in 2019 entitled "*Selective ion transport for a vanadium redox flow battery (VRFB) in nano-crack regulated proton exchange membranes*". The concept of IEM with a nano-patterned surface layer was demonstrated in this work by using a model membrane system with nano-crack surface coatings prepared using plasma treatment. The second part of the work comprises the research progress on developing 2D graphene-coated composite membrane as well as studies on their ion transport properties and battery electrochemical performance. **Chapter 5** comprises the work on developing highly ion-selective and stable composite ion exchange membranes for non-aqueous based lithium-polysulfide batteries. Due to the limitation of the 2-dimensional membrane, **Chapter 6** further explores the possibility of achieving both high permeability and ion selectivity using a 3D nanometer-thick membrane, which could act as the ultimate membrane structure in various separation processes and electrochemical cells. The results from this work are published in Materials Horizons entitled with "*3D nm-Thin Biomimetic Membrane for Ultimate Molecular Separation*".

II. STATE OF KNOWLEDGE

2.1 The overview redox flow battery technologies

A surge of electricity generation from renewable energy sources, e.g. wind and solar powers, has been witnessed in the past decade. In a report from the World Energy Council, it is estimated that new wind power capacity will be increased to 474 GW worldwide by the end of 2020 [14]. Similarly, a 40 % increase in the photovoltaic module installations has been observed word widely in recent years [3].

Despite the significant growth in the popularity of these technologies, the capricious nature of renewable energies still results in multiple unresolved issues. For instance, the integration of intermittent power input into the electrical grid would bring extra burden and endanger the stability of the grid. Moreover, it is also difficult to coordinate the working condition of solar and wind power plants with the customers' demand. This mismatch between power generation and consumption would lead to wasted energy. In this regard, a cost-effective and efficient energy storage system becomes essential to enhance the reliability and stability of the electrical grid. Among the various energy storage methods, redox flow batteries (RFBs) have attracted tremendous attention for the large-scale stationary applications owing to their compelling features such as flexible system design, no geographical requirement, safe operation, and long cycle life[3].

As an electrochemical energy storage device, redox flow batteries can convert the chemical energy carried by the electro-active materials to electrical energy via electrochemical reaction, and vice versa. The structure and working mechanism of a typical RFB are shown in **Figure 1.** A redox flow battery mainly consists of two electrolytes tanks, separately storing the electro-active species for the positive cell and negative cells, respectively. Generally, the active materials in flow batteries are soluble in aqueous or non-aqueous solutions[14] and are stored in the electrolyte tanks. The catholyte and anolyte solution are continuously circulated using pumps through the two half-cells, which containing porous conducting electrodes to provide electron pathway and reaction sites. The two half cells are separated by an ion-selective membrane to prevent active redox-species from mixing or crossover which results in the 'chemical short-circuit' and loss of capacity [15]. It is this unique cell structure and working principle that makes RFBs superior to other energy storage technologies for large scale applications. The flexible modular design achieved by separating energy conversion from energy storage allows the RFBs to be sized for a wide spectrum of power and energy storage. Besides, using soluble redox species reduce the risk of electrodes structural deformation, which takes place frequently in batteries having solid active species with changing volume during charging and discharging. Thus, the cycle life of RFBs would not be shortened by the electrode damage or shape deformation[16].

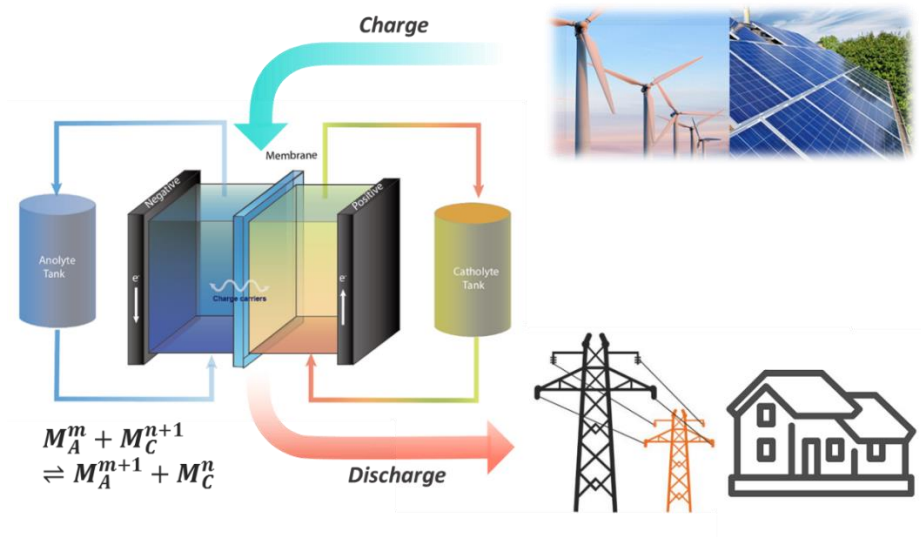

Figure 1. Schematic diagram of a typical redox flow battery composed of two electrolyte tanks, two half cells, and an ion exchange membrane [3].

In general, the RFBs can be classified into aqueous RFBs and non-aqueous RFBs depending on the types of electrolyte solutions. Historically, most RFBs utilize water-based electrolyte solution, e.g. vanadium redox flow batteries (VRFBs), as they are relatively safe, available, and compatible with a variety of redox species[16]. However, the water-based electrolyte typically has a low solubility threshold for the redox couples, which results in an unsatisfactory volumetric capacity. Besides, the energy output of aqueous RFBs is limited due to the narrow operation voltage window to prevent the water electrolysis. Thus, non-aqueous RFBs, which have distinct redox chemistry and battery configurations from aqueous batteries, have gained tremendous interest recently. Furthermore, non-aqueous RFBs have greater potential in providing higher volumetric capacity and energy density than conventional aqueous flow batteries. Historical reviews on the development of flow batteries and the in-depth assessment of different RFB technologies have been well summarized in a number of published review papers [3, 17-20]. The next two sections will concentrate on introducing several of the most popular RFBs systems and the relevance to the current study.

2.1.1. Aqueous redox flow batteries

Aqueous RFB technologies based on several chemistries have been considered for grid storage over the last decades. The redox couples and electrode reactions of these batteries are summarized in **Table 1**. Among these various types of RFBs, VRFB was selected as the model system for most of the following studies, because of its technological maturity and the availability of experiment resources. This section will briefly introduce some of the important aqueous RFBs focusing mainly on VRFBs.

Table 1. Characteristics of conventional redox flow batteries

System (Redox couple)	Electrode Reactions	Cell potential	Support Electrolyte Anode/cathode
All vanadium	Anode: $V^{2+} \overset{Charge\ Discharge}{\rightleftharpoons} V^{3+} + e^-$ Cathode: $VO_2^+ + e^- \overset{Charge\ Discharge}{\rightleftharpoons} VO^{2+}$	1.4 V	H_2SO_4/H_2SO_4
Vanadium-Polyhalide	Anode: $V^{2+} \overset{Charge\ Discharge}{\rightleftharpoons} V^{3+} + e^-$ Cathode: $\frac{1}{2}Br_2 + e^- \overset{Charge\ Discharge}{\rightleftharpoons} Br^-$	1.3 V	VCl_3-HCL/NaBr-HCl
Bromine-Polysulfide	Anode: $2\,S_2^{2-} \overset{Charge\ Discharge}{\rightleftharpoons} S_4^{2-} + 2e^-$ Cathode: $Br_2 + 2e^- \overset{Charge\ Discharge}{\rightleftharpoons} 2Br^-$	1.36 V	NaS_2/NaBr
Iron-Chromium	Anode: $Fe^{2+} \overset{Charge\ Discharge}{\rightleftharpoons} Fe^{3+} + 2e^-$ Cathode: $Cr^{3+} + e^- \overset{Charge\ Discharge}{\rightleftharpoons} Cr^{2+}$	1.2 V	HCl/HCl
H_2-Br_2	Anode: $H_2 \overset{Charge\ Discharge}{\rightleftharpoons} 2H^+ + 2e^-$ Cathode: $Br_2 + 2e^- \overset{Charge\ Discharge}{\rightleftharpoons} 2Br^-$	1.1 V	PEM*-HBr
Zinc-Bromine (Hybrid)	Anode: $Zn \overset{Charge\ Discharge}{\rightleftharpoons} Zn^{2+} + 2e^-$ Cathode: $Br_2 + 2e^- \overset{Charge\ Discharge}{\rightleftharpoons} 2Br^-$	1.8 V	$ZnBr_2/ZnBr_2$
Zinc-Cerium (Hybrid)	Anode: $Zn \overset{Charge\ Discharge}{\rightleftharpoons} Zn^{2+} + 2e^-$ Cathode: $2Ce^{4+} + 2e^- \overset{Charge\ Discharge}{\rightleftharpoons} 2Ce^{3+}$	2.4 V	CH_3SO_3H

Iron/chromium RFB The origin of this RFB can be traced back to the 1970s, when NASA developed its prototype iron/chromium (Fe/Cr) RFB that is generally considered as the first redox flow battery[21]. The Fe/Cr battery is based upon an aqueous solution of a ferric/ferrous (Fe^{2+}/Fe^{3+}) redox couple as the catholyte and a solution containing chromic and chromous ions (Cr^{2+}/Cr^{3+}) as the anolyte. This system can deliver a power density around 80 mW/cm^2 and operate at a relatively low voltage window of 0.9-1.2 V. The major drawback of this system is the severe cross-contamination caused by the traverse of different redox couples across the separator, which renders a short battery life and low coulombic efficiency[22]. Moreover, the Fe/Cr systems usually operated at an elevated temperature around 65 ^oC to maintain operating reaction kinetic, hence consuming extra energy. Although great endeavors have been dedicated to improving the Fe/Cr RFBs since it was invented, this technology has received less amount of attention compared to other flow batteries nowadays.

Zinc bromine flow battery (ZBB) ZBB is a hybrid flow battery system, employing the zinc metal and bromine as active species via the reaction of $Zn+Br_2(aq) \leftrightarrow Zn^{2+}+2Br^-$ [23]. The advantages of ZBB over many other flow batteries are its comparatively higher energy density (70 W h/kg) and lower chemical cost[24]. However, a critical issue with ZBB is the low working current density of 20 mA cm^{-2} due to the sluggish reaction kinetics on the positive electrode and the high cell internal resistance. Thus, many research efforts

were spent on developing advanced electrodes and catalysts to facilitate the reaction kinetics[25]. Although the batteries exhibited improved current density by using these electrodes, the increased cost from using expensive catalyst and complicated fabrication procedure compromise their contribution to the cell performance [24, 26]. Additionally, safety concerns are often associated with ZBBs because of the use of hazardous bromine species as well as from the growth of zinc dendrites during cycling[27].

Sodium bromine-polysulfide battery (PSB) PSB uses sodium bromides and sodium polysulfides as electrolytes, which can give a standard cell potential of 1.36 V. Although the PSB has the advantage of low material cost, it suffers from the sulfur precipitation and the formation of toxic H_2S and Br_2 species, which brings severe safety concerns for large scale applications [28].

Vanadium redox flow battery (VRFB) Among all the existing RFB technologies, VRFB is perhaps the most well-developed system and has been studied extensively[17]. The concept of VRFB was first demonstrated by M. Skyllas-Kazacos et. al. at the University of New South Wales (UNSW), Australia in the mid-1980s[29]. The advantages of VRFB comes from the use of the same redox species (vanadium) in both negative and positive electrolytes. Thus, the cross-contamination issue encountered in the aforementioned RFBs does not affect VRFB. The vanadium ions have four different oxidation states ranging from V(II) to V(V). In VRFB, the V(V)/V(VI) redox couple operates on the positive side of the battery while the V(III)/V(II) operates on the negative half-cell. It is important to note that the different oxidation states of vanadium ions can still diffuse/migrate across the separator in the VRFB, which is usually called "cross-over" in most papers. However, unlike the RFBs using different redox couple species, the cross-over of vanadium ions only results in the reduction of cell efficiency (coulombic efficiency) instead of changing the composition of the electrolyte. For this reason, there is in principle no limitation to the cycle life of VRFB, which made VRFB become favored for grid-storage.

The first-generation battery uses 1-1.5 M vanadium as active redox species and 2.5-3.5 M sulfuric acid as the supporting electrolyte. Besides the abovementioned benefit of eliminated cross-contamination free, the first generation VRFB also demonstrates excellent electrochemical activity and reversibility[30]. Thus, this battery system has been successfully commercialized to the Multi-MWh scale[30].

Despite the notable progress in commercialization, further market penetration of VRFB technology has been hindered by several obstacles: (1) The vanadium sulfate has a solubility limit of ~ 1.7 M in aqueous solution with sulfuric acid as supporting electrolyte. Thus, the first generation of VRFB can only deliver a low energy density (<25 Wh/L), restricting the broader application of VRFB for high energy-density required fields, such as electrical vehicles. Furthermore, the low energy density also demands larger space to accommodate a large amount of electrolyte solutions, which increases the stack size and production cost

of the VRFB. (2) Although the VRFB is free from cross-contamination, the permeation of vanadium species crossing the membrane separators would still lead to the loss of battery efficiency, since extra energy would be required to charge these species back to the fully charged state. Unfortunately, the commercial membranes, such as Nafion®, cannot provide a satisfactory solution to tackle this issue. (3) In addition to the reduced energy efficiency due to the cross-over of vanadium species, there is also a significant voltage loss of VRFB especially at higher current densities, arising from polarization with multiple origins, such as reaction activation, ohmic resistance (from membranes, electrolyte solution, bipolar plates, carbon cathodes, and current collectors), and concentration polarization[31, 32]. These issues greatly undermine the power output for a VRFB station during peak hours. (4) As an energy storage system intended for large-scale purposes, the VRFB should be operated at a reasonable cost. In 2010, the Department of Energy (DOE) of the US has set a long-term capital cost goal of 100 $/kWh for both grid-storage and EV systems[33]. However, the capital cost of VRFB is estimated to be ~ $447 $/kWh [34], which is considerably higher than the DOE target. The high cost of VRFB mainly results from the high price of vanadium redox couples and Nafion membranes.

To address these critical issues, considerable efforts have been spent on increasing the efficiency and capacity of VRFBs, either by looking for alternative electrode and membrane materials or optimizing the electrolyte solutions and cell design. For instance, Li et al. at the Pacific Northwest National Laboratory (PNNL, *USA*) increased the concentration of vanadium from the 1.7 M to 2.5 M by using a sulfate-chloride mixed electrolyte[35]. This new system, often called second or third generation VRFB, can provide 70 % increased energy capacity over the current VRFB system, thus showing enormous potential for commercialization. Despite the great promise, the validation of this novel battery species still requires further examination before moving to the industrial scale. To reduce undesirable polarization and minimize power loss, various approaches have been also proposed for developing new electrode materials with outstanding electrochemical properties [36-38]. These methods include surface treatment of the glassy carbon electrodes[39, 40] and replacing the carbon felts with more conductive or electrochemical-active materials (e.g. carbon nanotubes)[37]. Compared to the research on electrolyte and electrodes, there have been more efforts focused on membrane development in the past decades, since most challenges with VRFB are more or less related to membranes. These challenges are also part of the motivation for this research. More detailed information on the membrane development for VRFB will be covered in section 2.2 of this chapter.

As a summary, there are a great number of other redox couples or active species that can be utilized for aqueous RFBs. These water-based RFBs have advantages in safety and fast reaction kinetics. However, the major drawbacks are their low energy density and high cost. With the immerging demand for the R&D

work in the energy-storage research, cost-effective RFBs based on new chemistry, especially those that can deliver higher energy densities are of greater significance for modern society.

2.1.2 Non-aqueous RFBs

Although aqueous RFBs have by far received most interest, they suffer from a low energy density of ≈25 W h Kg^{-1}, due to both the low electrolyte solubility and, more prominently, a narrow redox-innocent window (<1.9 V). In pursuit of higher energy-density battery systems, there has been a surge of research interest in the RFBs using organic-based active materials and solvent. Non-aqueous batteries typically can provide higher capacity and energy than the aqueous batteries. This is mainly attributed to 2 factors: 1. The use of non-aqueous solvents allows the batteries to be operated at higher cell potentials since there is no concern about water hydrolysis[18]. 2. The theoretical solubility of many redox-active species in non-aqueous RFBs is higher than that of the existing aqueous system, e.g. ~1.7 M $VOSO_4$ for VRFB[3]. Beside higher energy-density, a transition from aqueous RFB to non-aqueous RFB can also offer the benefits of lower price, due to the use of low-cost organic redox species.[41]

Metal-free organic RFBs (or referred to as all-organic RFB), wherein both solvent and redox species are made of organic compounds, have received growing interest in recent years. As one of the pioneers in this area, Liu and co-workers [42] reported an all-organic RFB using 2,2,6,6-tetramethyl-1-piperidinyloxy (TEMPO) and N-methylphthalimide as electroactive species for both catholyte and anolyte, respectively. $NaClO_4$ was employed as the supporting electrolyte and acetonitrile was the solvent in this work. Brushett et. al.[43] has also reported a similar work, in which 2,5-di-tert-butyl-1,4-bis(2-methoxy ethoxy)benzene (DBBB) serves as the catholyte active species and a variety of molecules derived from quinoxaline was used as anolyte active materials. Inspired by these early works, other systems using various redox species including MV/4-HO-TEMPO [44], AQDS/Br_2 [45], AQDS/BQDS [46] have also been reported. These all-organic RFBs can be operated at an elevated voltage of 1.7 – 2.2 V and can withhold higher concentration (>2M) of active materials. By combining low-cost solvents and separators, these affordable RFBs with potentially high energy density could be attractive to the market.

Another important class of non-aqueous RFB uses the metal-coordinated redox couple instead of an organic compound. The major advantage of using a metal-coordinated redox couple is the higher battery potential (>2.0 V). The early works mainly focused on Ruthenium-based active materials. Matsuda et al. reported a RFB system using $[Ru(bpy)_3]^{2+}/[Ru(bpy)_3]^{3+}$ as the anolyte redox couple and $[Ru(bpy)_3]^{+}/[Ru(bpy)_3]^{2+}$ as the catholyte redox couple[47]. Their battery could deliver an open circuit voltage of 2.6 V with acetonitrile solvent. However, the battery performance was obtained at a relatively low current density of 5 mA/cm^2. Besides the Ruthenium-based RFBs, more non-aqueous RFB studies focus on the zinc/cerium cell (Zn/Ce RFB), developed by Plurion Limited, GB. In Zn/Ce RFB, zinc metal is employed at the negative electrode

and Ce (III)/Ce(IV) serves as the positive side redox couple. The system has a cell potential of ~2.5 V and can work at a current density of 50 mA/cm^2 with ~60% energy efficiency [48].

Very recently, inspired by the Li-S battery works, a new lithium polysulfide (Li-PS) battery concept has been developed from the lithium-sulfur (Li-S) batteries. This system has a high theoretical capacity (1675 mA h g^{-1}) and energy density (~2600 W h kg^{-1}) for element sulfur and lithium [49]. Due to the employment of liquid polysulfide electrolytes instead of insoluble reactants, the volume expansion which is a big issue in the conventional Li-S batteries can be avoided. Since both lithium and sulfur are abundant elements on the earth, the raw material cost for the Li-PS flow batteries ($45 kW h-1) is much lower than that of traditional vanadium flow batteries ($50-110 kW h^{-1}) [15], exhibiting great potential for wide application. Additionally, the voltage of the Li-PS battery (2.15-2.8 V) is almost two times than the conventional vanadium flow batteries (1.1-1.7 V). Because of all these desired features, the Li-PS flow batteries are expected to find a prominent role as a powerful electrochemical storage system in the renewable energy plants, as well as a power supplying systems for the future electrical vehicles.

Even though a great deal of effort has been invested in developing non-aqueous RFBs, the study in this area is still in an early stage. By far, there is an absence of standardized testing protocols for these new battery systems. The reported performances of non-aqueous RFBs are often obtained at very low current densities with a small amount of electrolyte. Besides, compared to aqueous RFBs, non-aqueous RFBs usually exhibit poor electrochemical performance, probably due to the low electrolyte conductivity and sluggish reaction kinetics. More importantly, the active species cross-contamination is even more severe in non-aqueous, because of the high electrolyte concentration and lack of suitable membrane to attenuate the crossover problem. Most commercial membranes are either soluble or mechanically weak in the organic solvent, yet there are few studies about the membrane materials for organic electrochemical systems. Herein, the limited choices of membranes and their undesirable performance in different solvents/redox species are critical issues that hinder the development of non-aqueous RFBs [45, 50]. This is the motivation for our work on developing highly ion-selective and stable IEMs for organic RFBs. This part of the work will be introduced in Chapter 5.

2.2 Overview of membranes developed for RFBs

The membrane or separator is one of the most important components in all RFB systems. It plays a critical role in separating the cathode and anode compartments while allowing the transport of charged ions (H^+ or SO_4^{2-}.) to complete the circuit. Another important function of the membrane is to prevent the crossover of ions in the negative and positive side either under the driving of the concentration gradient or electrical

field. To date, most membrane development work focus on the application in vanadium flow batteries to replace expensive Nafion membranes. This section will briefly overview the membrane development progress in VRFBs, but a similar concept can be applied to other flow batteries as well.

2.2.1 Proton exchange membranes

Generally, an ideal membrane for VRFB applications should exhibit the following characteristics: 1) low vanadium ion and water molecule permeation rates to minimize self-discharge; 2) high proton conductivity/low area resistance to minimize voltage efficiency loss; 3) good chemical stability under operational conditions; and 4) low cost [20]. Based on the ion transport and separation mechanism, the IEM used for VRFB can be generally classified as proton exchange membranes (PEMs) and anion exchange membranes (AEMs). Proton exchange membranes (PEMs) have received more attention for the research and application in RFBs due to their facile synthesis, tunable conductivity, and the community's broader understanding of their ion transport properties compared to AEMs.

Perflourinated proton exchange membranes Perfluorinated membranes, nominally Nafion® by Dupont, are the most widely implemented and studied membranes in RFBs [20]. The common structure for the perfluorinated membranes is a tetrafluoroethylene (Teflon) backbone grafted with perfluorovinyl ether groups terminated with sulfonate groups. These membranes normally consist of a hydrophobic phase made by Teflon backbone and a hydrophilic phase formed by the sulfonated side chains [51]. The most attractive features of Nafion® are its excellent chemical and mechanical stabilities provided by the Teflon backbone, giving high tolerance to the strong oxidant (for example VO_2^+ in the VRFBs) in many RFB applications. At the same time, the hydrophilic zone in Nafion assembled by sulfonated groups provides a decent ion conductivity, especially in the acidic environment.

Despite the favorable stability and proton conductivity, the low monovalent/multivalent cation selectivity remains a serious concern on Nafion membranes in RFB applications, especially for the vanadium flow batteries. The cross-contamination severely diminishes the available active materials leading to fast capacity decay and low coulombic efficiency. To improve the ion selectivity, modification of Nafion by either physically blending with inorganic compounds or chemical functionalization have been received continuous interest. It was reported that the Nafion membranes modified by incorporating inorganic materials (e.g. SiO_2 [52], TiO_2 [53], GO[54], etc.) can help to suppress vanadium crossover better than pristine Nafion membranes, although they also exhibit reduced proton conductivity. Modifying the Nafion surface via chemical functionalization (e.g. electrolyte soaking, oxidation, and electrodeposition) has also been reported to be effective to increase the ion selectivity and reduced water transfer of Nafion [8]. Due to the different testing environment and transport mechanisms, many of these implanted works only achieved

marginal improvement in flow batteries performance. Despite the remarkable electrochemical properties and stability, the extremely high cost (600–800 USD m^2) and fast active species crossover are consistently cited as drawbacks for Nafion. Hence, alternative membranes should be developed. In our research, Nafion membranes are used as reference samples, because of the wide availability of material properties from literatures

Non-fluorinated PEMs Non-fluorinated hydrocarbon membranes have received broad attention as an alternative replacement to Nafion in RFBs due to their low cost, recycling convenience, and potential high ion selectivity [55]. Early work of applying sulfonated aliphatic hydrocarbon membranes, including sulfonated polyethylene (PE) and laminated sulfonated PE membranes, on VRFBs was introduced by Skyllas-Kazacos [56] and Hwang et al [57]. Although the cells using these membranes exhibit desirable CE (>90%), the high membrane resistances often give rise to a poor VE.

Recently, the sulfonated aromatic polymers are receiving more interest from researchers, in the hope that the rigid main chain structure and less connected ionic cluster regions may provide lower vanadium permeability than Nafion. Polymers such as sulfonated poly(arylene thioether ketone), sulfonated poly-(fluorenyl ether ketone), poly(arylene ether sulfone), and sulfonated poly(tetramethydiphenyl ether ether ketone) (SPEEK) have been reported to show similar or better performance than Nafion in VRFBs.

The main concern for the sulfonated hydrocarbon PEMs is long term durability in RFBs. To achieve decent proton conductivity, the hydrocarbon polymers are required to contain a high concentration of acidic groups, which leads to severe swelling and weakened mechanical strength [20]. The sulfonated polymer backbone is also known to be inherently weak to oxidation attack, decreasing the membrane lifespan in the oxidative environment. Moreover, their application in RFBs has just started there is still a lack of systematic study on these membranes

Pore-filled PEMs Pore filling is a novel method to prepare IEMs with low swelling and high selectivity. These membranes are commonly fabricated by infiltrating ion exchange resin into a mechanical robust porous support. This technique allows the optimization of the properties of the filler and the matrix separately, which can synergistically improve the overall performance of the membrane [58]. The improved mechanical integrity and lower swelling ratio of the pore filled membranes provided by the dimensionally stable substrate materiel are desirable properties for the redox flow batteries properties. The stronger mechanical property reduced the risks of fracture during cell assembly and operation at the flow-through condition. The fabrication of free-standing ion exchange membrane with sub-30 μm thickness also became achievable using the pore filling technique. Decrease or reduce membrane thickness helps to decrease the membrane resistance, which is especially critical for anion exchange membrane. The low swelling ratio

narrowed water channel diameter in the polymer electrolyte matrix, leading to a reduced active species crossover [59]. It was found recently that by controlling the alignment of polymer electrolyte in the porous substrate, the conductivity and ion selectivity of the pore-filled membrane can be higher than the pristine polymer membrane [60].

To prepare IEMs using the pore-filling method, the most important prerequisite is to search for appropriate porous substrates that are chemically inert, mechanically stable, compatible with polymer electrolyte, and cost-effective [58]. Different porous supports can be used for this kind of membrane fabrication, most of which are polypropylene (PP), polyethylene (PE), polytetrafluoroethylene (PTFE), Daramic (W.R. Grace), and track-etched polymer carbonate (TEPC). Apart from polymeric substrates, inorganic materials, such as porous alumina can also be used to obtain pore filling IEMs[61]. For inorganic substrates, the pore size distribution is uniform, and the pore is small enough compared to polymeric substrates, leading to higher selectivity.

Pore-filled IEMs can be prepared by directly introducing polymeric electrolytes into the porous substrates. The simplest approach is to pour the selected resin solution on the surface of substrate membranes followed by vacuum drying [62]. In many cases, these steps need to be repeated several times to ensure successful infiltration. The pore-filled IEMs can be alternatively prepared via a so-called 'pore soaking technique', by immersing the porous substrates in the resin solution [63]. After the infiltration, the chemical stability of the resulting membranes can be further improved/enhanced by the cross-linking reactions.

Nowadays, the pore-filling method has gained increased popularity for fabricating the IEMs due to their exceptional mechanical property. By taking this advantage, we also fabricated the pore-filled IEMs with the low swelling ratio as the substrate for transferring 2D materials, as will be introduced in chapter 4.

2.2.2 Anion exchange membranes (AEMs)

AEMs are designed for conducting anions while being impermeable to cations or neutral molecules [64]. The major advantage of AEMs over PEMs is their high rejection for cations. For example, the positively charged groups in AEMs can repulse vanadium cations via the Donnan exclusion mechanism in VRFB system. Therefore, the AEMs usually exhibit extremely low vanadium cation permeability compared to PEMS, resulting in an almost 100 % coulombic efficiency in VRFB.

The majority of research efforts on AEMs development are devoted to synthesizing new anion conducting groups. A state-of-the-art AEM is the quaternized ammonium (QA) based AEMs [65, 66]. This group of membranes is featured with its facile synthesis procedure and flexible design. The QA-AEMs are commonly prepared by functionalizing a polymer precursor with a benzyl halide and trimethylamine (TMA) groups. A variety of tertiary amines precursors have been investigated to target at improving the anion

conductivity or mechanical property. AEMs with other types of anion conducting groups, such as imidazolium cation groups [67], benzimidazolium groups [68], pyridine groups [69], and phosphonium groups [70], have also received extensive research. Besides these efforts on synthesizing new functional groups, AEMs with new polymer architecture (e.g. comb-shaped AEMs) have also been studied [71, 72].

To date, most AEMs are developed for fuel cell researches applications. The application of AEMs in redox flow batteries has just started. The major concerns of AEMs lie in low anion conductivity due to the low anion (e.g. SO_4^{2-}) mobility in the polymer matrix and electrolyte solution. In contrast to PEMs, protons can transport via Grotthuss mechanism in PEMs and aqueous solution, resulting in a higher membrane ion conductivity. Therefore, future work on AEM development for RFBs may target for improving the anion conductivity and the chemical and mechanical stability.

2.2.3 Non-ionic porous Separator

Porous separator is another type of membrane that started to be employed for VRFBs. These membranes, traditionally used in lithium-ion batteries, selectively transport ions based on the size sieving effect instead of charge interaction. The microporous separators are traditionally used in lithium-ion batteries. Their potential as separators in VRFB originates from the feasibility of separating protons from vanadium ions due to the different Stokes radii. By optimizing the pore size, the microporous membrane can still achieve a decent proton/vanadium selectivity even without any surface ion-exchange groups.

Zhang et al. [73] first reported the successful use of nanofiltration (NF) membrane for VRFB. The membrane has a sub-micron thin selective layer connected to a much thicker substrate with finger-like pores. VRFB assembled with this membrane has shown acceptable battery performance (EE~80%). Following this work, Zhang et al. [74] later reported another porous membrane by introducing silica as ion filters. These membranes have shown higher ion H^+/VO^{2+} selectivity than the pure polymer-based NF membranes and provide slightly enhanced battery performance. Based on a similar concept, Yang et al. [75] reported a zeolite membrane for VRFB application. The membrane has a micrometer zeolite selective layer grown on α-alumina substrate. This membrane also exhibits a higher ion selectivity than Nafion. However, only limited battery characterization has been reported.

Compared to the IEMs, the advantage of microporous membranes comes from the lower cost and good stability. However, these porous separators usually possess a lower conductivity and higher membrane resistance. Thus, batteries equipped with these membranes commonly exhibited a poor voltage efficiency. Despite the unsatisfactory performance of the microporous membrane, this strategy of utilizing the size difference of vanadium ions and protons to enhance membrane performance has been widely accepted and inspired many other works, such as poly (benzimdazole) (PBI) membranes[76].

2.2.4 Separator for nonaqueous RFBs

IEMs like Nafion have been widely adopted in aqueous RFBs. However, in the non-aqueous electrolyte, the conventional IEMs have shown poor performances due to the crossover of redox couples, which is mainly a consequence of membrane swelling and deformation. Instead of IEMs, ceramic conductors (e.g. perovskite, NASICON, and garnet type) are generally used for non-aqueous RFBs, owing to their excellent chemical/mechanical stability in non-aqueous electrolytes. In this section, membranes/separators developed for non-aqueous RFBs will be introduced. Porous separator has been extensively employed in NARFBs owing to their excellent stability and relatively low cost. Unlike IEMs, commercial porous separators are usually fabricated using chemically inert materials, such as PTFE, PP, and PE, thus having strong resistance against organic solvent. These membranes usually have a large pore size ranging from tens of nanometers to several micrometers. Due to the highly porous structure, the resistance of porous separator can be much lower than that of the IEMs and ceramic separators in the electrolyte solution. However, the large pore size also gives rise to severe crossover issue, which is the major drawback of using porous separators in NARFBs. Since the chemical environment in the non-aqueous batteries is usually more complicated than the aqueous systems, the active species cross over not only reduce their round-trip efficiency but also leads to unexpected side reactions that undermine the battery lifespan.

Ceramic conductors like NASICON typically have a chemical formula of $Na_{1+x}Zr_2Si_xP_{3-x}O_{12}$. A more general formula of NASICON is $AB_2(PO_4)_3$, where *A* is a monovalent cation, such as Li, Na, and K, while *B* could be either single or multivalent ions, such as Ge, Zr, or Ti.[77] One of the most widely studied NASICON materials is the lithium superionic conductor (or called LISICON), such as $Li_{1+x+y}Al_xTi_{2-x}Si_yP_{3-y}O_{12}$ (LATP) [78] and $Li_{1+x}Y_xZr_{2-x}(PO_4)_3$[79]. These materials can transport lithium in organic electrolytes. However, the ionic conductivity of LATP relies on fabrication conditions. In most cases, the areal resistance of the ceramic conductors is higher than that of porous membranes.

In recent years, IEMs have received an increasing amount of interest as highly selective, cost-effective materials for NARFB. The narrowly distributed pore size and the unique separation mechanism based on charge interaction of IEMs are ideal to alleviate the crossover of large organic active compounds. However, most polymeric IEMs do not have sufficient chemical stability in organic electrolytes, which greatly narrows the selection of IEMs for NARFBs. Additionally, ion exchange groups in many IEM cannot dissociate in organic electrolytes, leading to a low conductivity in non-aqueous RFBs[80]. Therefore, comparing to the popularity of IEMs in aqueous RFBs, there much fewer reports on the development of new membranes for non-aqueous RFBs.

2.3 Ion transport studies for ion exchange membranes

Although substantial work has been devoted to the synthesis and testing of these novel ion-exchange membranes, there is a deficiency in the fundamental understanding of the molecular-level ion transport mechanisms in the polymer electrolyte matrix. It appears that these fundamental and mechanistic insights are crucial for the success in designing novel IEMs and improving their electrochemical performance in RFBs.

Proton transport is the most fundamental mechanism in PEMs since the high conductivity is essential for the batteries operating at a high current density. Nafion is the most well-studied membrane systems, for which there are several proton transport models. Despite this work, a consensus is absent. The first proton transport mechanism in Nafion was proposed by Gierke et al. [51]. They proposed a cluster-network model for the Nafion structure and attributed the transport of ions to a percolation mechanism (also called hoping mechanism). In this mechanism, the proton percolates and hops between each ionic cluster connected by 1-nm-diameter channels. This mechanism is close to the Grotthuss mechanism that explained the fast proton transport in bulk aqueous solutions. Another prevalent mechanism is the vehicular mechanism or called diffusion mechanism in which the hydronium ions (H_3O^+) transported through the aqueous medium by electroosmotic drag and concentration gradient. The existence of water transport channels and free volumes in the membrane matrix is the main reason for the vehicular mechanism.

Various numerical modeling and modern characterization methods enable a deeper understanding of polymer structures and ion transport in the IEMs. By combining numerical simulation and small-angle X-ray scattering (SAXS), Chen et. al. explained the fast proton and water transport through Nafion via the water channel model [81]. They observed that the sulfonic acid functional groups were arranged into long, parallel, randomly distributed water channels with diameters between 1.8 and 3.5 nm, which affords excellent proton conductivity. Eikerling et al [82] using a numerical modeling method explained details of the proton transport behavior via a surface mechanism. In this mechanism protons are transported along with the array of acid groups on the interface. Additionally, they have attempted to build a model on the membrane morphology where the connections of the hydrophilic domains, evolution of the pore volume, and the orientation of the pores in the network with water uptake were considered[83].

The capacity loss in VRFB is caused by the undesired transport of active vanadium species across the membrane. Hence, the basic understanding of vanadium ion transport through IEMs is essential for explaining the capacity loss during battery operation and helpful for looking for solutions. Kumbur et al. [84] developed a 2-D transient, isothermal model that can predict the ion crossover flow rate and concentration gradient across the Nafion membrane. However, their initial work did not distinguish the contribution of diffusion, migration, osmotic, and electro-osmotic convection from the total driving force

for the ion movement. The same group later developed an experimentally validated, 2-D model that incorporated the species transport across the membrane due to migration, diffusion, and convection. Nevertheless, their simulation work revealed that the driving mechanism was quite dependent on the polymer species.

Although some works have explored the ion transport mechanisms in the IEMs, an in-depth numerical analysis accounting for multiple ion species, different membrane materials, and various operating conditions should be established to better understand the mechanism responsible for the ion crossover, proton-conducting, and the related battery performance.

2.4 Obstacles for the membrane development for RFBs

Various types of membranes based on different working mechanisms, materials properties, and membrane architectures have been developed for aqueous and non-aqueous RFBs. Although an improvement on the battery performance has been achieved with these efforts, a couple of fundamental problems remain unsolved, which greatly hinders the research progress in this area. These limitations are summarized as follows:

1. Trade-off limitation between ion selectivity and permeability.

One of the most critical issues with IEMs is the trade-off limitation between the ion selectivity and permeability, as the most efforts in improving one property will lead to the decrease of the other. In aqueous RFBs, especially VRFBs, PEMs can provide a high proton conductivity but suffers from the crossover rate of positively charged active species (e.g. vanadium ions). AEMs with the opposite exchanging ions can effectively address the active species crossover due to the Donnan mechanism while their performance is limited by the low conductivity of sulfate anions. This trade-off limitation is also affecting the composite membranes and porous membranes. Especially in organic RFBs, polyolefin porous membranes (e.g. Celgards) or glass fiber membranes are commonly employed as battery separators, mainly due to their stability and low cost. However, these membranes only function as an electronic insulator between the two electrodes and cannot address the crossover issue of active species. Thus, a continuous research effort on improving the ion selectivity of the membrane separators is imperative to enhance the overall efficiency of RFBs.

2. Membrane mechanical and chemical stability

The poor membrane mechanical/chemical stability in the battery testing environment is another great challenge for the current membrane research. A wide range of commercial and laboratory-synthesized membranes start to be degraded after a few tens of battery cycles, which leads to the quick capacity decay

and increased cell resistance. Moreover, there is a lack of testing standards to characterize the membrane stability in RFBs. Plenty of works have reported stable membrane performance after hundreds of battery cycles. However, the real testing time for each cycle could be quite different from one to another depending on their operating parameters, such as current density, amount of electrolyte, and cut-off voltage. In addition to the testing standard, there is also a critical need for developing in-situ testing methods to diagnose the membrane condition during operations.

It is also noteworthy that the issues mentioned above are more severe for the non-aqueous RFBs. Most IEMs developed for aqueous systems cannot be applied for non-aqueous RFBs since they can either be dissolved by the organic electrolyte or severely swelled. Nonetheless, a considerable share of research efforts so far for non-aqueous electrochemical systems still focuses on studying the electrolyte chemistry and electrode design rather than on developing separators. As a critical component in RFBs, membranes are closely related to the overall battery performance. Hence, it is urgently required to develop stable membrane materials for the non-aqueous RFBs.

3. High cost.

As discussed above, the expense on membranes comprised a large part of the cell capital cost. Alternative membranes with lower cost must be developed to replace the perfluorinated membranes. Besides, the cost of the membrane is not only affected by the raw materials, but also by the membrane thickness and fabrication procedure. A thicker membrane usually has lower vanadium permeability but will lead to an increased cost. Some membranes fabricated via complicated steps or using expensive additives and substrates are also not preferable for industrial applications.

To address these problems, there is a need for continuous efforts on developing membrane materials. While it is also important to understand how ion transport and battery performance are related to the basic membrane properties, which would require more in-depth chemical analysis and numerical modeling.

III. DEVELOPMENT OF A HIGHLY SELECTIVE AND LOW-COST AROMATIC POLYMER MEMBRANE FOR VANADIUM REDOX FLOW BATTERIES (VRFBS)

(Previously published as Wang, T., Jeon, J. Y., Han, J., Kim, J. H., Bae, C., & Kim, S. "Poly (terphenylene) anion exchange membranes with high conductivity and low vanadium permeability for vanadium redox flow batteries (VRFBs)." *Journal of Membrane Science* 598 (2020): 117665.)

Ion exchange membrane (IEM) is one of the most critical components in VRFB which should prevent cross-mixing of the multivalence vanadium ions, while allowing the transport of charge-carrying ions to complete the circuit [85]. However, there is a trade-off between ion conductivity (membrane resistance) and selectivity of co/counter-ions in conventional polymeric IEMs, which greatly lowers the energy efficiency of VRFBs [85]. The high vanadium permeation across conventional PEMs which leads to rapid capacity fade with cycling and low coulombic efficiency (CE). Anion exchange membrane (AEM) suffers from poor chemical stability and low voltage efficiency due to low anion conductivity [86].

Recently, sulfonated aromatic polymers are recognized as promising candidates to fabricate low-cost, high-performance membranes in VRFBs [87, 88]. This type of membranes is commonly featured with high mechanical strength, good oxidative stability, low vanadium permeation, and reasonable proton conductivity. However, most efforts on implanting aromatic PEMs from fuel cell research to VRFBs have been hampered by low proton selectivity over multivalent vanadium cations. Hence, a new polymer design for the VRFB application and a deeper understanding of the molecular structure-performance relation are needed.

In this study, we herein rationally designed and fabricated a series of PEM and AEM with high ionic conductivity as well as ion selectivity. These polymers were built on rigid biphenyl/terphenyl backbone and decorated with different side chains. The ion transport properties of the membranes are investigated by measuring the vanadium/hydronium ion permeability, proton conductivity, area resistance, and ion exchange capacities. The single-cell VRFB performance with the prepared membranes are evaluated and compared with the conventional Nafion membranes. To understand the origin of this high performance, we studied the polymer membranes with small-angle-x-ray scattering (SAXS) and density functional theory (DFT) calculations. Based on these results, the relationships between the molecular structures and the selective ion transport properties were established.

3.1 Materials and characterization methods

Chemicals Nafion® 117 and 212 were purchased from Ion Power Inc. (DE, USA). A commercial AEM, Fumasep® FAP-450, was purchased from FUMATECH BWT GmbH (Bietigheim-Bissingen, Germany). Vanadyl sulfate ($VOSO_4$, 99.9%) and magnesium sulfate ($MgSO_4$, 99.5%) were purchased from Alfa Aesar (MA, USA). Sulfuric acid (H_2SO_4, 98.0%) was purchased from Fisher Scientific (PA, USA). All reagents and solvents used for synthesis of the polymers were purchased from Aldrich, Alfa Aesar, TCI Chemical Co., and Strem Chemicals, and were used without further purification.

Synthesis of biphenyl polymers (PEM). Chemical structures of the biphenyl polymers with various pendent groups (synthesized and provided by our collaborators from Rensselaer Polytechnic Institute) are depicted in **Figure 2.** These polymers were synthesized from low-cost monomers via facile approaches (synthesis approach has not been disclosed yet). To cast these polymers into membranes, the polymers were first dissolved in N,N'-dimethylacetamide (DMAc) solution at 5-8 wt %. The desired amount of polymer solution was poured into a glass mold with 4.5×4.5 cm^2 area. Solvent was evaporated at 70 °C for 12 h under ambient pressure. The membranes were gently pealed from the glass mold and immersed 1 M H_2SO_4 solution at 80 °C for 1 h for acidification. Afterwards, samples were stored in deionized water at room temperature before testing.

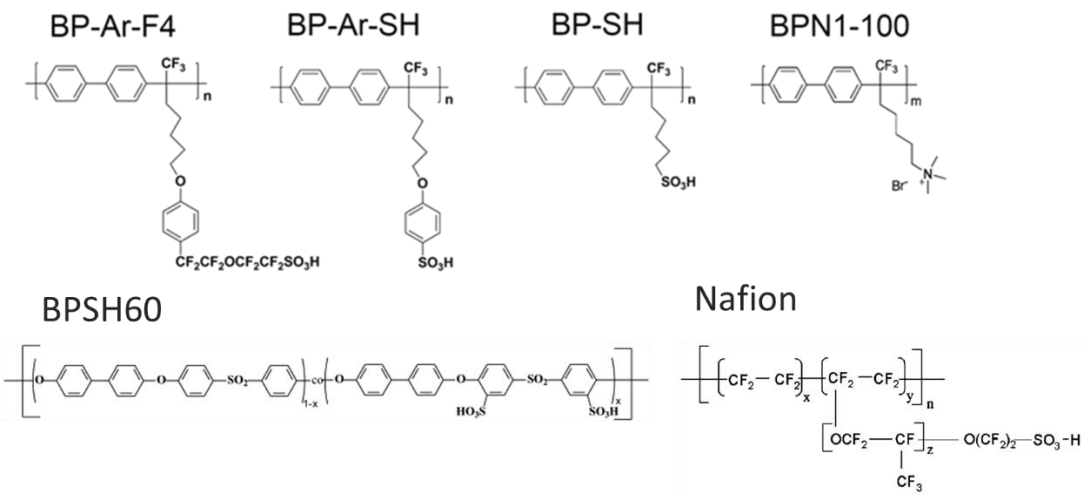

Figure 2 | Chemical structures of the polymers studied in this work.

Synthesis of terphenyl polymers (AEM).

p-TPN1, *m*-TPN1, and BPN1-100 were synthesized by acid-catalyzed Friedel-Crafts polycondensation of aromatic monomers and 7-bromo-1,1,1-trifluoroheptan-2-one, followed by quaternization of alkyl bromide with trimethylamine (**Figure 3a**). The detailed synthetic methods have been described in our previous

publications [89, 90] and the chemical structures of the polymers are shown in **Figure 3b**. The molecular structures were confirmed by ^{1}H NMR. The polymers are alternating copolymers composed of aromatic unit (blue in **Figure 2b**) and a trimethylammonium (TMA) group-tethered alkyl unit (red in **Figure 2b**). The aromatic unit was varied by changing the aromatic monomers, *para*-terphenyl, *meta*-terphenyl and biphenyl for *p*-TPN1, *m*-TPN1 and BPN1-100, respectively. The insertion of a sp^{3}–hybridized tetrahedral carbon spacer between rigid aromatic groups on the polymer backbones enhances flexibility of the polymer chain, affording high molecular weights and excellent mechanical properties; the three AEMs show tensile stress higher than 20 MPa at 50 °C and 50% relative humidity condition [89, 90].

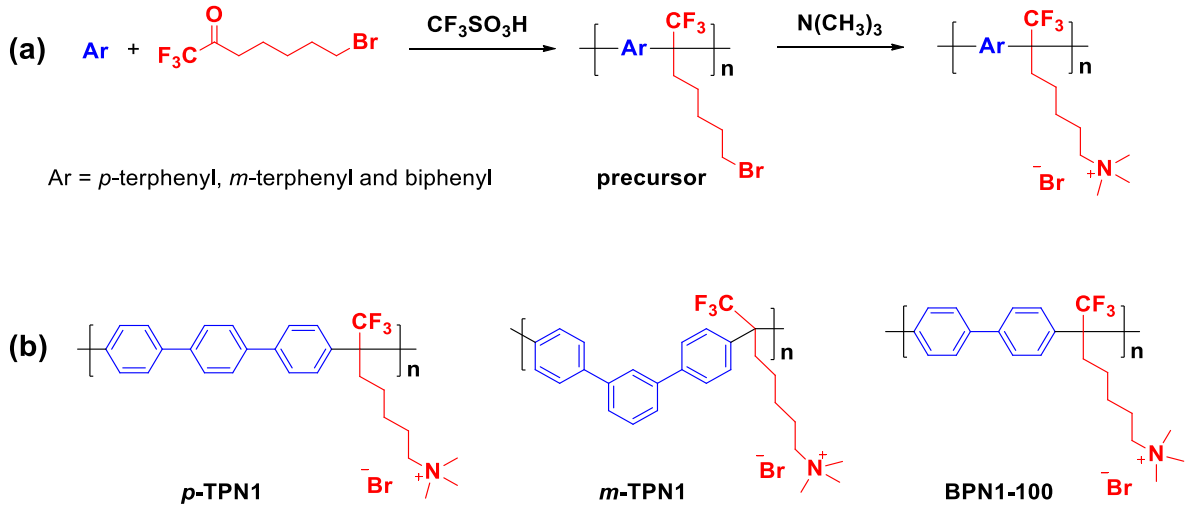

Figure 3. (a) Synthetic route for *p*-TPN1, *m*-TPN1, and BPN1-100 and **(b)** their chemical structures.

Ion exchange capacity Ion exchange capacity values based on weight (IEC_w) were measured using a conventional titration method. The membranes were immersed in a 1 N NaCl solution for 24 hours in order to substitute H^+ ion of the sulfonic acid groups with Na^+ ion. The substituted solution was titrated using a 0.01 M NaOH solution with phenolphthalein as an indicator. The IEC_w value was calculated from the following equation:

$$IEC_w = \frac{0.01 \times V_{NaOH}}{W_{dry}}$$

where V_{NaOH} is the volume of NaOH solution which was added in titration, and W_{dry} is the weight of membrane at dry state.

Membrane preparation PEM and AEM membranes were prepared by casting 5–7 wt% polymer/DMSO solution on a homemade polypropylene/glass mold. The membranes were subsequently dried at 70°C under a constant flow of nitrogen for 24 h. Nafion® membranes were pretreated with 3 wt.% H_2O_2 solution for 1

hour, boiling deionized water for 1 hour, and boiling 1 mol/L H_2SO_4 solution for 30 min [91]. Fumasep® FAP-450 membrane was used without any pre-treatment. All membrane samples were immersed in 1 M H_2SO_4 for 1 day before characterization and battery tests.

VO^{2+} and H^+ permeability The VO^{2+} permeability of membranes was tested using a diffusion test as described in elsewhere [53]. The prepared membrane with an effective area of 1.76 cm^2 was sandwiched between two diffusion half cells. The feed side reservoir was initially filled with 11 ml of 1 M $VOSO_4$ in 2 M H_2SO_4 solution and the permeate side reservoir was filled with the same amount of 1 M $MgSO_4$ in 2 M H_2SO_4 solution. A magnetic stirrer was placed in each cell and kept for stirring during the test to avoid diffusional concentration polarization. The VO^{2+} concentration at the permeant side was monitored using UV-Vis spectroscopy (UV-1800, *Shimadzu*, Japan). The VO^{2+} permeability through the membrane was calculated from Fick's law:

$$V\frac{dC_B(t)}{dt} = A\frac{P}{L}\left(C_A - C_B(t)\right)$$

where V is the volume of solution in each reservoir, C_A is the feed side VO^{2+} ion concentration, C_B is the permeation side VO^{2+} ion concentration, t is the testing time, A is the effective membrane area, P is the VO^{2+} ion permeability, and L is the membrane thickness.

Proton conductivity and area resistance The in-plane proton conductivity was measured by using electrochemical impedance spectroscopy (EIS) method. During the test, the membranes were placed on two gold-coated plates with 1 cm gap. Impedance measurements were performed in the frequency range from 10^6 Hz to 10 Hz with an amplitude of 10 mV using a Metrohom potentiostat/galvanostat (Metrohm, FL, USA). The membranes were immersed in deionized water for 24 hours to fully hydrate the membranes before proton conductivity test. The proton conductivity was calculated from the resistance value which was obtained by extrapolating the low-frequency curve on the Nyquist plot based on the following formula:

$$\sigma = \frac{L}{R \cdot A}$$

where L corresponds to the electrode separation, R is the membrane resistance obtained by extrapolating the low-frequency curve on the Nyquist plot and A is the membrane cross-sectional area. For the area resistance measurement, the conductivity cell was setup using the method described in literature [17]. The resistance of the entire cell with and without the membrane was determined using EIS. The area resistance of the membrane was calculated from the difference between the two values.

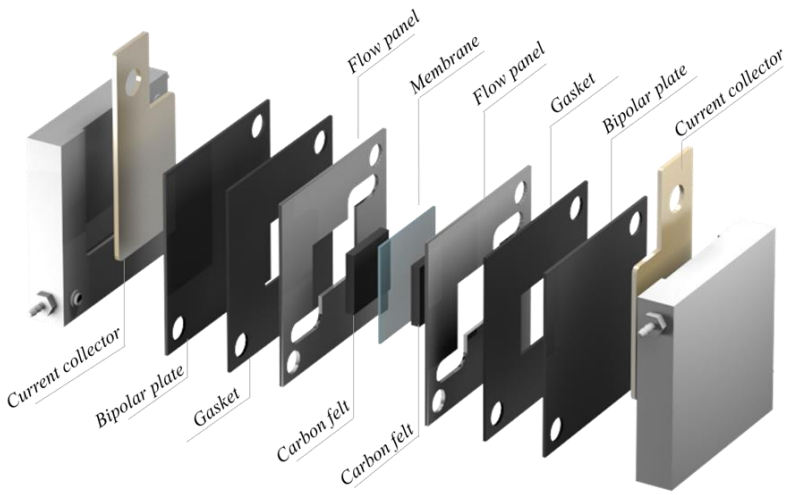

Figure 4. Configuration of vanadium redox flow battery.

VRFB single cell performance test The configuration of VRFB cell is provided in **Figure 4.** Two graphite felts (MTI, 30 × 30 × 4 mm) were used as electrodes without any post-treatment. The testing membrane was sandwiched between the two graphite felts with an active area of 9 cm^2. Two copper current collectors were coated with gold to prevent corrosion. The gold coated copper plates were separated from carbon felts by two TF6 SIGRACELL® bipolar plates (SGL Carbon, USA). Same volume of electrolytes (each 45 mL) containing 1.6 M vanadium ions and 4 M H_2SO_4 were adopted as catholyte and anolyte. The catholyte was prepared by oxidizing V(IV) to V(V) ions under galvanostatic condition, and the anolyte was prepared by reducing V(IV) to V(II). During the battery operation, the half-cell reaction on the positive electrode was: $\mathrm{V(IV)} \rightleftharpoons \mathrm{V(V)} + e^-$, and the reaction on the negative electrode was: $\mathrm{V(III)} + e^- \rightleftharpoons \mathrm{V(II)}$.[92] The electrolytes were circulated by Masterflex L/S peristaltic pumps (Cole-palmer, USA) with the flow rate of 30 mL/min. The operation of the cell was controlled by a CT2001A-5V1.8A battery testing system (Landt, China) with the cut-off voltage of 1.65 V (charge process) and 0.8 V (discharge process), respectively. All test has been repeated three times. Coulombic efficiency (CE), voltage efficiency (VE) and energy efficiency (EE) of VRFB were calculated by the following equations and averaged from three experiments (Table A2):

$$Columbic\ efficiency(CE), \% = \frac{t_{Discharge}}{t_{Charge}} \times 100\ \%$$

$$Voltage\ efficiency(VE), \% = \frac{V_{Discharge}}{V_{Charge}} \times 100\ \%$$

$$Energy\ efficiency(EE), \% = CE \times VE/100$$

Activation energy measurement.

The permeation activation energy of vanadium ions in Nafion and BP-ArF4 was obtained from the Arrhenius plot. The vanadium permeability and temperature follow an Arrhenius like relation:

$$D = D_0 \exp\left(-\frac{E}{RT}\right), \quad Eq.7$$

Where D is the vanadium permeability/diffusivity (cm^2/min), D_o is the pre-exponential factor (cm^2/min), E is the activation energy (kJ mol^{-1}), R is the universal gas constant (8.314 J $mol^{-1}K^{-1}$), and T is the absolute temperature (K).To measure the vanadium permeation activation energy, the VO^{2+} permeability test was performed at different temperature for each membrane inside a temperature-control chamber. From all the experiments, it was found that log(D) is linearly correlated with 1/(RT). As suggested by the equation., activation energy was obtained from the slope of the log(D) *vs.* 1/(RT) plot.[93] It worth mentioning that membrane has different swelling ratio at different temperature. Hence, the change of membrane dimension was considered during calculating membrane permeability at each temperature.

Oxidative stability The oxidative stability of the membranes against V(V) species was tested according to a method reported in the literature [94]. Prior to the test, the membranes were dried in vacuo for one day. Afterward, 0.12 g (dry weight) membrane sample was immersed in 10 mL of 0.1 M V(V)/4 M H_2SO_4 solution, which is prepared from the fully charged catholyte solution. The concentration of V(IV) species in the solution, which is generated due to the oxidation of membranes, was monitored using a UV-Vis spectroscopy (UV-1800, Shimadzu, Japan).

Density functional theory (DFT) calculations. DFT calculation was done by Dr. Choe in AIST (Japan). ωB97XD functional [95] and 6-31G(d,p) basis sets for S, N, C, H and O atoms [96, 97] were employed for the DFT calculations. For vanadium, core electrons were represented by LANL08 effective core potential (ECP) and for valence electrons of vanadium, we used LANL08 basis sets augmented by f function [98-100]. Geometry optimizations and additional frequency calculations to confirm the optimized structure is minima were conducted using Gaussian 16 program.

3.2 Biphenyl proton exchange membranes (PEM)

3.2.1 Ion transport properties

To characterize the ion transport properties of the membranes, we evaluated the IEC, vanadium ion permeability, proton conductivity, and area resistance of the prepared membranes (Table 2). Commercial Nafion 117 and 212 membranes, which are widely used in VRFBs, were used as reference samples. The low vanadium ion crossover is a critical property of IEMs to achieve high CE values and low capacity loss in VRFB applications. Among all membranes tested, the BP-SA membrane showed the highest vanadium permeability of 110.1 × 10^7 cm^2/min possibly due to the highest IEC and swelling ratio. The BP-ArSA

membrane exhibited markedly lower vanadium permeability of 13.5 × 10^7 cm^2/min, thus indicating that the incorporation of an aromatic group and ether linkage in the side chain can greatly improve the vanadium ion rejection properties of the membrane. BP-ArF4 with longer -CF_2 pendant chains further suppressed the vanadium ion permeability to 10.2 × 10^7 cm^2/min, a value 4.0 times and 3.2 times lower than those for Nafion 212 and Nafion 117, respectively. Hydrated vanadium ion and proton transport in the sulfonated aromatic polymers have been found to be severely affected by the dimension of the separated hydrophobic and hydrophilic domains between their chain structures[101]. Swelling ratios for BP-ArSA (12.9%) and BP-ArF4 (10.2%) were significantly lower than for BP-SA (18.6%), suggesting a smaller extension of the aqueous domains within the polymer matrix. We also tested BPN1, an AEM with an almost identical molecular structure of BP-SA, to investigate the structure-performance relationship of the sulfonated vs. quaternary ammonium aromatic polymer membranes. BPN1 also showed a significantly lower vanadium permeability (23.8 × 10^7 cm^2/min) than BP-SA, because its highly concentrated positive quaternary ammonium functional groups are expected to decrease the permeability of the multi-valent vanadium cations, based on the Donnan exclusion model.

The IEC values of the BP-SA (2.29 meq./g) and BP-ArSA (2.01 meq./g) were more than twice those of Nafion 117 and Nafion 212 (0.89-0.90 meq./g); the concentration of ionic groups is significantly higher for BP-SA and BP-ArSA compared to Nafion. As expected, the proton conductivity values of CEMs increased with IEC in the order BP-ArF4 < BP-ArSA < BP-SA (Table 2). The proton conductivity of the BP-ArSA and BP-SA membrane was 75.8 and 86.3 mS/cm, which are higher than those of Nafion 117 (59.2 mS/cm) and Nafion 212 (73.5 mS/cm). Although BP-ArF4 showed lower proton conductivity (57.6 mS/cm) than BP-ArSA and BP-SA, the proton conductivity is comparable to that of Nafion 117.

We express the ion selectivity (α) of the membranes by the ratio of proton conductivity and vanadium permeability (α, $\times 10^{-4}$ min·S/cm^{-3}). The ion selectivity values of BP-ArF4 and BP-ArSA were approximately 3 times higher than that of Nafion membranes. Areal specific resistance (ASR) values of all prepared membranes were measured with electrochemical impedance spectroscopy (Table 2). In a bulky solution, the ionic currents are mostly carried by migration instead of diffusion, the later commonly take place near the carbon electrode surface. For CEM, the ASR of membrane predominantly refers to proton transport. Although vanadium ion can also pass through CEM, the transference number of vanadium ion is considered to be much lower than protons, owing to the lower concentration (~1/5 of proton) and the much smaller diffusivity (more than two orders of magnitudes lower than proton, Table 10) in IEM. Of note, the transference number is depending on concentration and diffusivity of ions. On the other hand, the ASR of the BPN1 AEM sample was measured for SO_4^{2-} ion transport instead of proton, since proton transport through AEM is excluded by means of Donnan effect. The ASR values of prepared biphenyl sulfonated CEMs decreased with increasing IECs (BP-SA < BP-ArSA < BP-ArF4). Notably, the ASR values (0.23–

0.28 Ω cm^2) were significantly lower than that of Nafion 117 (0.89 Ω cm^2), currently the standard CEM in VRFB, because of their higher conductivity and lower membrane thickness (195 μm for Nafion 117 vs. 60–90 μm for biphenyl CEMs). As expected, the ASR of BPN1 (0.67 Ω cm^2) was almost three times higher than that of CEMs with similar thickness, owing to the intrinsically low mobility of SO_4^{2-} (8.27×10^{-8} m^2 s^{-1} V^{-1}) in aqueous solution, which is approximately one-fourth that of protons[102].

Table 2. IEC, VO^{2+} permeability, proton conductivity, ion selectivity, and area resistance of membranes.

Samples	Thickness (μm)	IEC (meq./g)	VO^{2+} Permeability ($\times 10^{-7}$ cm^2/min)	Ionic Conductivity (mS/cm)	α ($\times 10^4$ min • S/cm^{-3})	Area resistance (Ω cm^2)	Linear Swelling Ratio (%)
BP-ArF4	88±1	1.25±0.05	10.2±0.8	55.3±1.2[a]	5.42	0.28±0.02	10.2
BP-ArSA	90±1	2.01±0.06	13.5±0.5	67.6±0.9[a]	5.08	0.26±0.02	12.9
BP-SA	60±2	2.29±0.19	110.1±2.5	94.4±2.1[a]	0.75	0.23±0.01	18.6
BPN1	97±2	2.60±0.05	23.8±3.4	14.5±1.4[b]	0.61	0.67±0.07	17.4
Nafion 212	55±1	0.90±0.02	41.2±2.0	73.5±3.1[a]	1.78	0.23±0.05	14.3
Nafion 117	195±1	0.89±0.02	32.1±1.7	59.2±2.2[a]	1.84	0.89±0.09	15.1

[a]Cation conductivity. [b]Anion conductivity.

3.2.2 Battery performance evaluation

Figures. 5a-c indicate that VRFB single cell tests with BP-ArF4 as a membrane separator showed the best overall performance among all membranes examined, including Nafion 117, the most commonly used benchmark separator membrane. Because the transport of vanadium species may occur through diffusional processes even in the absence of current, coulombic losses are expected to dominate at low current density, whereas VE is expected to decrease with increasing charging/discharging current, owing to the charge transfer resistance and transport limitations within the anolyte and catholyte (**Figures. 4a & b**). Nafion 212, BP-SA, BP-ArSA, and BP-ArF4 have similar ranges of ASR (0.23–0.28 Ω cm^2), and they all showed higher VE than that of Nafion 117, which has an ASR of 0.89 Ω cm^2. The positive effects of ion selectivity of newly developed IEMs on VRFB performance were more clearly visible in CE. Among all tested membranes, the CE of VRFBs with BP-ArF4 membrane approached 100% at a current density > 60 mA/cm^2. Even at the lower current density of 40 mA/cm^2, the BP-ArF4 membrane still exhibited a very high CE of 98.6%, as compared with 95.0% for Nafion 117 and 85.9% for Nafion 212. Notably, the CE of BP-ArF4 was even higher than 96.2% of BPN1 at 40 mA/cm^2. We also evaluated cycle stability and chemical stability of the BP-ArF4 membranes in oxidative/acidic V^{5+}/H_2SO_4 solution. The CE of BP-ArF4 samples remained nearly constant (close to 100%) and highly stable during 200 charge-discharge cycles at 60 mA/cm^2, thus indicating negligible crossover of vanadium ions through the membrane during the operation and good chemical stability under the strong oxidizing and acidic environment (**Figure. 4d**). According to the results of the chemical stability tests, all prepared CEMs showed significantly less V^{4+}

generation than other hydrocarbon PEMs such as BPSH60 [12] (**Figure. 5**). Among three biphenyl-based CEMs, BP-SA showed the highest chemical resistance against oxidation, to an extent similar to Nafion. Both the battery cycling test and off-cell stability test provided strong evidence that our CEMs are stable in VRFBs during long-term operation.

Since CE and EE values of the BP-ArF4, BP-ArSA, BPN1, and Nafion 212 are similar at 100 mA/cm^2 (**Figure 5. b&c**), we additionally monitored capacity retention of the IEMs to further evaluate their performance, particularly at the high current density. VRFB single cell loaded with the IEMs were charged and discharged at 100 mA/cm^2 for 200 cycles. As shown in **Figure. 5e**, the capacity decay rate of the BP-ArF4 membrane is lowest (0.08% per cycle) followed by BP-ArSA (0.16%), Nafion 117 (0.29%), BPN1 (0.36%), Nafion 212 (0.44%), and BP-SA (0.49%). The capacity decay of VRFB cell is typically a result of the charge imbalance due to the crossover of vanadium ions as well as water transfer [91]. Benefiting from remarkably lower vanadium permeability and swelling ratio of BP-ArF4 and BP-ArSA, these membranes exhibited slow capacity decay rate and high capacity retention after 200 cycles, 84% and 67%, respectively. In contrast, BP-SA and Nafion 212 showed faster capacity decay and lower capacity retention, presumably

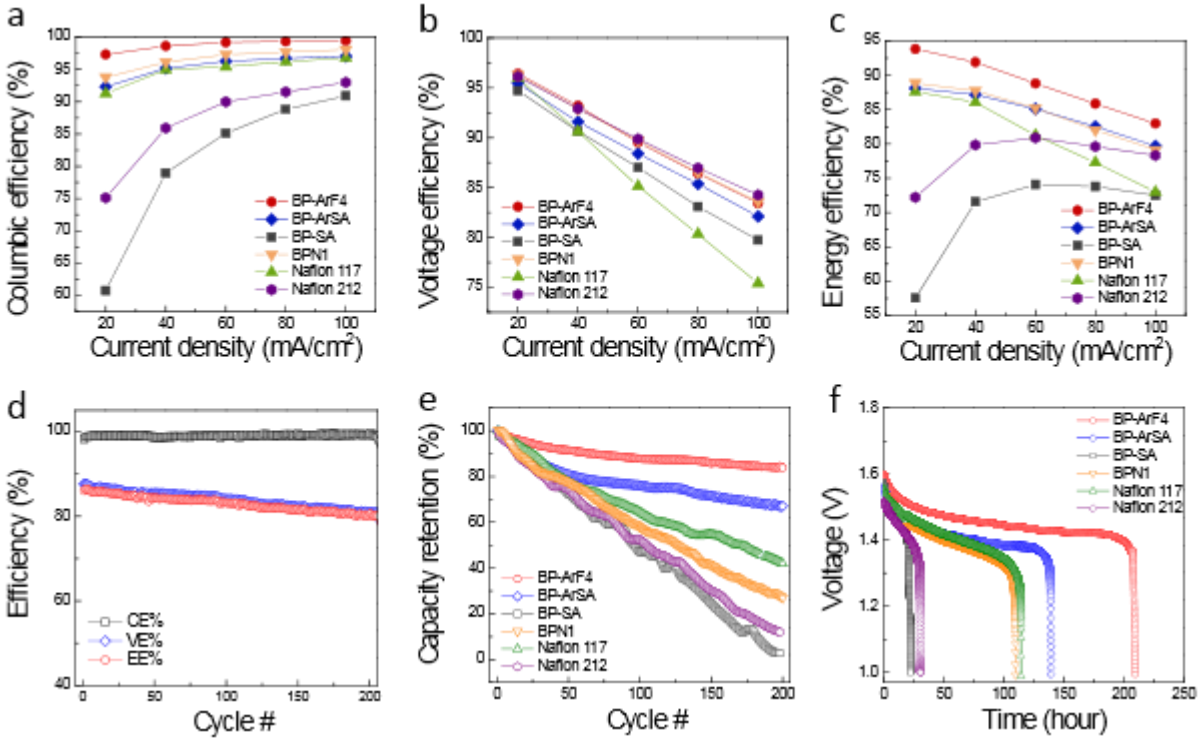

Figure 5. (a) CE for PEMs at a current density from 20 to 100 mA/cm^2. (b) VE for PEMs at a current density from 20 to 100 mA/cm^2. (c) EE for PEMs at a current density from 20 to 100 mA/cm^2. (d) cycle stability of VRFB with BP-ArF4 membrane at 60 mA/cm^2. (e) capacity retention for IEMs at 100 mA/cm^2. (f) self-discharge curves of PEMs.

due to the more rapid vanadium and water crossover which can deteriorate the charge imbalance between positive and negative half cells. In addition, we evaluated the self-discharge rate of the IEMs which is

closely related with the VRFB lifetime[103]. **Figure. 5f** shows self-discharge curves of VRFB with IEMS starting from ~80% of state of charge. Due to the crossover of active vanadium species through the IEMs,

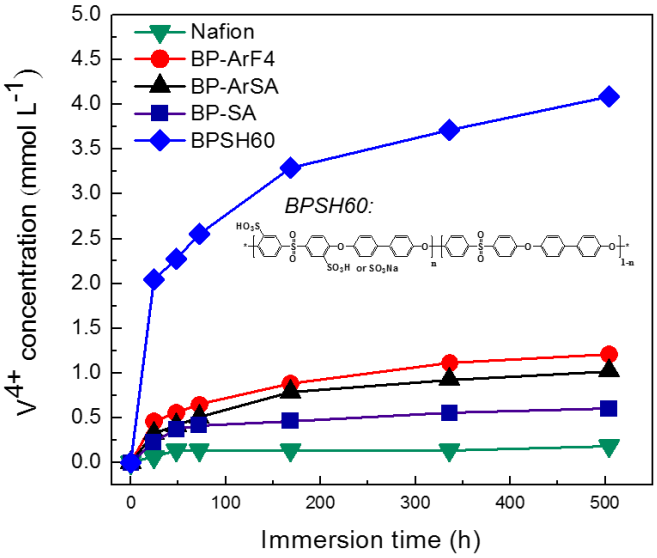

Figure 6. Chemical stability test results show increase of V^{4+} ions concentration with time of electrolyte (0.1 M V^{5+} in 4.0 M H_2SO_4) solutions containing IEMs at room temperature. We also compare our biphenyl-based sulfonated membranes with another hydrocarbon PEM, BPSH-60.

open circuit voltage (OCV) of all VRFB tests gradually decreased over time. At the end of each test, the OCV sharply decreased to below 1.0 V. With 1.0 V as a cut-off voltage, BP-ArF4 showed the longest self-discharge time (209.5 hrs) among all tested IEMs: BP-ArSA (139.5 hrs), Nafion 117 (114.5 hrs), BPN1 (109.9 hrs), Nafion 212 (30.5 hrs), and BP-SA (22.2 hrs). It is important to note that the 90 μm-thick BP-ArF4 membrane shows almost twice longer self-discharging time than 195 μm-thick Nafion 117, owing to its superior ability to mitigate vanadium crossover. In overall, the results of the capacity retention and self-discharge tests agree well with vanadium permeability test results (Table 2).

3.2.3 SAXS and DFT studies: selective ion transport mechanism

On the basis of a recent work on selective ion transport[104, 105], we suggest that the high battery performance of BP-ArF4 is mainly due to its unique morphology and optimum ion exchange capacity. When equilibrated with a 1.6 M $VOSO_4$/4 M H_2SO_4 electrolyte, the hydration number (swelling) of CEMs was low (Table 2) and a substantial amount of co-ions (here sulfate anions) entered the membrane with a corresponding amount of counter-ions (mostly H_3O^+ and vanadyl species). Interestingly, there was a strong indication that VO^{2+} counter-ions were well hydrated and dissociated (they did not bind to the $-SO_3^-$ fixed ionic group), whereas excess VO^{2+} was strongly associated with SO_4^{2-} co-ions by forming neutral $VOSO_4$ species within the aqueous domains of the CEMs. Then, vanadium crossover mainly occurred through $VOSO_4$ diffusion, with a minor contribution from charged vanadium species, whereas the major contribution to the ionic current through the membrane was carried by protons, which were present as

counter-ions and part of the excess H_2SO_4 entering the membrane as a consequence of the breakdown of Donnan exclusion at high acid concentrations (i.e., 4 M H_2SO_4). We also demonstrated that the transport of vanadium containing species was largely decreased when the extension of aqueous domains fell below the hydrated sizes of these species (sieving-effect), which was also observed in subnano-sieving PIM-1 membrane[106]. This effect began to occur at a domain width of approx. 0.7 nm, which remained wide enough for rapid local H_3O^+ diffusion.

With their pronounced hydrophobic/hydrophilic separation, as indicated in Table 2, perfluorosulfonic acid membranes, Nafion 117 and Nafion 212, have much wider aqueous domains, even despite the low swelling in highly concentrated electrolytes (i.e., 1.6 M $VOSO_4$/4 M H_2SO_4), thus explaining their low CE values. In contrast, the flexible and long side-chains of Nafion efficiently decouple hydrophobic aggregation within the polymeric domain from ionic ordering and water coalescence within the aqueous ionic domain, thus leading to a relatively smooth interface between the two domains and good connectivity of the aqueous ionic domain. Consequently, even with low IEC, Nafion membranes show less of a conductivity decrease than other IEMs as hydration decreases[107]. With respect to low hydration conditions, such as those in VRFBs, relatively high proton conductivity can still be achieved, thus leading to high VE for a given current density (**Figure. 5b**). Therefore, a key design criterion for obtaining both high CE and VE is the morphology of the IEMs, which should have narrow aqueous ionic domains that efficiently block the transport of vanadium species (e.g., $VOSO_4$, $VO^{2+}_{aq.}$, $VO_2{}^{+}_{aq.}$, $V^{3+}_{aq.}$, $V^{2+}_{aq.}$) yet are still wide enough and are well-connected for high proton conductivity. To investigate how the structural correlation lengths and degree of order/disorder affect ion selectivity and VRFB performance, we recorded SAXS patterns for CEMs immersed in 1.6 M $VOSO_4$/4 M H_2SO_4 **(Figure. 7)**[108]. Together with the water volume fraction, these parameters allowed us to estimate the width of the aqueous ionic domains, d_{aq}, including its dispersion. The estimation is based on the assumption that the morphology of all membranes under consideration is locally flat, thus implying that[108]:

$$d = d_{poly} \times \left(1 + \frac{V_{aq}}{V_{poly}}\right) \qquad Eq.1$$

where d is the structural correlation length, as obtained from the position of the ionomer peak in q space, d_{poly} is the width of the polymeric domains, and V_{aq} and V_{poly} are the volume fractions of the aqueous ionic domain and the polymeric domain, respectively. Then, d-$d_{poly.}$ can be a good estimate of the width of the aqueous ionic domain, $d_{aq.}$. The relevant data are also shown in Table 2. BP-ArF4 has the unique molecular structure of a hydrocarbon backbone and flexible pendant side chains with a perfluorinated terminating part. Although the BP-ArF4 membrane does not show the smallest structural correlation length d, its d_{aq} is the smallest as compared with other membranes, owing to its lower water volume fraction,

essentially reflecting the low IEC. Notably, the ionomer peak of the BP-ArF4 is relatively narrow, and the second order peak is clearly visible (**Figure. 7b & 3c**), thus indicating a well-ordered morphology with a narrow distribution of the aqueous ionic domain width. This finding may be a reason for its superior blocking properties for vanadium species, thus leading to the highest CE over the entire current densities (20–100 mA/cm^2). On the other hand, the VE is still reasonably high, i.e. the trade-off between CE and VE leads to a better compromise than for other types of membranes. The reason is probably the combination of properly sized aqueous ionic transport pathways and the high degree of order. The morphological "sieving" effect can be characterized by a relatively distinct threshold with respect to the width of the aqueous ionic domain[107]. It is the very nature of this effect that only a narrow distribution of this width allows for a high blocking effect close to the percolation threshold. Otherwise, one had to further reduce the average width of the transport pathways as to avoid transport through the fraction of wider parallel pathways. This would further reduce proton conductivity which is also highest for a narrow domain width distribution because of the non-linear dependence of the water diffusion coefficient on the water volume fraction (domain width)[107]. The morphology of the BP-ArF4 membrane seems to provide both properly sized aqueous ionic domains and a high degree of order. The molecular structure of this ionomer represents

the rare case of a hydrocarbon backbone with flexible pendant side chains with perfluorosulfonate terminating group (refer chemical structure of BP-ArF4 in **Figure. 2**).

We further investigated transport phenomena of vanadium species in two extreme cases of Nafion 117 (the largest d_{aq}) and BP-ArF4 (the smallest d_{aq}) by estimating $VOSO_4$ transport rates. Because both membranes enabled complete exchange into VO^{2+} form in an excess of 0.1 M $VOSO_4$ with limited uptake of excess $VOSO_4$ (< 10% of the fixed ion concentration), the total conductivity mainly represented the mobility of $VO^{2+}_{aq.}$ in both structures (the volumetric density of ionic groups in both membranes was very

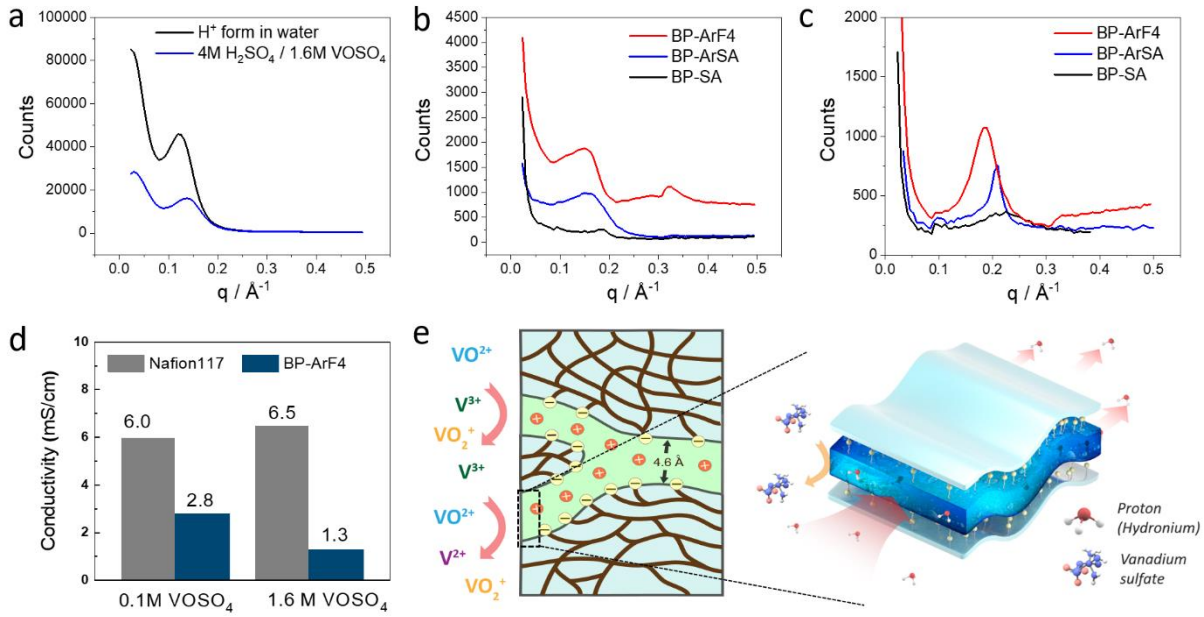

Figure 7. SAXS patterns of: (a) Nafion 117 in water and 4 M H_2SO_4/1.6 M $VOSO_4$. (b) BP-ArF4, BP-ArSA, and BP-SA membranes in the acid-form immersed in water and (c) equilibrated in a 1.6 M VO_2SO_4/4 M H_2SO_4 electrolyte. (d) total room temperature conductivity of a Nafion 117 and BP-ArF4 membrane equilibrated in solutions of $VOSO_4$ with different molarity. (e) illustration for the selective ion transport mechanism of BP-ArF4 membrane. The narrow aqueous ionic channel (0.48 nm) and functionalities of the BP-ArF4 can efficiently block $VOSO_4$ transports, while keeping high proton conductivity.

close, i.e., approximately 1.9 meq./ml). As shown in **Figure. 7d**, the total conductivity of BP-ArF4 (2.8 mS/cm) was lower than that of Nafion 117 (6 mS/cm) by approximately a factor of two. A more interesting observation was that the increase in the $VOSO_4$ concentration from 0.1 to 1.6 M left the total conductivity of Nafion 117 unchanged while the value of BP-ArF4 largely decreased to 1.3 mS/cm. In the highly concentrated electrolytes, we observed a substantial amount of co-ion (SO_4^{2-}) uptake, mainly from neutral $VOSO_4$ and diminished water uptake (approximately 10%) as a response to the decreased water activity in the electrolyte solution. Thus, in more highly concentrated electrolytes with a further decrease in the membrane's hydration, the conductivity contribution of vanadium species (e.g., VO^{2+}) can be further decreased in the BP-ArF4 after its de-swelling, because less swelling can decrease the width of the aqueous

ionic domain to an extent (e.g., 0.48 nm as a lower bound in Table 3) that substantially impedes vanadium ions, whereas protons still can be transported through the channels. This result is consistent with the recent molecular dynamics simulation studies, which suggests that zeolites-based IEMs with < 0.5 nm is indicative of the selective hydronium ion transport over vanadium ions[109].

DFT calculation results provided additional insights into vanadium ion transport in terms of the chemical functionalities of polymer chains. A previous study has reported that the vanadium (IV) ion in sulfuric acid solution forms a $[VO(SO_4)(H_2O)_4]H_2O$ complex[110]. Our further optimized vanadium ion structures indicated that the energetics of the vanadium ion was lowest when its spin state was doublet (**Figure 8**), and its structural parameters such as the V=O bond length or V-O bond length were in good agreement with previously reported values[111]. Table 3 lists the interaction energies of the vanadium ion complex with different moieties of BP-ArF4 and Nafion (detailed calculation methods and optimized structures of IEMs can be found in the SI). The interaction energies between BP-ArF4 and vanadium ion were in the range of 22.6–33.8 kcal/mol, which are higher those of Nafion (13.7 and 21 kcal/mol). The higher interaction energy is due to strong binding energy through π---H or π---F hydrogen bonding in BP-ArF4 and vanadium ion complexes (**Figure 9**), thus hindering the diffusion of vanadium ion through the polymer membrane. Among several complexes, comp3-BP-ArF4, whose optimized structure is depicted in **Figure 10**, showed a remarkably large binding energy (33.8 kcal/mol). In this complex, three hydrogen atoms of the vanadium ion interact with the fluorine atom of BP-ArF4, which should contribute to the interaction to a large extent. In addition, one hydrogen atom (H_D) interacts with the neighboring aromatic moiety. The formation of three hydrogen bonds between the vanadium ion and BP-ArF4 arises from flexibility of the $-CF_2CF_2OCF_2CF_2SO_3H$ chain attached to the benzene ring. In contrast, the interaction of Nafion with vanadium complexes occur around its fluorine atoms, owing to the absence of aromatic ring in the backbone or side chains (**Figure 10**). All complexes of Nafion showed that two hydrogen atoms of the vanadium complex interact with Nafion's $-CF_3$ group; thus, the computed binding energies indicated that the interaction between Nafion and the vanadium complex is weaker than that of BP-ArF4. Although the fluorine atoms in the $-CF_3$ group typically have a sizeable negative charge, their hydrogen bonding ability with hydrogen donor molecules is rather weak[112].

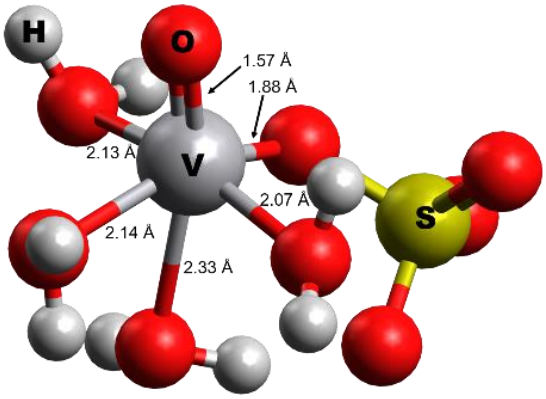

Figure 8. Optimized structures of $VO(SO_4)(H_2O)_4$

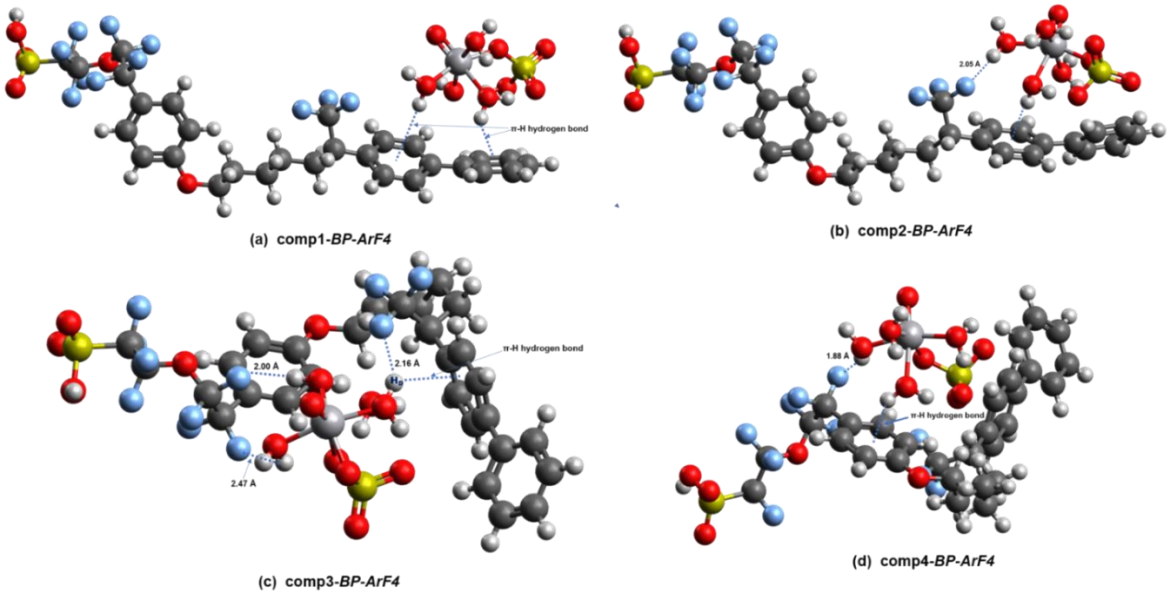

Figure 9. Optimized structures of BP-ArF4 --- vanadium ion complexes

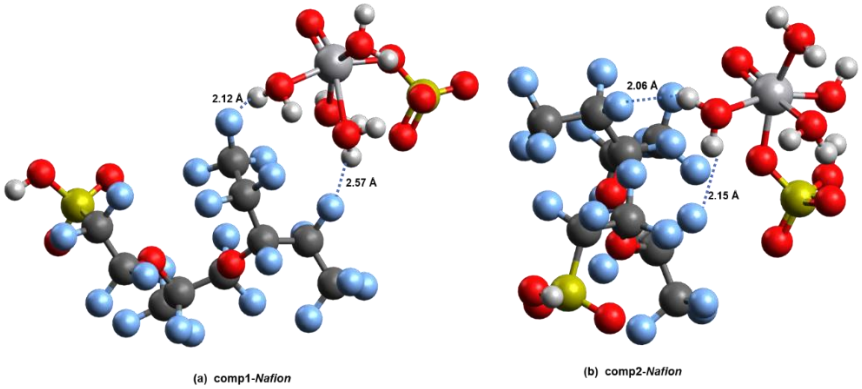

Figure 10. Optimized structures of *Nafion* --- vanadium ion complexes

As illustrated in **Figure. 5e**, the anomalously high ion selectivity properties and VRFB performance of BP-ArF4 might have resulted from the synergistic effects of its unique morphology and functionalities in its polymer chain which greatly hinder the vanadium ion transports, while keeping high proton conductivity. Thus, the resistance for transporting vanadium ion in BP-ArF4 is higher than in Nafion. We also investigated the differences of $VOSO_4$ transports in BP-ArF4 and Nafion 117 by experimentally measured activation energy. The activation energies for $VOSO_4$ transport of BP-ArF4 and Nafion 117 membrane were calculated from Arrhenius plots by measuring the $VOSO_4$ diffusivity at different temperatures. In Table 4, the activation energy of the BP-ArF4 (9.14 kcal/mol, 0.40 eV) was 2 times larger than that of Nafion 117 (4.5 kcal/mol, 0.20 eV) and Nafion 212 (5.4 kcal/mol, 0.23 eV) suggesting that the morphology and functionalities of BP-ArF4 create much higher energy barrier for vanadium transports in BP-ArF4, similar to the results observed from the $VOSO_4$ transports in 1.6 M $VOSO_4$ electrolyte and interaction energy differences.

Table 3. Binding energy between the vanadium ion/BP-ArF4 and vanadium ion/Nafion

Complexes	Binding Energy (kcal/mol)
comp1-*BP-ArF4*	23.9
comp2-*BP-ArF4*	22.6
comp3-*BP-ArF4*	33.8
comp4-*BP-ArF4*	26.3
comp1-*Nafion*	13.7
comp2-*Nafion*	21.0

Table 4. Activation energy of Nafion 117, Nafion 212 and BP-ArF4 obtained by measuring vanadium ion permeability at different temperature.

Membrane	Activation Energy (kcal/mol)
Nafion 117	4.53
Nafion 212	5.40
BP-ArF4	9.14

3.2.4 Surpassing the trade-off limitations in IEMs

Finally, to correlate the high battery performance with the ion transport properties of our best membrane, we compared the ion selectivity-membrane resistivity trade-offs of BP-ArF4 with other high-performance CEMs and AEMs reported to date. Of note, mixed matrix membranes, blended membranes, and nanocomposite membranes in which the performance of IEMs were modified with other components or enhanced by thickness optimization are not included in the comparison because it is more reasonable to

compare the performance of BP-ArF4 only with a single component, free-standing membranes. For example, the reported low areal resistance (3.9×10^{-2} Ω·cm^2) and high ion conductivity (0.27 S/cm) values of the polyamide (PA) thin-film composite membrane were calculated by normalizing the resistance and conductance with the entire thickness of the composite membrane (support layer + PA selective layer) rather than using thin selective PA layer[113]. However, one should know that the intrinsic resistivity and ion conductivity of the PA layer are ~706 Ω·cm and 1.4×10^{-3} S/cm, respectively.

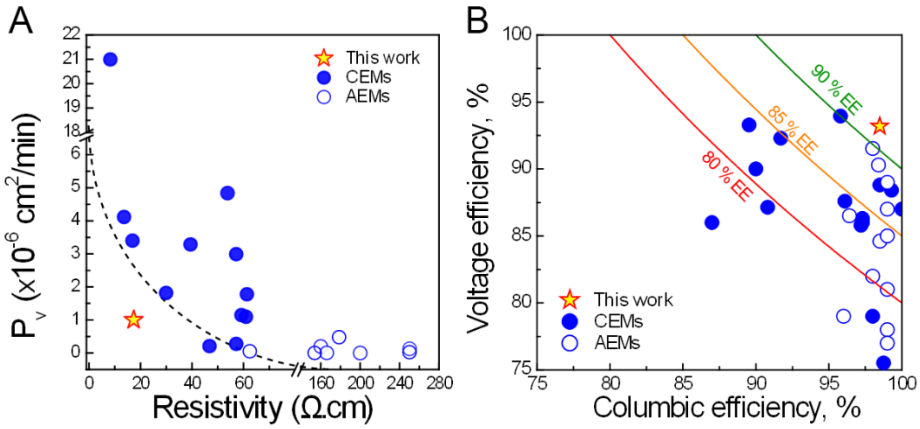

Figure 11. Trade-off curves of ion transport properties and battery performance. (a) Trade-off between vanadium diffusivity and resistivity. (b) VRFB performance relationships among CE, VE, and EE at 40-60 mA/cm^2.

As shown in **Figure. 11a**, the BP-ArF4 has the best combination of low membrane resistivity and low vanadium permeability outperforming all other reported CEM and AEM materials: generally, CEMs show low resistivity and high vanadium permeability while AEMs show high resistivity and low vanadium permeability. Surprisingly, the performance of BP-ArF4 overcomes the conventional trade-off limitation of ion selectivity and conductivity of IEMs. The efficiency of VRFB is largely affected by the transport properties of the IEMs in various ways. Typically, IEMs must efficiently separate electrochemically active ionic species (e.g., different vanadium species in anolyte and catholyte) while highly conducting other ionic species (e.g., protons) to mediate electrochemical reactions. Losses in ion selectivity results in vanadium cross-over and increases the ohmic resistance of IEM. Thus, the high proton selectivity over vanadium ions of BP-ArF4 demonstrates its great potential for application in VRFBs. Indeed, **Figure. 11b** shows a trade-off relationship between CE and VE which is similar to the ion selectivity/conductivity trade-off: except for a few examples, IEMs with high VE tend to show low CE due to high cross-over of vanadium species and *vice versa*. However, BP-ArF4 membrane illustrates a remarkable combination of high CE with high VE, resulting the highest EE over the entire current density ranges. It outperforms all CEMs and AEMs for VRFB systems reported to date and breaks the trade-off limitation on battery performance due to highly selective vanadium ion/proton transport.

3.2.5 Summary

In summary, we developed a series of novel sulfonated aromatic polymer membranes that have a good combination of high proton conductivity and ion selectivity, and overcome the conventional proton conductivity-selectivity trade-off. The effects of the pendant group structure on the membrane ion selectivity and battery performance were investigated. The incorporation of aromatic moiety on the pendant groups effectively improved the proton conductivity and selectivity. The membrane with aromatic pendant groups (BP-ArF4) showed three times higher vanadium/proton ion selectivity than Nafion, the standard CEM in VRFB. As a result, the VRFB single cell equipped with the BPAr-F4 membrane showed significantly better efficiencies, and its performance overcomes the CE and VE tradeoff curves, outperforming all other IEMs reported to date. SAXS and DFT calculation studies revealed that the narrowly distributed aqueous ionic domain width of BP-ArF4 and the strong interaction between BP-ArF4 and vanadium ion complexes through π---H or π---F hydrogen bonding synergistically improve H^+/V ion selectivity. Our study suggests an effective path toward the design of high-performance IEMs that can overcome the trade-off of ion selectivity/conductivity in many other energy conversion and storage systems. In addition, these IEMs could be used as base matrix materials for the development of novel nanocomposite membranes which can further improve the energy efficiencies of the systems.

3.3 Poly(terphenylene) Anion Exchange Membranes (AEMs)

Among many efforts to improve anion conductivity and the chemical/mechanical stability of AEMs, quaternary ammonium functionalized AEMs have been most extensively studied, owing to their facile synthesis procedure and flexible design [114-117]. Recently, we developed a new class of terphenyl-based polymeric membranes with quaternary ammonium group terminated side chains, *p*-TPN1 (para-terphenyl) and *m*-TPN1 (meta-terphenyl), and demonstrated their high hydroxide anion conductivity as well as improved fuel cell performance [90]. The unique microstructure and morphology of these AEM significantly enhance anion conductivity, thus resulting in superior fuel cell performance. Nevertheless, the performance of these promising polymers in VRFB applications has not yet been studied.

In this study, we systematically investigated how molecular structures of poly(terphenylene)-based AEM (terphenyl-based *p*-TPN1 and *m*-TPN1) affected VRFB performance. In addition, we compared the results of terphenyl-based AEMs with biphenyl-based AEM (BPN1-100) to investigate the effects of polymer backbones on ion transport properties, electrochemical performance, and membrane stability. The *p*-TPN1 and *m*-TPN1 membranes exhibited orders of magnitude lower vanadium ion diffusivity and higher proton/vanadium ion selectivity (16.31 for *p*-TPN1 and 10.29 for *m*-TPN1) than commercial Nafion (0.58)

and FAP-450 (0.81) membranes. Consequently, the VRFB with *p*-TPN1 showed an excellent energy efficiency (EE) of 86.07% at current density of 80 mA/cm^2, compared with ~78% for Nafion 212 and FAP-450.

3.3.1 Membrane properties

The molecular weights of the polymers are measured from alkyl bromide-containing neutral precursor polymers instead of the quaternary ammonium-containing polymers. This is because the presence of ionic groups in the polymers tends to form polymer aggregates and results in complicated and unreliable molecular weight characterization in size exclusion chromatography (SEC) [118]. *p*-TPBr, *m*-TPBr and BPBr-100 are the precursor polymers of *p*-TPN1, *m*-TPN1 and BPN1-100, respectively, and their SEC results are listed in **Table 5**.

Table 5. Properties of precursor polymers

Samples	Mn (kDa)	Mw (kDa)	PDI	DF (%)
***p*-TPBr**	50	94	1.9	100
***m*-TPBr**	41	126	3.1	100
BPBr-100	45	86	1.9	100

The number- and weight-average molecular weights of polymers were determined by SEC on a Viscotek T60A instrument with a differential refractive index detector (Viscotek 302), using THF as the eluent and polystyrene as the standard.

The results of IEC, WU, vanadium permeability (P_{VO2+}), conductivity, and ASR are listed in **Table 6**. In general, a higher IEC value is required for IEMs to provide satisfactory conductivity. The IEC values of all prepared AEM membranes were in the range of 2.13–2.6 meq./g, which are higher than those of the commercial AEM (0.89 meq./g of FAP450) and PEM (~0.9 meq./g of Nafions). However, the WU values of two terphenyl-based membranes (*p*- and *m*-TPN1) were significantly lower than that of the biphenyl BPN1-100 membrane. We speculate that the lower WU values of the *p*- and *m*-TPN1 membranes might be resulted from the higher hydrophobicity and rigidity of the terphenyl polymer backbone. In general, increasing the WU value of IEMs results in enlarged aqueous channels and greater electrolyte uptake [119, 120], which could enhance the transport of charge carriers. However, the increase in ion channel sizes in IEMs also facilitates active species crossover, thus decreasing the selectivity of IEMs (e.g., H^+/VO^{2+}). In addition, membranes with larger WU values usually exhibit poor dimensional stability. Thus, optimization of the WU is required to balance the ion permeance and mechanical properties of a membrane.

As presented in **Table 6**, the conductivity values of AEMs tended to increase with IEC and WU. However, we also found that the PEMs had higher conductivity values than those of AEMs despite having lower IEC.

This finding may have resulted from the intrinsically low mobility of SO_4^{2-} ions (8.27×10^{-8} $m^2s^{-1}V^{-1}$) in aqueous solution, which is approximately one-fourth the mobility of protons [102]. The higher conductivity of BPN1-100 compared with *p*- and *m*- TPN1 may have been a result of both its high WU and IEC, as mentioned above. Of note, however, although conductivity can reflect the ion transport properties of membranes, the voltage efficiency of a battery is more affected by the areal resistance (inverse to ionic conductance), which is a function of membrane thickness. Through optimization of the thickness of the prepared AEMs, the ASR values (0.22–0.29 $\Omega \cdot cm^2$) became comparable to that of Nafion® 212 (0.23 $\Omega \cdot cm^2$). This result was also evidenced in the overlapping EIS curves of the poly(terphenylene)-based AEMs (*p*-TPN1 and *m*-TPN1) and Nafion® 212 (**Figure 12a)**. Commercial FAP-450 exhibited a larger ASR (0.72 $\Omega \cdot cm^2$) than the prepared AEMs and Nafion® 212, owing to its low IEC value. Nafion® 117 had the largest ASR among all samples, primarily because of its high membrane thickness.

Table 6. **Properties of the studied AEMs (*p*-TPN1, *m*-TPN1, BPNI-100, and FAP 450) and PEMs (Nafion 117 and 212).** Notably, the membrane conductivity was converted from through-plane area resistance values. We believe that, for AEMs, membrane conductivity is mainly contributed by the transport of anions, whereas proton transport is the predominant factor affecting PEM conductivity. In-plane proton conductivity values for Nafions can be found in our previous study [121]. α is the membrane conductivity/VO^{2+} permeability ratio, in units of $\times 10^{-4}$ min·S/cm^{-3}.

Samples	Thickness (μm)	WU %	IEC (meq./g)	P_{VO2+} ($\times 10^{-7}$ cm^2/min)	Ionic Conductivity (mS/cm)	α	ASR (Ω cm^2)
***p*-TPN1**	35 ± 1	18 ± 1	2.15 ± 0.05	0.74 ± 0.12	12.07 ± 1.96	16.31	0.29±0.03
***m*-TPN1**	35 ± 1	22 ± 1	2.13 ± 0.05	1.26 ± 0.27	12.96 ± 2.78	10.29	0.27±0.05
BPN1-100	45 ± 2	58 ± 1	2.60 ± 0.05	23.83 ± 3.40	20.45 ± 2.91	0.86	0.22±0.06
FAP-450	50 ± 1	9 ± 1	0.93 ± 0.03	7.09± 1.10	6.94 ± 1.07	0.98	0.72±0.12
Nafion® 212	55 ± 1	19 ± 1	0.90 ± 0.02	41.21 ± 2.01	23.91 ± 1.17	0.58	0.23±0.05
Nafion® 117	195 ± 1	20 ± 1	0.89 ± 0.02	32.14 ± 1.74	21.91 ± 1.18	0.68	0.89±0.09

For VRFB applications, vanadium ion permeability is a critical property of IEMs that greatly affects battery performances, such as the CE%, self-discharge rate, and capacity retention. **Figure 12b** shows that the vanadium concentrations in the permeant side of the diffusion cell with *p*- and *m*-TPN1 was scarcely noticeable, even after 10 hours of measurement, thus implying that the membranes are almost impermeable to VO^{2+} ions. In contrast, the vanadium ion diffusion rates of the Nafion® 212 and BPN1-100 membranes were much higher than those of other membranes. The VO_4^{2+} permeability of *p*- and *m*-TPN1 was an order of magnitude lower than that of commercial PEMs and FAP-450 membrane (**Table 6**). We calculated the selectivity (α) of membranes by dividing membrane conductivity by the vanadium permeability. A higher

selectivity value indicates that a membrane is more likely to transport charge-carrying ions over the active vanadium species. The *p*- and *m*-TPN1 exhibited markedly higher selectivity than Nafion® 117 and 212. For example, the selectivity of the *p*-TPN1 was 28 times higher than that of Nafion® 212. However, BPN1-100, compared with terphenyl AEMs, showed relatively poor selectivity, possibly as a result of wider water channels allowing more vanadium ion crossover. The membrane transport property results suggested that the as-prepared poly-terphenylene AEMs (*p*- and *m*-TPN1 membranes) could provide better battery performance than the commercial Nafion and FAP-450 membranes.

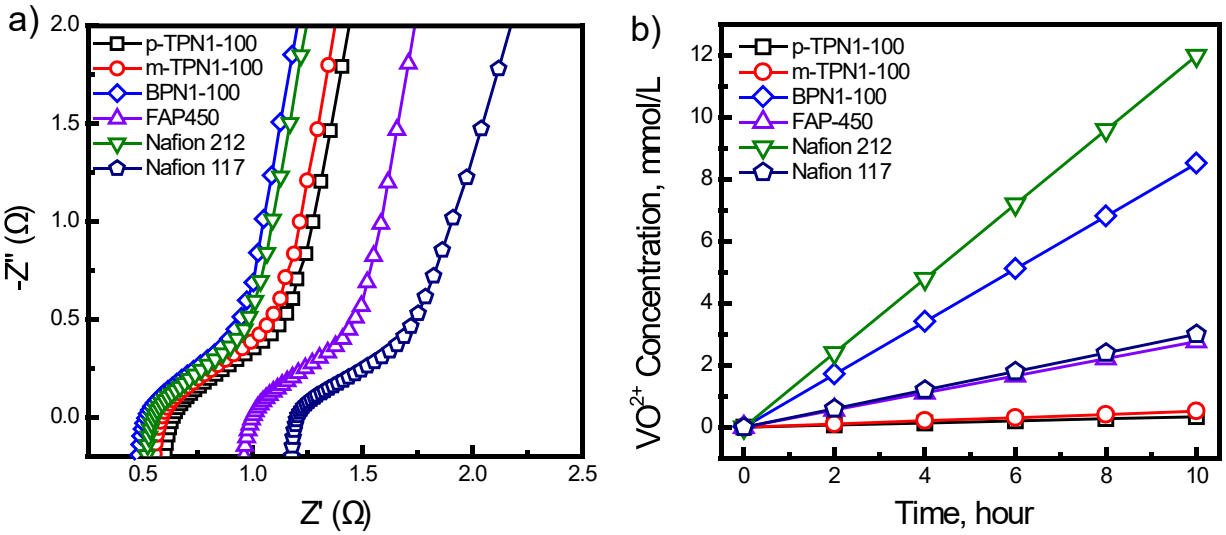

Figure 12. (a) EIS curves for the area resistance measurement, the experiment was carried out far below the reaction potential window (1.2V-1.6V) to exclude the effect of reaction on the measuring result. and **(b)** increase in vanadium ion concentrations during the vanadium ion diffusion tests for different AEMs and PEMs.

3.3.2 VRFB single cell performance

To evaluate the VRFB performance of the membranes, we tested VRFB single cells loaded with all prepared AEM membranes at current densities ranging from 20 to 100 mA/cm^2 (**Figure 13**). Fumasep® FAP-450, a commercial AEM widely used in many VRB applications [122, 123], and Nafion® 212 were also evaluated as reference samples. All membranes used in this study had similar thicknesses (35–50 μm), and the data for each current density were averaged from three independent tests.

As depicted in **Figure 13**, the CE values of all tested membranes decreased at lower current densities because of the increased charging/discharging time, which allowed for more active species crossover. In contrast, the VE tended to increase at lower current density because of the reduced ohmic loss. All tested AEMs showed higher CE than that of the proton exchange membrane Nafion® 212 (**Figure 13a**). As discussed in the diffusion test results, this finding occurred because the positively charged ion exchange groups in the AEM matrix efficiently repelled the vanadium co-ions, whereas Nafion® 212 allowed transport of positively charged vanadium ions. Among all tested membranes, VRFB with *p*-TPN1 showed the highest CE (~100% at 80 mA/cm^2), followed by the *m*-TPN1 membrane. The high CE values of *p*-TPN1 and *m*-TPN1 membranes were expected because of their extremely low vanadium permeability, as described in Table 6. In addition to the high CE, the *p*- and *m*-TPN1 as well as BPN1-100 membranes also showed excellent VE, even at high current densities. We speculate that the high VE values resulted from the synergistic contribution of high ion exchange capacity and the favorable hydrophobic−hydrophilic domains that facilitate anion transfer [90].

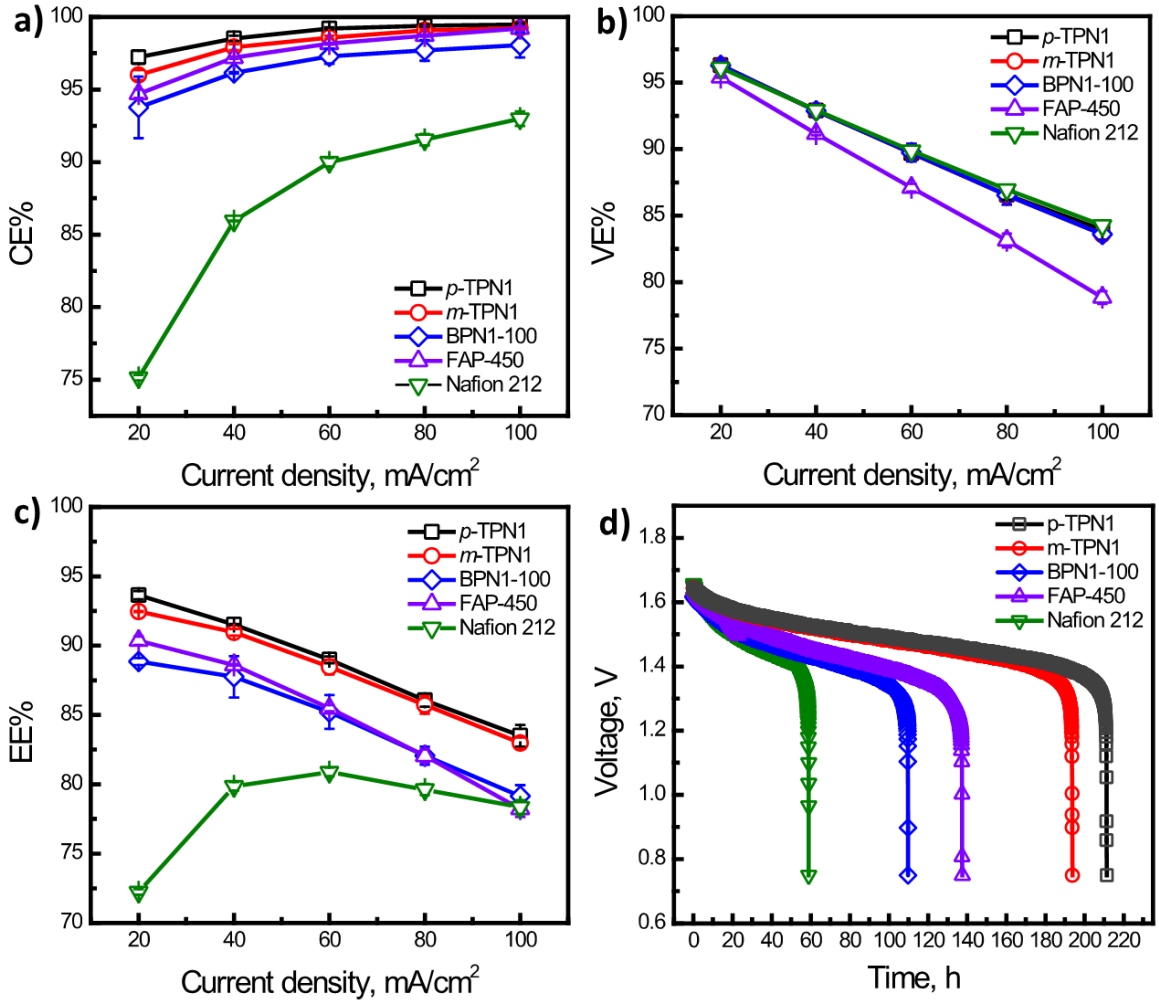

Figure 13. (a) CE, (b) VE, (c) EE, and (d) self-discharge curves of VRFB single cells with the *p*-TPN1, *m*-TPN1, BPN1-100, and FAP450 membranes at different current densities. Some error bars are hidden by the symbols.

Owing to both high CE and VE, the *p*- and *m*-TPN1 exhibited excellent EE, which is the product of CE and VE. In particular, *p*-TPN1 showed the best overall performance among all tested membranes. The highest EE value of 93.64% was achieved at the current density of 20 mA/cm^2. This is the highest EE value in VRFB performance reported to date. The commercial FAP-450 also showed good CE. However, owing to the high ASR, its VE was lower than that of other membranes, thus leading to a lower overall EE. Compared with AEMs, commercial PEMs and Nafion® 212, provide satisfactory VE but low CE and EE, especially at low current densities, because of the faster cation permeation across Nafion membranes.

Another criterion for high-performance membrane separators in VRFB is a slow self-discharge rate. To evaluate the self-discharge performance of the AEMs and PEM, we self-discharged battery single cells loaded with various membranes to 0.8 V. As shown in **Figure 13d**, the open circuit voltage of batteries with all membranes decreased gradually over the self-discharging, mainly because of crossover flux of the vanadium ions. At the end of each test, the open circuit voltage sharply decreased to less than 1 V. During the self-discharge measurement, the diffusion of vanadium ions was the major factor accounting for the active species crossover. As a result, the trend observed for the self-discharge time was in good accordance with the results of vanadium permeation tests for the membranes. At the cut-off voltage of 0.8 V, the self-discharge times of Nafion® 212, BPN1-100, FAP 450, *m*-TPN1, and *p*-TPN1 were 58.7, 109.9, 137.2, 193.7, and 211.3 hours, respectively. Among all the membranes, *p*-TPN1 membrane exhibited the longest self-discharge time (approximately 10 days). This superior performance of *p*-TPN1 further demonstrated its excellent ability to reject vanadium species, a property that is beneficial to extending the stand-by time of VRFB stacks.

Long-term VRFB cycle stability testing with the *p*-TPN1 membrane, which showed the best performance among the as-prepared AEMs, was performed for 150 cycles. For comparison, we also tested Fumasep® FAP-450 AEM and Nafion® 212 at a current density of 80 mA/cm^2. As shown in **Figure 14a**, the CE of the *p*-TPN1 membrane was stable at ~100% over the course of the testing, and the VE and EE also remained high (>85%). In comparison, although Nafion® 212

also showed stable performance, its CE (92%) and EE (80%) were lower than those of *p*-TPN1 (**Figure 14 a&c**). Fumasep® FAP-450 showed a stable CE value similar to that of *p*-TPN1. However, its VE was approximately 7–8% lower than that of *p*-TPN1, owing to its high membrane resistance. In addition, FAP-450 showed relatively less stable VE and EE than Nafion and *p*-TPN1. In **Figure 14d,** the capacity retention of VRFB single cell *p*-TPN1, Fumasep® FAP-450 and Nafion® 212 is plotted against cycle numbers. A higher capacity retention was found for of *p*-TPN1 than Nafion® 212 and FAP-450. The capacity loss per cycle for *p*-TPN1 was approximately 0.2%, whereas Nafion® 212 and FAP-450 exhibited capacity losses of 0.35% and 0.33% per cycle, respectively. The faster capacity decay of Nafion® 212 and FAP-450 may have been a consequence of the faster crossover of vanadium ions. The superior cycle stability and high capacity retention of *p*-TPN1 demonstrated its great potential for long-term operation in VRFB applications.

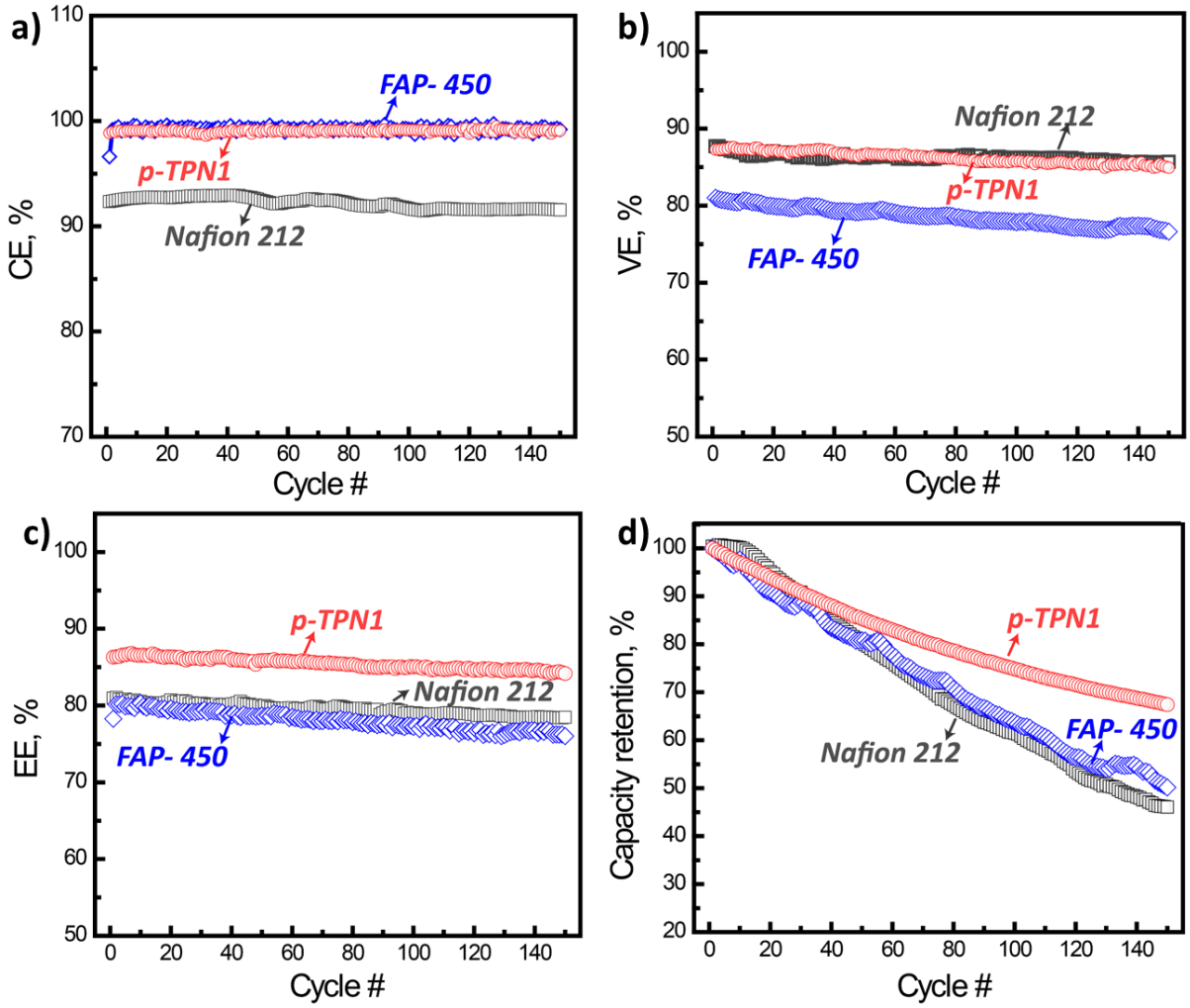

Figure 14. 1–150 cycles of VRFB single cell performance in terms of **(a)** CE %, **(b)** VE %, **(c)** EE, and **(d)** capacity decay curves with *p*-TPN1, Nafion 212, and FAP 450 membrane.

3.3.3 Summary

A series of poly(terphenylene) and biphenyl-based anion exchange membranes were fabricated and optimized for VRFB applications. These membranes exhibited both low vanadium ion crossover and low membrane resistance, owing to their well-balanced ion channel structure and functionalities. Consequently, the ion selectivity of the terphenylene-based *p*- and *m*-TPN1 membranes outperformed Nafion by 28 and 18 times, respectively. Superior VRFB single cell performance was further obtained with the prepared poly(terphenylene)-based AEMs. Among all membranes tested, *p*-TPN1 exhibited the highest overall performance at all current densities. In addition, VRFB cell cycle stability testing with *p*-TPN1 for 150 cycles showed a highly stable CE (>99%) and slow capacity decay. The results indicate that these poly(terphenylene)-based AEMs are promising candidates for development of high performance VRFBs.

IV. SELECTIVE ION TRANSPORT IN PROTON EXCHANGE MEMBRANE WITH NANO-ENGINEERING SURFACE LAYER FOR VANADIUM REDOX FLOW BATTERIES

(Previous published as Wang, T., Moon, S. J., Hwang, D. S., Park, H., Lee, J., Kim, S., ... & Kim, S. "Selective ion transport for a vanadium redox flow battery (VRFB) in nano-crack regulated proton exchange membranes." *Journal of Membrane Science* 583 (2019): 16-22.)

In the previous work, we have discussed the structure-property correlation of pure ion exchange polymers and their ion transport characteristics. In this study, we will explore the feasibility to further enhance the membrane performance by introducing a nano-patterned selective layer on the proton conductive membranes. To achieve this objective, the research work has been carried out in two steps. In the first step, we have developed a surface nano-engineered hybrid membrane with tunable ion selectivity by introducing a thin nano-cracked surface layer on the pure polymer membrane substrate (BPSH60). This work is established on the foundations previously done by our collaborators. We use this nano-cracked membrane design as a proof-of-concept for the latter development of highly selective and ultrahigh proton conductive membranes based on mono-layered film incorporated into a polymer matrix (e.g., Nafion, hydrocarbon proton exchange membrane). The first part of the work will be introduced in section 4.1. After a deeper understanding of surface nano-patterned layer and their relation to ion transport properties of IEMs was established, we have fabricated surface nano-engineered hybrid membranes with 2D graphene film as the ion selective layer. The studies on their ion transport properties and electrochemical performance in VRFBs will be introduced in section 4.2.

4.1 Selective ion transport in nano-crack regulated proton exchange membrane for vanadium redox flow battery (VRFB)

Post-sulfonated polymer membranes have been widely used as separators for many electrochemical applications because of their high mechanical strength, good oxidative stability, and low cost. A great deal of effort has been devoted to the improvement of the performance of sulfonated polymer membranes by increasing their ion exchange capacity (IEC) or introducing a microphase-separated domain structure. Chen et al.[124] prepared sulfonated poly(fluorenyl ether ketone) with an embedded silica-rich layer *via* sol-gel process exhibited higher coulombic efficiency. Ji et al.[77] reported an improved ion selectivity for

sulfonated poly(ether ether ketone) membrane by incorporating TiO_2. Chen et. al. [125]introduced fluorine groups into a poly(arylene ether) membrane (S-Radel). The membrane shows improved chemical stability in VRFB. However, these works show a trade-off relationship between the proton conductivity and vanadium ion permeability as the effort to the improvement of one property always results in the deterioration of the other. Therefore, to improve the VRFB performance using the sulfonated membranes, an alternative strategy should be employed to increase the ionic selectivity of the membrane.

Recently it has been reported that nano-crack regulated fluorocarbon plasma coating can effectively improve the ion selectivity of the IEMs by enhancing ion selectivity without sacrificing ion conductivity[12]. In reverse electrodialysis application, the nano-crack patterned hydrophobic coating layer provided sodium ion and chloride ion transport channels in this surface fluorocarbon coating layers on the surface of IEMs. This thin surface layer showed considerably enhanced ion selectivity of the BPSH with a degree of functionalization from 65% to 85%.

In this work, we demonstrate the proton/vanadium selectivity of sulfonated hydrocarbon membranes could be enhanced by employing the concept of nano-crack regulation and its potential application for the VRFB application. A thin hydrophobic layer with nano-crack structure was grown on the BPSH60 membrane surface by hydrophobic atmospheric plasma treatment. The performance of the VRFBs was tested with plasma coated BPSH membrane (P-BPSH) and Nafion® 212 and 117. The effect of nano-crack structure on the ion transport properties and the feasibility of using plasma treatment to enhance the membrane performance in VRFBs is discussed along with battery performances.

4.1.1 Materials and characterization methods

Materials. N,N-dimethylacetamide (DMAc, 99.5%) was purchased from *Daejung Chemical* (Gyeonggi-do, Korea). Octafluorocyclobutane (c-C_4F_8) and helium (He) gases were supplied from *Air Korea* (Gyeonggi-do, Korea). Commercial Nafion® 117 and 212 membranes were purchased from *Ion Power Inc*. (DE, USA). Vanadyl sulfate ($VOSO_4$, 99.9 %) and magnesium sulfate ($MgSO_4$, 99.5 %) were purchased from *Alfa Aesar* (MA, USA). Sulfuric acid (H_2SO_4, 98.0 %) was purchased from *Fisher Scientific* (PA, USA). Pristine (BPSH-60) was purchased from *Yanjin Chemical Co., Ltd* (Guangzhou, China). All membranes were tested immediately after pretreatment and chemicals were used without further purification.

Sample preparation The protonated poly(arylene ether sulfone) polymers (BPSH60) were prepared by immersing sodium-neutralized BPSH60 polymers into boiling 2 M H_2SO_4 solution for 2 hours, followed by washing with deionized water for 4 hours and drying at 100 °C for 12 hours in a vacuum oven. The BPSH60 membrane was prepared by casting solution of 15 wt.% polymer in DMAc. The dry process was carried out under ambient conditions at 100 °C for 12 hours, 120 °C for 2 hours and 150 °C *in vacuo* for 2 hours. Atmospheric plasma treatment on both sides of membranes was performed with various repeat time from 5 to 10 under RH 45 % below. Repeat time was limited to within 10 considering membrane resistances and ion permselectivity in the reverse electrodialysis (RED) application of our previous study. After being completely dried, the membrane was flattened for uniform plasma treatment. And then, the membrane was placed on an aluminum plate and slowly coated at a speed of 30 mm s^{-1} along the y-axis. The input power of the glow discharge source was 150 W and the distance from the membrane was maintained at 2.5 mm. The whole plasma treatment process proceeded at the atmospheric condition with gas flow rates of 10 mL min^{-1} of octafluorocyclobutane (c-C4F8) and 20 L min^{-1} of He gases.

Before battery test and membrane characterization, Nafion membranes were pretreated with 3 wt.% boiling H_2O_2 solution for 1 hour, boiling deionized water for 1 hour, and, followed by a boiling 1 mol/L H_2SO_4 solution for 30 min. After the treatment, the membrane was washed with deionized water several times and stored in deionized water before testing.

Morphology characterization The surface morphology and the thickness of the coating layer were studied by atomic force microscopy (AFM). AFM images were obtained using MultiMode 8 AFM (Veeco) with a NanoScope V controller (Veeco). Silicon tip and nitride coated silicon tip (Bruker) were used according to dry and wet samples respectively. All samples were treated at different plasma conditions to present morphology changes of the surface of the membranes. The scan assist mode was employed to scan the surface of the fully hydrated plasma-coated membrane, where the fluid cell was filled with deionized water. After the measurement, the hydrated samples were dried naturally in air for at least 30 min to present partially dehydrated membranes. The scan assist mode under atmospheric conditions with 30 % to 45 % RH was performed to investigate the surface of dehydrated membranes. Surface topological depths were estimated from AFM height images.

Ion transport property measurement. The measurement methods for vanadium ion permeability, proton conductivity, and IEC are the same as those for the methods mentioned in the previous section. The H^+ permeability was tested with diffusion method similar to the VO^{2+} permeability measurement. 1 M HCl solution was used as feed solution, and 1 M KCl solution was used as permeation solution. The change in the H^+ concentration in the permeate side was monitored using conductivity meter at 30 sec intervals. One

should note that, although diffusion is not considered as mechanism sole driving force for the protons transport in the VRFB, the ion diffusivity measurement can provide useful information on the ion transport properties of the membrane.

4.1.2 Result and discussion

Membrane morphology

Surface morphology of ionomer is very important because it forms ion channel and determines the state of the electrolyte in the polymer membrane[126]. As shown in **Figure. 15a**, thin hydrophobic coating layers are deposited successfully on top of BPSH60 by atmospheric plasma treatment. The thickness of the coating layer reported in our previous study was so thin that hydrophobic island was not formed in dehydration condition. Instead, in hydration condition, membrane surfaces exhibited a nano-crack surface morphology with the width of 2.5-7.5 nm and the depth of 3.3-14.1 nm. In the dehydrated conditions, the depths of nano-cracks were reduced to 1.1-9.1 nm (see **Table 7**). As the number of plasma treatments increased, the area and width of nano-cracks were also increased. The thickness of the coating layer also increased when the plasma coating cycles increased as evidenced by the increase in depth of nano-cracks which allowed forming nano-cracks during hydration and dehydration. For the sample with plasma treatment repeated 5 times (P-BPSH60 R5), the width of the nano-cracks was too narrow, and the size of the hydrophobic islands was too small to be detected by AFM images since the ultrathin hydrophobic coating layer did not form observable nano-cracks. However, the existence of nano-cracks was evidenced by improvement of the plasma treatment in proton permeability and selectivity over vanadium ion, as described in the following sections. Ion conductivity can be reduced when membranes are coated with even and thin hydrophobic barriers because it hinders proton transport. However, as illustrated in **Figure. 15b**, we coated thin hydrophobic layers with nano-cracks, which allowed protons to pass through nano-cracks on the hydrophobic coating layer without significant resistance to proton transports [12]. As summarized in **Table 7**, dimension and morphology of nano-cracks were reproducible and controllable in the deposited hydrophobic coating layer.

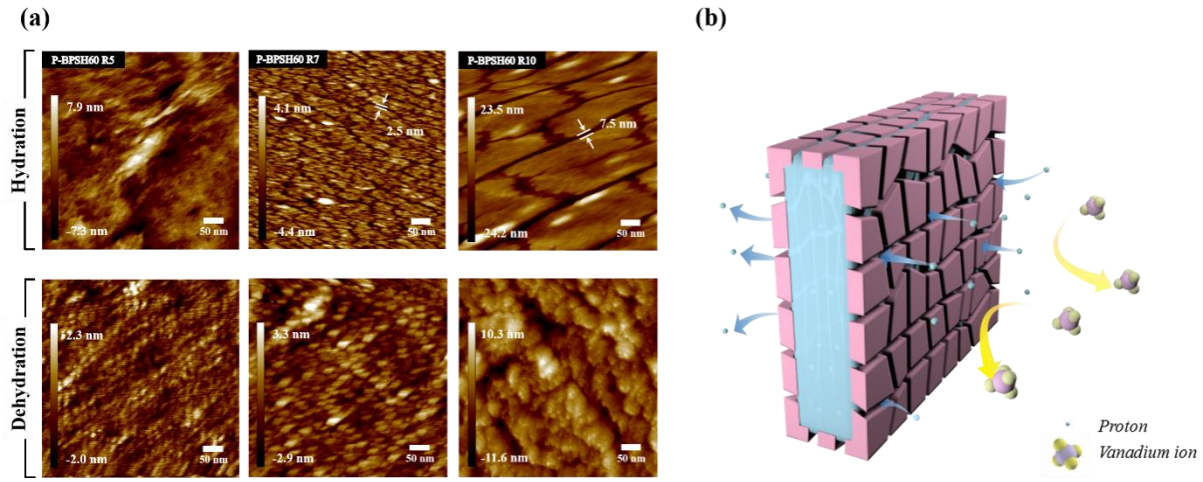

Figure 15 (a) AFM images of the P-BPSH60 membranes and **(b)** schematic of the ion selective mechanism by the nano-crack surface layer

Table 7. Roughness and height differences of the coated surface according to the number of plasma treatment.

Samples		Roughness			Depth of crack	Area of crack
		R_a (nm)[a]	R_z (nm)[b]	R_{max} (nm)[c]	(nm)	(%)
P-BPSH60 R5	Hydration	2.27	1.39	9.01	3.3	14.3
	Dehydration	0.38	0.84	2.01	1.1	N/A*
P-BPSH60 R7	Hydration	0.92	2.36	4.93	4.1	25.1
	Dehydration	0.61	1.28	2.92	2.2	N/A*
P-BPSH60 R10	Hydration	4.55	11.14	19.61	14.1	27.7
	Dehydration	2.96	3.36	11.00	9.1	N/A*

[a] Roughness average / [b] Average maximum height of the profile / [c] Maximum roughness depth

*Area of cracks in the dehydration condition are not available because of small crack width

Mechanical properties

Good mechanical properties are essential to prevent crossover of VO2+ ions due to physical failure. Data on tensile strength, elongation at break and Young's modulus are shown in Table 8. The pristine membrane showed tensile strength of 69.0 MPa, elongation at break of 12.4% and Young's modulus of 1.34 GPa. Similarly, plasma-coated membranes showed tensile strength of 66.8 – 75.6 MPa, elongation at break of 10.9 – 14.1% and Young's modulus of 1.23 – 1.37 GPa. Plasma treatment did not change the mechanical properties of the membrane because it formed a very thin coating layer on the surface. All BPSH60 membrane, with or without plasma coating, showed better tensile strength and Young's modulus than Nafion® 212 membrane. On the other hand, Nafion® 212 membrane was higher in elongation property.

Table 8. Mechanical stabilities of BPSH60, P-BPSH60 R5, P-BPSH60 R7, P-BPSH60 R10 and Nafion® 212 membranes.

Samples	Tensile strength (MPa)	Elongation at break (%)	Young's modulus (GPa)
Pristine	69.0 ± 2.1	12.4 ± 0.2	1.34 ± 0.06
P-BPSH60 R5	75.6 ± 4.2	14.1 ± 0.0	1.37 ± 0.04
P-BPSH60 R7	66.8 ± 8.6	10.9 ± 0.6	1.33 ± 0.19
P-BPSH60 R10	71.9 ± 6.5	14.0 ± 1.3	1.23 ± 0.13
Nafion® 212	20.6 ± 1.4	353.3 ± 2.1	0.15 ± 0.02

Ion exchange capacity (IEC)

The IEC_w values of membranes were summarized in **Table 9**. Pristine membrane exhibited an IEC_w value of 2.41, which is close to the theoretical value. There were slight changes in the IEC value after the plasma treatment, but there was no significant difference in all samples. This result indicates that the enhancement of proton selectivity and conductivity can be mainly due to the presence of the nano-cracks on the plasma coating.

Table 9. Ion exchange capacity (IECw) values according to the number of plasma treatments.

Samples	IECw (meqv g^{-1})
Pristine	2.41
P-BPSH60 R5	2.33
P-BPSH60 R7	2.25
P-BPSH60 R10	2.40

VO^{2+} and H^+ Permeability

The cross-over flux of vanadium ions through the membrane separators is detrimental to the VRFB operation, which can lead to high self-discharge of the battery and low coulombic efficiency (CE). Thus, a low permeability of vanadium ions through the membrane is one of critical properties for the membranes used for VRFB systems [127]. To investigate the enhanced ion selectivity by the nano-crack surface layer, we evaluated proton selectivity of the p-BPSH60 membranes with different numbers of coating cycles ranging from 5 to 10 (P-BPSH60-R5, P-BPSH60-R7 and P-BPSH60-R10). It can be seen from **Table 10** that the VO^{2+} permeability of the P-BPSH60 membranes (9.42×10^{-6} - 11.73×10^{-6} cm^2 min^{-1}) is much lower than that of the pristine BPSH60 membrane (2.17×10^{-5} cm^2 min^{-1}). The crossover of VO^{2+} could be restrained in the plasma-treated

surface layer, which creates narrower channels for ion transport on the membrane surface as presented in **Figure 15**. Despite the decreased of VO^{2+} permeability, it is also found that the H^+ permeability of the plasma coated membrane is as high as the H^+ permeability of the pristine BPSH60 membrane. The H^+/VO^{2+} permselectivity was calculated using proton conductivity over the vanadium ion permeability and was used to compare the properties of the membranes. As shown in **Table 10**, there is no distinct difference between the permeability or selectivity of the three P-BPSH60 membranes. In overall, the H^+/VO^{2+} permselectivity of the P-BPSH60 membrane is two times higher than that of the pristine BPSH60 membrane. It is also worth to note that the H^+/VO^{2+} permselectivity of the P-BPSH60 membrane is comparable to Nafion® 117, indicating that the P-BPSH60 membrane could be the cost-effective IEM in VRFB alternative to Nafion. Although the P-BPSH60 shows slightly lower selectivity than Nafion® membranes, these test results clearly show that the formation of nano-crack on the membrane surface can significantly enhance H^+/VO^{2+} permselectivity of the PEMs, and the enhancement in proton selectivity could provide higher efficiencies for the VRFB system (e.g. CE and EE).

Area resistance and proton conductivity

The area resistance of the membrane corresponds to the ohmic resistance of the battery, which determines the voltage efficiency (VE) of a VRFB. As summarized in **Table 10**, 60-μm-thick P-BPSH60 R5 membrane shows similar resistance with pristine BPSH60 membrane (thickness of 60 μm), implying the surface treatment doesn't affect the transport of protons. The area resistance of the P-BPSH60 R5 and R10 membranes is larger than that of pristine membrane because of their higher thickness[81]. While the pristine BPSH60 and P-BPSH60 R7 have similar resistance value with Nafion 212, the P-BPSH60 R5 and R10 membranes shows lower values compared to Nafion 117 with similar thickness. These effects of the area resistance on VRFB performance will be discussed further in the section of VRFB single performance test.

Table 10. VO^{2+} and H^+ permeability, proton conductivity and area resistance of BPSH60, P-BPSH60-R5, P-BPSH60-R7, P-BPSH60-R10, Nafion® 212 and Nafion® 117 membranes. α is the ratio of proton conductivity/VO^{2+} permeability.

Samples	Thickness (μm)	VO^{2+} Permeability (x 10^6 cm^2 min^{-1})	H^+ Permeability (x 10^4 cm^2 min^{-1})	Proton Conductivity ($mS.cm^{-1}$)	α (x 10^4 min.S cm^{-3})	H^+/VO^{2+} Permselectivity	Area resistance ($\Omega.cm^2$)
Pristine	60	21.7	7.15	121	0.56	32.95	0.21
P-BPSH60 R5	200	9.9	7.45	104	1.05	75.25	0.51
P-BPSH60 R7	60	9.4	6.99	104	1.10	74.36	0.26
P-BPSH60 R10	200	11.7	7.69	108	0.92	65.73	0.61
Nafion® 212	55	4.1	3.89	74	1.78	94.88	0.21
Nafion® 117	195	3.2	2.66	59	1.84	82.87	0.98

A higher proton conductivity implies that the faster proton transport rate through the membrane and less voltage drop, which results in a higher VE along with lower area resistance. The proton conductivity of the P-BPSH60 membrane is only slightly lower than that of the value of the pristine BPSH60 membrane. Since

the vanadium ion permeability was dramatically decreased, all P-BPSH60 membranes show much higher selectivity values than the pristine BPSH60 membrane, which is consistent with the results presented in **Table 10**. Like the result of the H^+ permeability, we couldn't find a clear correlation between the coating cycle numbers and the ion conductivity for the plasma-coated membranes. Therefore, in the rest part of the paper, the plasma-coated membranes are simply denoted as P-BPSH60.

VRFB single cell performance

Charge-discharge curves Charge-discharge curves of VFRB with Nafion® 212, pristine BPSH60 and P-BPSH60 are displayed in **Figure 16**. The charge-discharge capacity (Ah) of VRFB with the P-BPSH60 is larger than that of VRFB with BPSH60 and Nafion®. This may be due to the suppressed vanadium cross-over by the surface nano-crack selective layer, which reduced the discharge capacity loss. It was also found that the charging curve of VRFB with the P-BPSH60 is slightly above that of VRFB with pristine BPSH60, indicating a higher charging overpotential. This could be due to the slightly higher membrane resistance (slightly lower proton conductivity) of the P-BPSH60 membrane, as described in the proton permeability/conductivity test (**Table 10**).

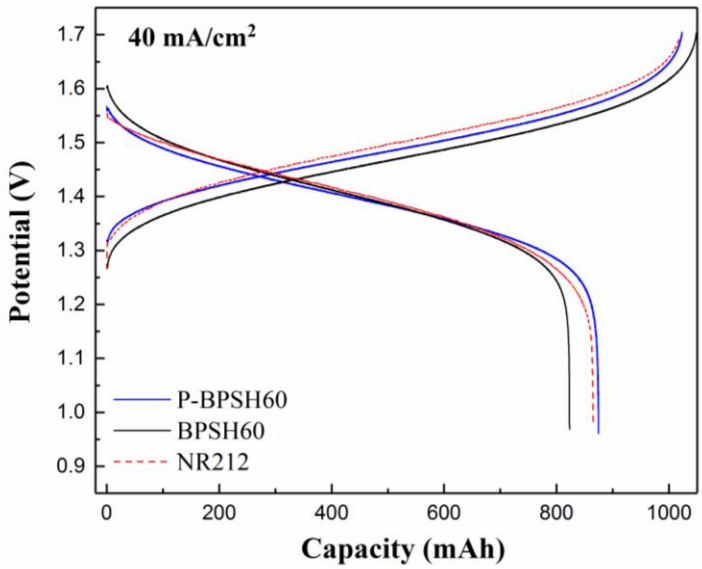

Figure 16. Charge-discharge curve of VRFBs with different membranes at the current density of 40 mA/cm^2.

Effect of surface coating As shown in **Table 11,** the efficiencies of the VRFB assembled with P-BPSH60 (60-μm in thickness) compared with that of the batteries with BPSH60 and Nafion® 212 at the current density of 40 mA/cm^2. Each performance value is averaged from the first 10 cycle charge/discharge tests. It can be seen that the formation of nano-crack selective layer remarkably improved the performance of the VRFB with pristine BPSH60. The CE value of the P-BPSH60 membrane achieved 86.88 %, which is higher

than the CE value (79.27 %) of the VRFB with the pristine BPSH60 membrane. This improvement is possibly attributed to the attenuated vanadium ion crossover flux by the surface nano-crack selective layer. Although the VE value of the P-BPSH60 membrane showed slightly lower VE value than that of the BPSH60-based VRFB cell, its EE value increased from 73.58 % to 80.08 %. The result indicates that the employment of the surface nano-crack selective layer on the IEM can effectively improve the overall performance of the VRFB. The result also shows that the VRFB equipped with this plasma coated membrane exhibit similar performance with the VRFB using Nafion® 212 membrane. The energy efficiency (EE) of VRFB with Nafion® 212 is 79.96%, which is similar to that of the VRFB with P-BPSH60 membrane at the same current density.

Table 11. CE, VE and EE of VRFB single cell with: (a) Pristine BPSH60; (b) P-BPSH60 (60 μm); (c) Nafion® 212; (d) P-BPSH60 (200 μm); and (e) Nafion® 117 at current density of 40 mA/cm^2.

Samples	Thickness (μm)	Columbic Efficiency (%)	Voltage Efficiency (%)	Energy Efficiency (%)
Pristine	60	79.27	92.82	73.58
P-BPSH60	60	86.88	92.16	80.08
Nafion® 212	55	85.41	93.68	79.96
P-BPSH60	200	92.78	92.01	85.37
Nafion 117	200	95.35	89.27	85.11

Effect of current density The single cell performance with the pristine BPSH60, Nafion 212, and P-BPSH60 in terms of CE, VE, and EE were evaluated at current density ranging from 10 mA/cm^2 to 100 mA/cm^2, as shown in **Figure 17**. Due to the higher IR drop and electrochemical reaction resistance at higher current density, the VE values decrease as increase in current density. On the other hand, because of the cross-mixing of the vanadium ion between the two half-cells, the decrease in the testing time at higher current density leads to an increased CE. The maximum EE of the single cell with the P-BPSH60 membrane (~80%) was achieved at a relatively low current density of 40 mA/cm^2.

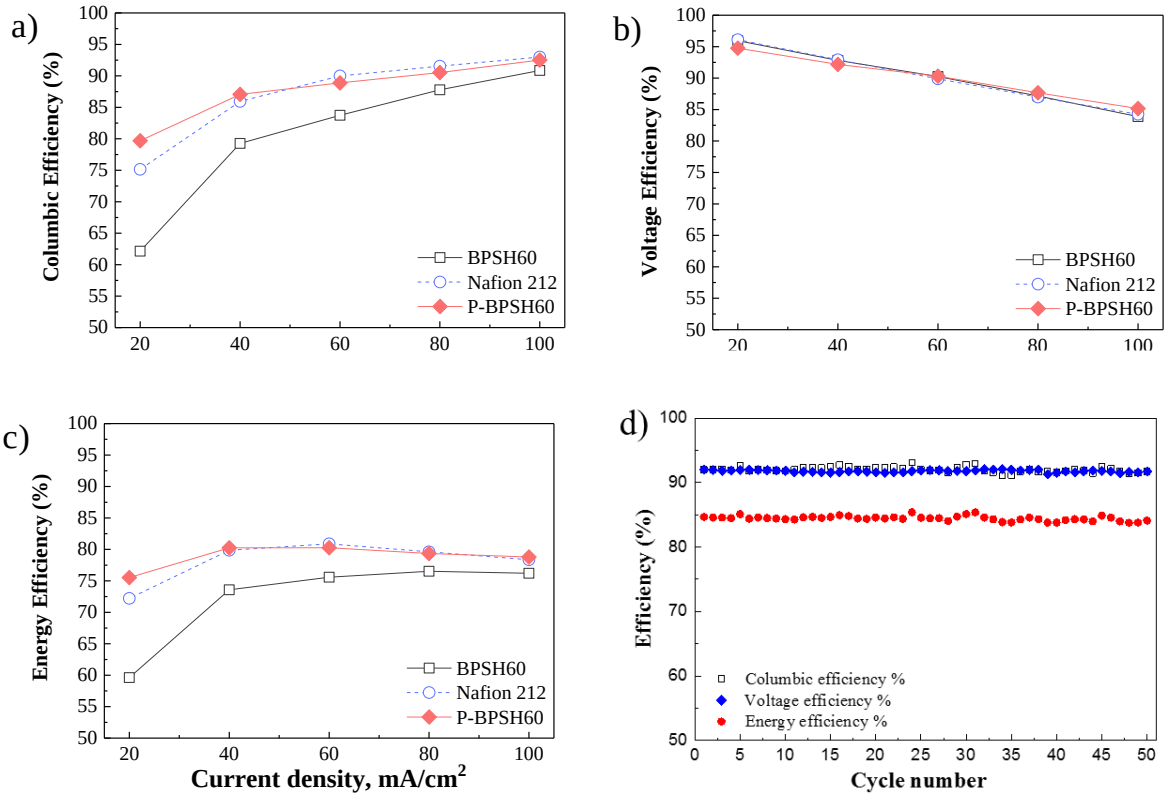

Figure 17. (a) CE, (b) VE and (c) EE of VRFB single cell with the BPSH60, Nafion 212, and P-BPSH60 membrane at different current densities. (d) Efficiencies as a function of 50 charge/discharge cycles for VRFB single cell with P-BPSH60 membrane at current density of 40 mA/cm^2.

The VRFB with the P-BPSH60 membrane shows a very similar performance with the one using Nafion membrane. As compared to the pristine BPSH60 membrane, the CE and EE of the P-BPSH60 is improved over the entire current range in this test. The improvement can also be attributed to the lower vanadium crossover rate of the plasma coated membrane. It is noticeable that the P-BPSH60 membrane shows almost identical VE as the pristine BPSH60 membrane, which is consistent with the area resistance value for these membranes as discussed in the previous section. This result indicates that the plasma coated layer can effectively alleviate the vanadium ion crossover without sacrificing the ability to transport protons and thus can overcome trade-off issue of typical IEMs.

Effect of membrane thickness Since the performance of the VRFB at a certain current density is affected by the thickness of the IEMs, we also evaluated a thicker plasma-coated membrane with similar thickness (190 μm) to Nafion 117, which commonly exhibits better performance than Nafion® 212 in VRFB at lower current densities. As shown in **Table 11**, the VRFB with 190-μm-thick P-BPHS60 shows an almost 6 % enhancement in the CE value than that of the battery using 60-μm P-BPHS60, while just slightly

compensating the VE. The EE of the VRFB with 190-μm P-BPSH60 membrane reaches 85.37 %, which is slightly higher than that of Nafion® 117 (85.11 %). In general, the results shown in **Figure 17** and **Table 11** demonstrate that P-BPSH60 membranes can achieve comparable performance in VRFB as Nafion® membranes with corresponding thickness. Notably, the hydrophobic plasma-coating technique can be conveniently scaled up and the price for BPSH60 is considerably lower than Nafion®, the P-BPSH60 could be more attractive for commercial use.

Cycle stability To further investigate the operation stability of P-BPSH60 membrane under the harsh testing condition for VRFB application, 50 cycles of charge-discharge tests were performed on the static VRFB single-cell assembled with the P-BPSH60 membrane at the current density of 40 mA/cm^2 (**Figure 17d**). It can be seen that cell efficiencies of the cell remained nearly constant and highly stable during 50 charge-discharge cycles. The CE and VE retained above 92%, indicating the lower permeation rate of vanadium ions and suggesting the membrane was high conductive even at the end of the stability test. It can be concluded that the P-BPSH60 membrane possesses very remarkable chemical stability under the strong oxidizing and acidic environment.

4.1.3 Summary

Ion exchange membranes with surface nano-crack selective layer, P-BPSH60s, were successfully developed for VRFB. The effect of these patterned nano-cracks on the ion transport and VRFB performance was investigated. Our works demonstrate that the nano-crack selective layer on the membrane surface is effective in hindering the transport of vanadium ions and therefore mitigating the cross-over flow, while it has less effect on proton conductivity resulting in enhanced ion selectivity. The VRFB with P-BPSH60 membrane showed a significantly improved columbic efficiency and energy efficiency compared to the VRFB with pristine BPSH60 membrane. Furthermore, the VRFBs with the P-BPSH60 membrane showed performance similar to the VRFB with costly Nafion® membranes. Consequently, the plasma coated BPSH60 membranes were successfully demonstrated as an inexpensive and high-performance candidate for VRFBs. Our results strongly suggest that the plasma-induced surface modification of the IEM can serve as an effective nano-engineering technique to overcome the limitations of the trade-off relationship between high vanadium ion diffusivity and high proton conductivity that is typical of conventional polymeric PEM. It is expected that such effective and scalable technique can be employed for other polymer substrates as well to enhance their performance.

4.2 Regulating ion transport using a 2D-graphene coated hybrid IEM

With our previous efforts and results from the surface patterned IEMs, we are aiming at building a more advanced membrane system based on the concept of 2D-layer coated hybrid IEM. To achieve this goal, a surface layer with ultra-high ion selectivity and low ionic resistivity is desired for constructing the hybrid membrane. Recent studies on one-atom-thick graphene and hexagonal boron nitride (hBN) have revealed the great potential of using 2D films to develop hybrid proton exchange membranes (PEMs) because of their high proton conductivity, chemical and thermal stability, and impermeability to other gases, ions, and water molecules [128]. The monolayer of graphene only allows subatomic ions (e.g., protons) to pass through the tiny 'holes' of electron-density distribution in their lattice electron clouds, which could impart enormous proton selectivity to an electrochemical system because of their intrinsic impermeability to other redox couple electrolyte ions such as vanadium ions. Despite the great promise, the practical deployment of the two-dimensional (2D) inorganic membrane in the electrochemical devices have been rarely reported. This slow research progress is mainly due to a lack of proper membranes design and an inadequate understanding on the ion transport mechanisms in 2D-layer covered hybrid membranes.

Herein, we have proposed several approaches in this study to investigate the fundamental ion transport properties of the 2D films and the 2D-layer coated IEMs. First, we studied ion transport properties across the bare graphene. To minimize the effect of defects on the 2D layers, the 2D film should be transferred on an inorganic silicon nitrate (SiNx) membrane which is dimensionally stable and only has a single aperture with small active area to transport ions (**Figure 18**). Proton conductivity, membrane area specific resistances, and membrane cross-over of various redox couples (e.g. $V^{4+}/^{5+}$) will be measured using electrochemical impedance spectroscopy (EIS) analysis. Upon successful completion of the basic transport studies through 2D single layers, the effect of chemical doping on the 2D films will be investigated. The p- and n-type dopant layer (e.g. polyaniline) was doped on the 2D film or the adjacent polymers. The ion transport properties of these membranes were studied with diffusion and impedance methods.

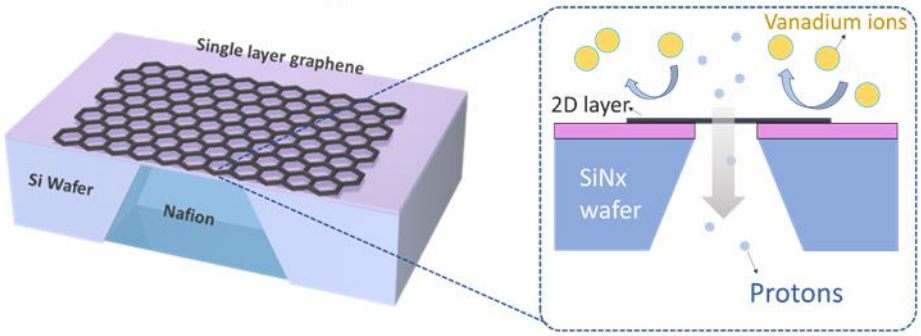

Figure 18. (a) Schematic of proton transport through 2D film transferred on an inorganic silicon nitrate (SiN_x) substrate.

In the second stage of the study, we have fabricated the hybrid membrane by transferring graphene on a polymer support. To prevent breakage of the monolayered 2D film on ion selective membrane, which can be swelled in aqueous electrolyte during the test, a dimensionally stable ion conducting membranes substrate were prepared using the pore-filling method. Upon successful fabrication of defect-free 2D hybrid membranes, their electrochemical performances (e.g. proton selectivity/conductivity, area resistance) and redox flow batteries performance were evaluated. In order to further control the selective ion transport through the 2D-film, we have planned to introduce our hybrid membranes with p- or n-type dopant. These dopants are expected to affect the surface charge density and electron clouds of 2D layers, thus, affecting the active energy as protons penetrate through the 'holes'. As part of our future work, the doping-induced proton transports, and electrochemical performance evaluation of doped hybrid membranes will be studied.

4.2.1 Experimental methods

Fabrication of SiN_x device*:* A schematic of graphene on single hole silicon nitrate (SiN_x) device is shown in **Figure 19** The SiN_x device was fabricated using the following procedure: A Si wafer was first cleaned by immersing in the HF solution (50 wt%) for 2 minutes and then cleaned with DI water. Then, it was put inside a PECVD chamber, and a 1.5-micrometer thickness of silicon nitride was deposited on both sides of the surface. The silicon nitride acts as a passivation layer. After the deposition of silicon nitride, the wafer was cleaned again and then patterned using photolithography followed by etching step to etch silicon using reactive ion etching. Then, the wafer was immersed in the 45% KOH solution at 80 ^{o}C. with an effective silicon etch rate of 55 microns/hour. The wafer was further coated with a 100-nm-thick chromium layer to improve the selectivity during the reactive ion etching step. The freestanding silicon nitride layer with chromium is then spin-coated with a PMMA photoresist and patterned with a hole using EBL. In the last step, the chromium from the patterned spot is removed using a wet chemical etching technique (Microtech Cr etchant) and the hole is drilled using reactive ion etching (CF_4 and O_2 mixture).

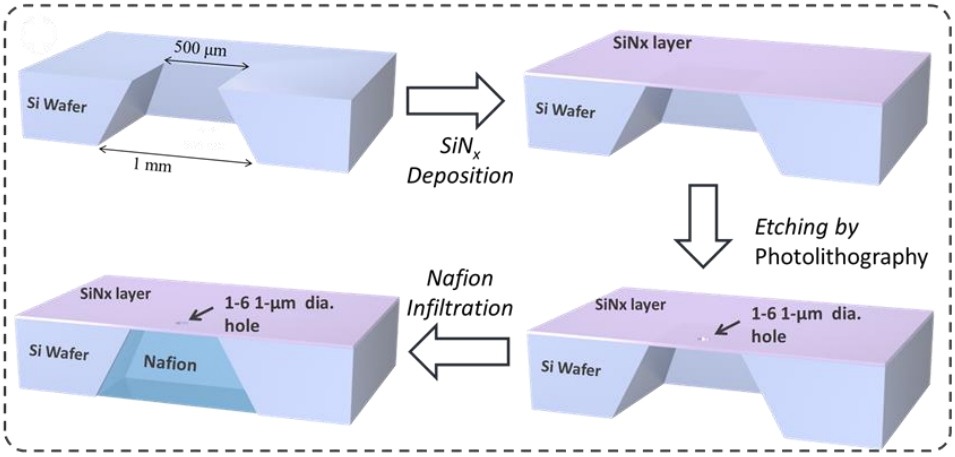

Figure 19. Schematic fabrication procedure of silicon nitrate (SiN_x) device.

Graphene transfer Single layer and multi-layer graphene were transfer to the SiN_x and polymer support using a PMMA assisted method. First, graphene grown on copper substrate was coated with PMMA by spin coating using a 2.5 wt% PMMA/anisole solution. The spin coating rate is set to increase from 500 rpm to 4000 rpm in 60 s and subsequently ramp down to 1000 rpm. Afterward, graphene-coated with PMMA was annealed in 130 ºC oven for 1 min and then gently floated on the 0.5 M FeCl3 solution overnight in order to etch out the copper substrate. The remaining impurities are removed by replacing FeCl solution with HCl and ammonia solution and subsequently washed with DI until no yellow color was observed. The graphene will be transferred on the targeting substrate and air-dried for one day. A 15 min annealing process was performed at 130 ºC to enhance the interaction between graphene and substrates. Finally, the PMMA layer was removed by immersing in acetone solution.

Synthesis of polyaniline and doping The polyaniline (PANI) emeraldine base (EB) was synthesized via in-situ chemical oxidation polymerization of aniline monomer (1M) in aqueous HCl (1M) for 2 hrs and mixed with oxidant (NH4)2S2O8 (0.1M) at 5◦C for 1 hr. After filtration, the residue particle dissolved in ammonium hydroxide solution (1M) that leads to the transformation of emeraldine salt (ES) form of PANI into the EB form of PANI. The EB form of PANI in a dimethyl sulfoxide (DMSO) was doped by dodecylbenzenesulfonic acid (DBSA) as P-type dopant and sodium hydride (NaH) as N-type dopant.

Fabrication of Nafion infiltrated PETE and PTFE membrane substrates:

Figure 20 demonstrates the illustration of the Nafion infilled PETE and PTFE membranes. The solution used for the infiltration consists of 10% Nafion in IPA. To prepare the solution, 2 g Nafion 117 was cut into smaller pieces and pretreat using standard procedure. 2g Nafion 117, 7.6 g DI water, and 30.4 g IPA were

mixed in an autoclave and subsequently loaded into 200 ºC oven overnight (8-10 hour). The obtained well-mixed solution will be cooled down and air-dried for 1day to obtain the Nafion resin. The Nafion resin was dissolved in 20 mL IPA and stirred for 1 day to obtain the 10wt% solution.

Before the infiltrating Nafion into the substrate, the PETE membrane was prewetted with IPA to improve the membrane wettability. The prewetted PETE membrane will be immersed in a 10wt% Nafion solution in IPA and sonicate for 1 hour to remove the air bubbles inside PETE pores. After taking out the PETE membrane from the solution, the excess Nafion solution on the PETE surface was removed using spin coater at low RPM. Nafion solution infilled PETE was loaded in a vacuum oven at room temperature for 1-2 hours to push Nafion into the pores of PETE membrane. Single-layer graphene will be transferred to the n-PETE membranes using a PMMA assisted transferred method as mentioned above. Before removing PMMA, the membrane will be annealed at 110 ºC for 5 min to improve the contact between graphene and substrate. The PMMA layer will be dissolved with acetone for 1 day.

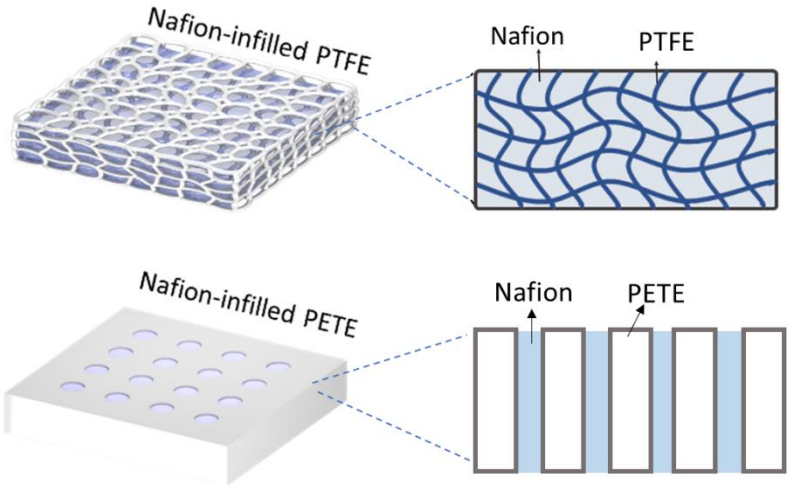

Figure 20. Schematic illustration of Nafion infilled PTFE and PETE membrane.

Morphology measurement

The morphology of SiNx device and hybrid membrane was characterized by field emission scanning electron microscope (FESEM, Hitachi S4800) and atomic force microscope (TT-2 AFM, AFM workshop) using contacting mode.

Ion transport property evaluation and VRFB single cell test

The protocols for vanadium and proton diffusion test in this study are similar to those used for testing pure polymer membranes (Chapter 3) and plasma coated membranes (Chapter 4, section 4.1). Due to the smaller

active area of the SiN_x device and hybrid membrane, the diffusion rate becomes slower. Thus, the duration of the diffusion test is longer than the previous works. Single-cell performance of the graphene transferred membranes are tested using a 1x1 cm^2 cell due to the limited graphene transfer area. Since the open area of PETE membrane is only ~10% of its footprint area, the applied current was also scaled down to 1/10. Other testing parameters are the same as previous works.

4.2.2. Graphene transferred on SiN_x device

Fabrication of SiN_x device and graphene transfer

To reduce the risk of ions transporting through the cracks and pinholes on the 2D-layer, a SiN_x membrane with a single micrometer-sized hole was fabricated and will be used as the support for transferring 2D film. The structure of the SiN_x device was examined by combinedly using an optical profilometer (**Figure 21 a&b**) and SEM (**Figure 21 c-f**). The existence of a single micrometer-sized aperture was evidenced from the sharp decrease of highness detected by the optical profilometer (right panel of **Figure 21b**). However, due to the small pore size and long-distance, the laser from the profilometer couldn't travel through the aperture. Thus, we scanned the backside of this device with the SEM, which has higher resolution and stronger laser power. From the SEM images, we can see the aperture with a diameter of ~1 um on the backside of the device. These results demonstrated that the device has been successfully fabricated.

Graphene was transferred on the SiN_x device after its structure was confirmed, To protect the graphene from collapsing during the test, the bottom side of the device was filled with Nafion, which functions as mechanical support as well as ion-conducting media. The quality of the transferred graphene was examined by optical microscopy and Raman spectrum. As shown in lower resolution optical microscopic images (**Figure 22a)**, the transferred graphene is absent of big cracks or pinholes. Although a few cracks and small defects can be found on the high-resolution images, their effects on the transport measurement could be negligible, considering the small diameter (1 μm) of the aperture on the SiN_x device. Raman spectroscopy measurement was also performed on the graphene/SiN_x membrane (**Figure 22b**). Five different spots on the membrane were examined. All the locations exhibit strong 2D and G peak at ~1580 and 2700 cm^{-1}, respectively, while only 3 and 5 spots show very weak D peak at Raman shift ~1350 cm^{-1}. These optical microscopy images and Raman spectrum verified the successful transfer of graphene onto the SiN_x device with high integrity.

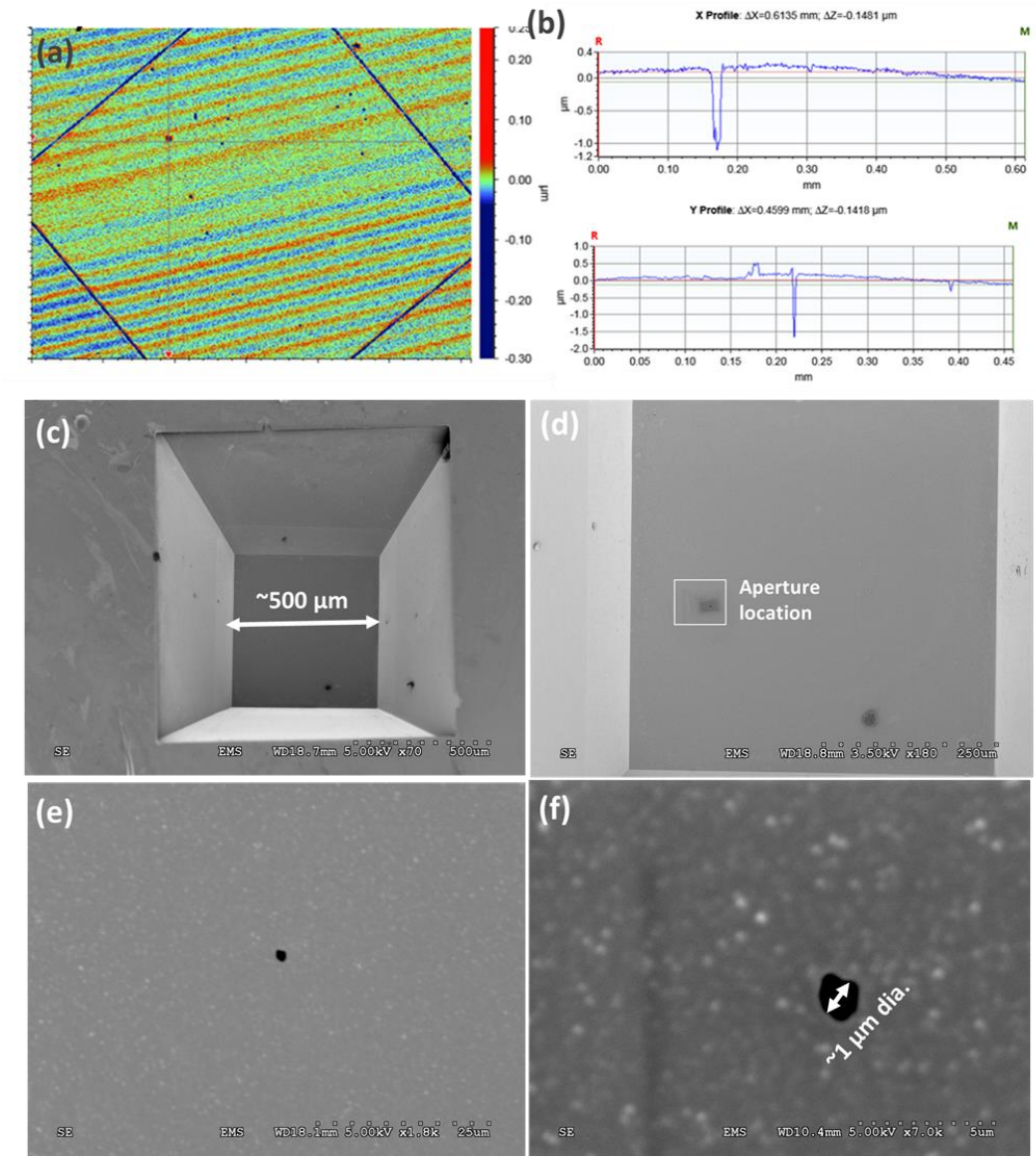

Figure 21. (a) & (b) Confirming the pore size using optical profilometer, (c-f) SEM images of the lower surface of SiN_x device with different resolution.

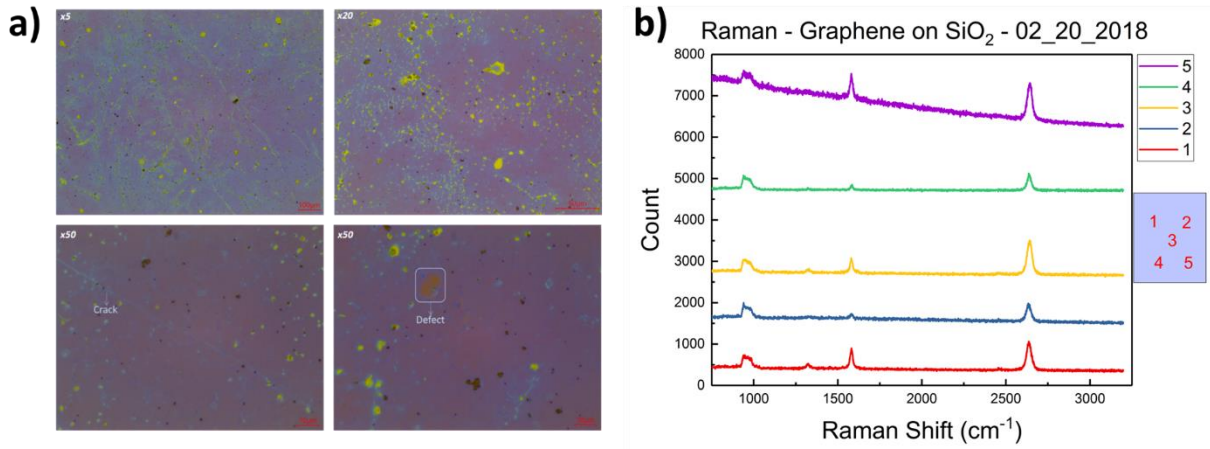

Figure 22. (a) Optical microscope images for the graphene/SiN_x membrane. (b) Raman spectrum for the graphene/SiN_x membrane.

Ion transport through supported single-layer graphene and the interaction with Nafion

The ion transport of the graphene/SiN_x membrane was investigated via H^+ and VO^{2+} permeation test as well as electrochemical impedance spectroscopy (EIS). A side-by-side diffusion cell (**Figure 23a**) was used for the diffusion test. For H^+ permeation test, 1mol/L HCl solution was used as a feed solution, and 1 mol/L KCl solution was used as a permeation solution. The change in the H^+ concentration in the permeate side was monitored using conductivity meter at a certain interval. It was found that the proton permeation through the graphene transferred SiN_x membrane is considerably slower than the original SiN_x membrane (**Figure 23b**). For the diffusion test with SiN_x substrate without graphene, the H^+ concentration increase almost linearly with time, showing a fast effusive flux of H^+ through the micro-size hole. In contrast, the Nafion infilled SiN_x membrane and the graphene transferred Nafion/SiN_x membrane shows that the H^+ concentration in the permeate solution increases slowly for the first 1-2 hours measurement and finally reaches a plateau. The results imply that the transport resistance of the Nafion/SiN_x and the graphene/Nafion/SiNx membrane is much larger than that of the pristine SiN_x membrane. However, from the result, it is difficult to differentiate the contribution of Nafion and Graphene, because both curves show a similar trend. The results are understandable, if considering the overall slow diffusion rate of protons through the single aperture with a diameter of 1 μm. The slight increase in the proton concentration at the beginning of the test is likely due to the release of the adsorbed ions on the diffusion cell. Thus, to clearly see the effect of graphene on ion transport, it is necessary to increase the ion transport rate to a measurable speed, either by enlarging the open area or applying a higher driving force (concentration gradient or electrical field).

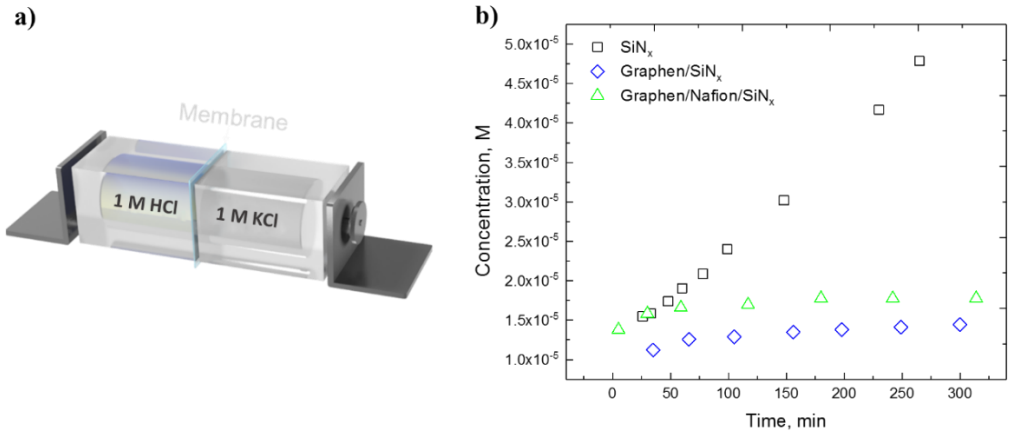

Figure 23. (a) Schematic of diffusion cell for proton diffusion measurement, (b) H^+ concentration in the permeation solution vs. time for the diffusion cell with Graphene/SiN_x membranes.

The procedure for the vanadium ion diffusion test is similar to the proton test. However, the result is even more disappointing. Due to the slower diffusion of VO^{2+} ion compared with proton and the detecting limit of small amount vanadium using UV, it is even difficult to detect the diffusion of VO^{2+} ions through the pristine SiN_x membranes (These results are not shown here because none of them showing signal for vanadium permeation).

Lastly, the ion-conducting through the three membranes are measured with impedance methods, where the electrical field exists. The impedance of the SiN_x membranes with/without graphene transferred was measured using EIS. The frequency was swept from $1x10^6$ Hz to 1 Hz at 10 mV amplitude vs. OCP. The resistance of the system was obtained from the intercept of the Nyquist curve on the x-axis (real part of impedance) at high frequency (inserted figure on **Figure 24**). It was found that the infilling of Nafion increase the system resistance with SiN_x membrane from ~20 Ω to ~28 Ω. While the incorporation of graphene further increases the system resistance to ~47 Ω. The experiment result indicates that the presence of graphene and Nafion increased the resistance. However, the results are not adequate to justify if the proton transfer through the graphene lattice or through the defects.

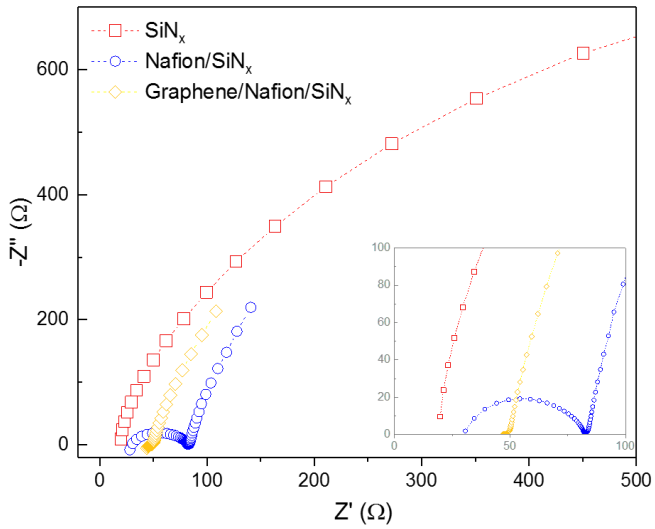

Figure 24. Nyquist curves for the conductivity cell loaded with SiN_x membranes

Effect of doping.

To investigate the doping effect of graphene charge density, three pieces of graphene were transferred to p-doped, n-doped, and non-doped (EB form) of polyaniline layer made by spin coating different PANI/NMP solution on the silicon substrate. The charge density was investigated using Raman spectroscopy.

From each graphene transferred sample, we picked the Raman spectrum of 9 different spots, as shown in **Figure 25-27** (details on the mapping could be found in the Appendix). From these results, we could see

the graphene signal in some of the spectrum. However, we couldn't completely differentiate the graphene peak from the background signals of polyaniline. This is because the polyaniline is also known as highly conductive material and its thickness is much thicker than the graphene. As a consequence, the Raman signal from the graphene is strongly interfered by the background signals from the PANI layers underneath the graphene. Thus, Raman may not be a suitable tool for investigating our system.

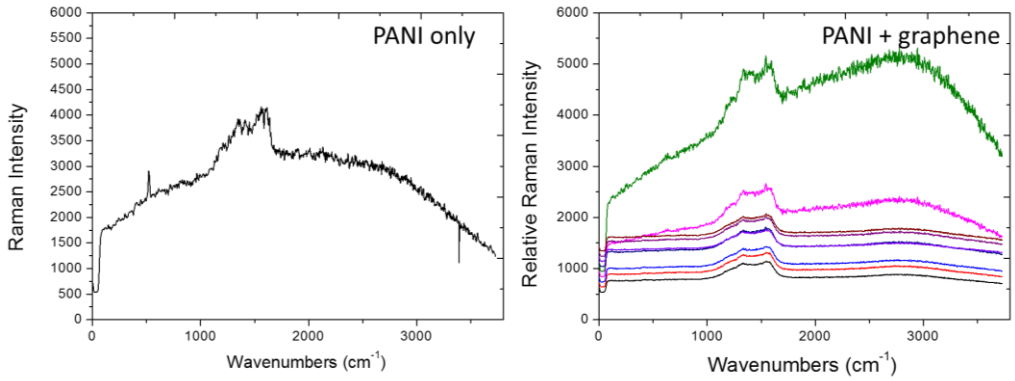

Figure 25. Raman mapping of the graphene transferred non-doped PANI.

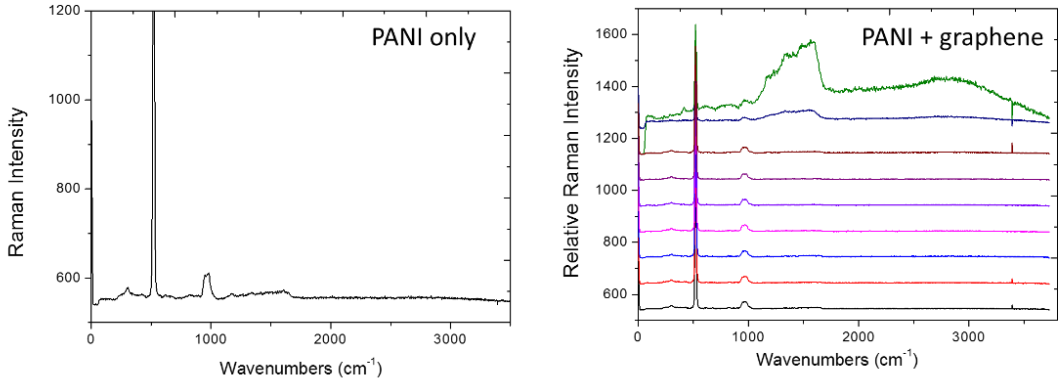

Figure 26. Raman mapping of the graphene transferred p-doped PANI.

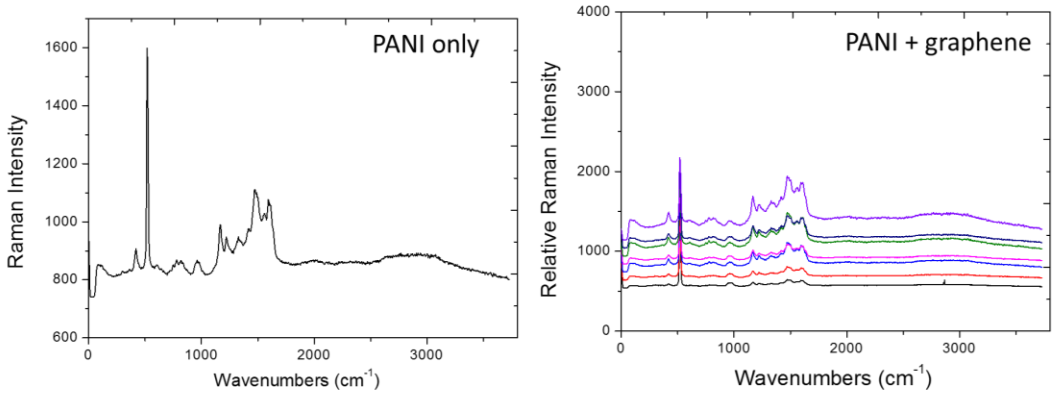

Figure 27. Raman mapping of the graphene transferred n-doped PANI.

4.2.3 Graphene transferred on dimensionally stable pore-filled IEM

The previous studies on the single aperture SiN_x device provides useful information on the ion transport through graphene. However, for practical application, it is imperative to transfer graphene on a substrate with sufficient large surface area. Meanwhile, the substrates ought to provide adequate conductivity and be dimensionally stable. Thus, choosing a suitable membrane matrix is a critical step for achieving our final target of developing a highly ion selective hybrid membrane. Cation exchange membrane, such as Nafion, seems to be a feasible option for substrates, due to their high proton conductivity and proper chemical stability. Nonetheless, most of these membranes exhibit a high swelling ratio in aqueous solution, which would inevitably lead to the formation of cracks or pinholes on the transferred 2D films. To restrain the intrinsic swelling behavior of IEMs, a practicable strategy, as introduced in Chapter 2, is to infill the polymers into a robust porous matrix (so-called pore-filled membrane). Here we choose two commercially available membranes, porous polytetrafluoroethylene (PTFE) membrane and polyester track-etch (PETE) membrane, as substrates. The origin for choosing these two membranes is attributed to their high chemical stability in the strong acid VRFB operation condition environment. Same as the previous study, Nafion was used as the ion-conducting media and was infilled into these substrates. The resulted membranes are correspondingly referred to as n-PTFE and n-PETE membranes.

Nafion infilled PTFE substrates

The n-PTFE membrane was fabricated by infilling the Nafion/IPA solution into the PTFE substrate under vacuum. After infiltration, the color of the membrane turned from white to transparent (**Figure 28a**), indicating Nafion has been successfully infilled into the PTFE matrix, thus altering the light refraction. The

morphology of the n-PTFE membrane was further examined by SEM. As shown in **Figure 28c**, Nafion has been well infiltrated throughout the entire volume of the PTFE substrate with a ~3-4 μm excess Nafion layer remaining on the top side. From **Figure 28 d**, we can still observe a certain area on the bottom side of membrane (**Figure 28d**) not fully infilled with Nafion. Whereas, the volume of these non-infilled part is almost negligible compared to that of the entire membrane.

The swelling ratio of the membrane was examined by comparing the length and area of the membrane in the hydration and dehydration state. As shown in **Figure 28b.** the pore-filled Nafion/PTFE membrane shows a reduced swelling ratio (5% in length) compared to the pristine Nafion membrane (14% in length), which demonstrates the effectiveness of using the pore-filled method for reducing the swelling ratio of IEMs. However, the 5% swelling is still questionable for preventing the graphene to be torn after transferring.

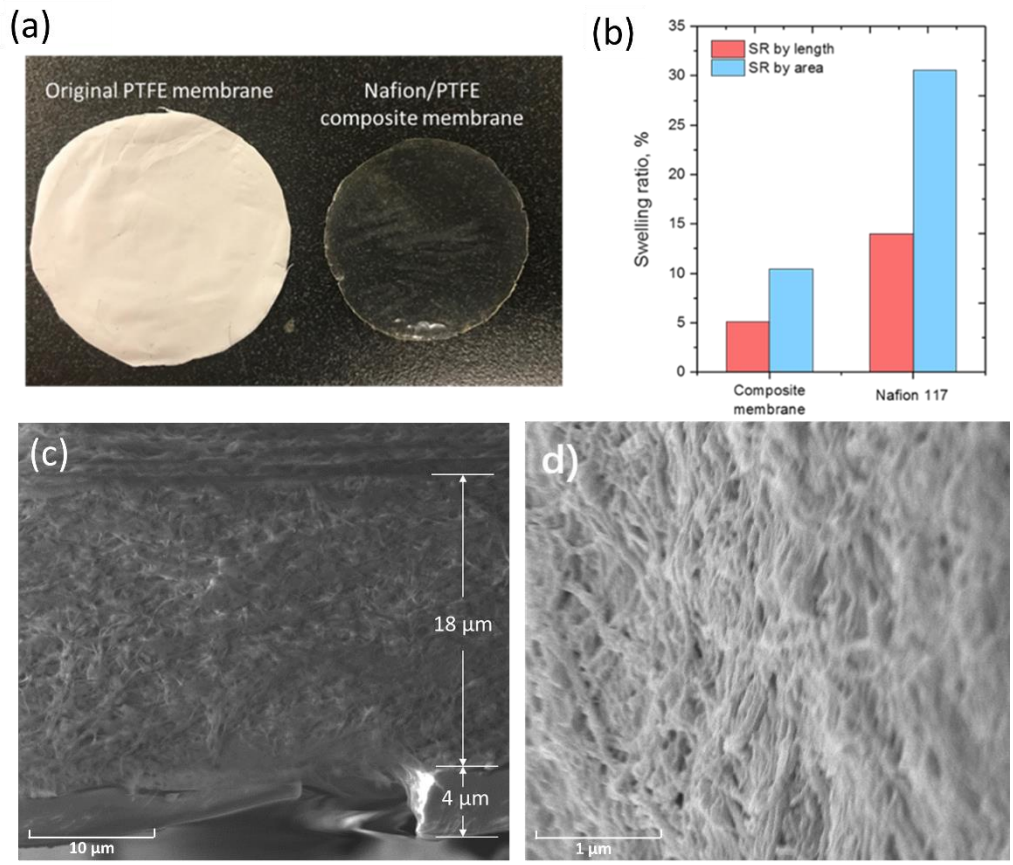

Figure 28. (a) Digital photo of the PTFE membrane before and after infiltration of Nafion. (b) Comparison of swelling ratio of composite membrane and pristine Nafion 117. (c) & (d)SEM images for the n-PTFE composite membrane.

The ion transport of the pore filled membrane was examined by testing vanadium permeability and proton conductivity. As shown in **Figure 29**, the pore-filled n-PTFE membrane shows much lower vanadium

permeability compared to the pristine Nafion 117 and 212 membrane, which is comprehensible if considering the less transport area of n-PTFE membrane taken by the porous substrates. However, it was found that the proton conductivity of the n-PETE membrane is also significantly reduced and leads to a worse ion selectivity than the pristine Nafion membranes. This result is unexpected, and the possible reason could be attributed to the tortuous pore geometry in the PTFE membrane that impedes the proton transport. Thus, although the n-PETE is successfully fabricated and shows reduced the swelling ratio compared to the pristine Nafion. Considering the less ion selectivity and rest 5% swelling ratio, it is not qualified as a substrate for directly transferring graphene.

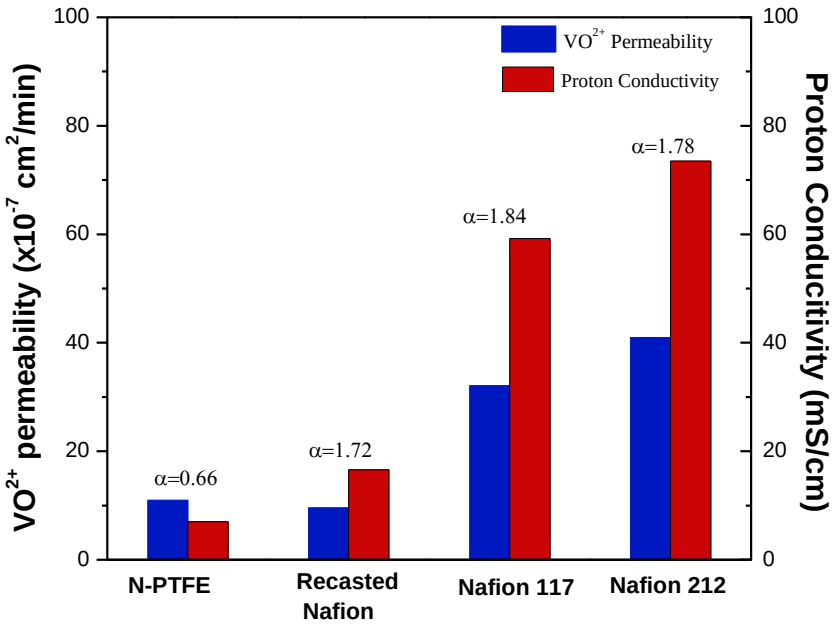

Figure 29. Ion selectivity of the n-PETE membrane compared to the recast Nafion, Nafion 117 and Nafion 212 membranes.

Nafion infilled PETE substrates

We further fabricate the Nafion infilled track-etch polyester (PETE) membrane, in hoping to use it as the substrate for graphene transfer. The major structural difference between the track etch membrane and another porous membrane is that track-etch membrane usually has straight cylindrical channels that penetrate through the membrane (as shown in **Figure 30**). This is an adventurous feature as a substrate for transferring graphene, since the defect on the graphene would only affect the ion transport through the

channel underneath (**Figure 30**). Thus, the effect of defects on the graphene on the overall membrane performance would be minimized.

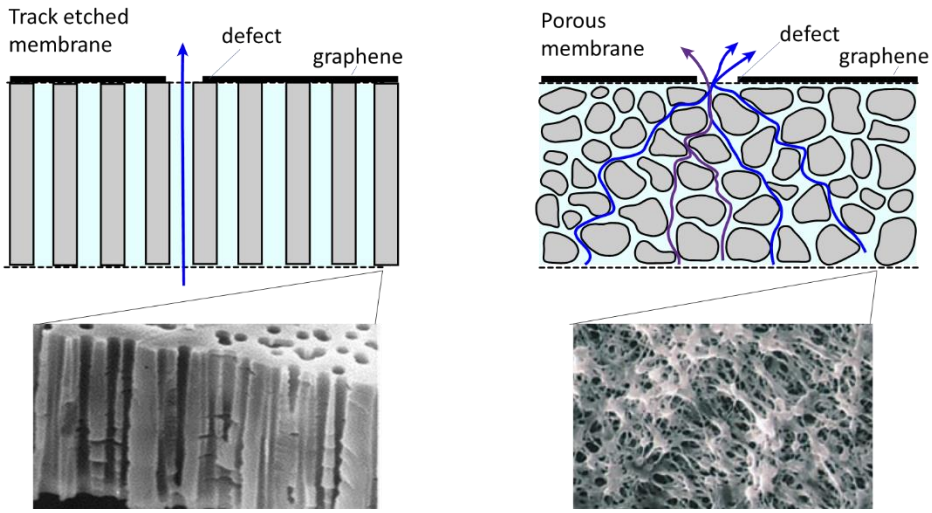

Figure 30. Proposed ion transport through the defects of graphene on the PETE and porous substrates (SEM images are obtained from Sterlitech website)

After Nafion infiltration, the swelling ratio, proton conductivity, and vanadium diffusivity of the n-PETE membrane was measured and compared with those of the n-PTFE and pristine Nafion membranes. It was found that the n-PETE has very high dimensional stability in water and the swelling ratio is <1% (**Figure 31**). Moreover, the ion selectivity of the n-PETE membrane is close to that of Nafion membranes. Therefore, the n-PETE membrane could be a proper substrate for the graphene transfer.

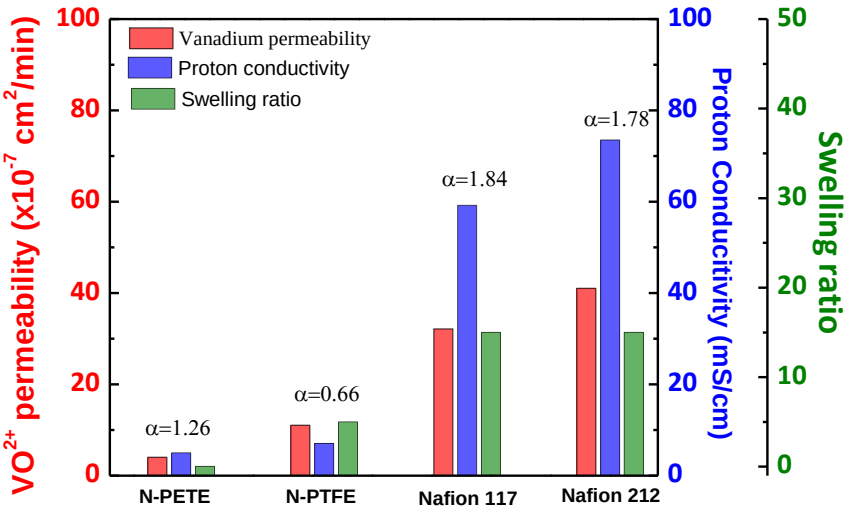

Figure 31. Vanadium permeability, proton conductivity, and swelling ratio of N-PETE, N-PTFE, Nafion 117 and Nafion 212.

Graphene transferred n-PETE substrates

Since the n-PETE membrane exhibits excellent dimensional stability and ion selectivity, it was chosen as the substrate for transferring graphene. Following the same procedure for transferring to the SiN_x membrane, the graphene was transferred to the n-PETE membranes with a PMMA assisted method. The membrane resistance of the graphene transferred membrane is measured with EIS and compared with that of the pristine n-PETE membrane. It was found that the membrane resistance of the graphene transferred n-PETE membrane is five times higher than the original membrane, due to the high resistivity of graphene towards proton transfer. However, the ion selectivity of the membrane is not only determined by the proton conductivity/ resistivity, but also by the vanadium permeability. Springing, it was found that the vanadium permeability of this membrane is extremely low (**Figure 32b**). To verify the result, the diffusion test was proceeded for 3 days, while no trace of vanadium permeation was observed. Meanwhile, the n-PETE control sample shows measurable vanadium permeation even after a few hours' measurement. This results the graphene transferred n-PETE membrane almost completely rejected vanadium ion while still being permeable to proton. Therefore, the ion selectivity of this membrane is close to infinity, as suggested by the ion permeation test.

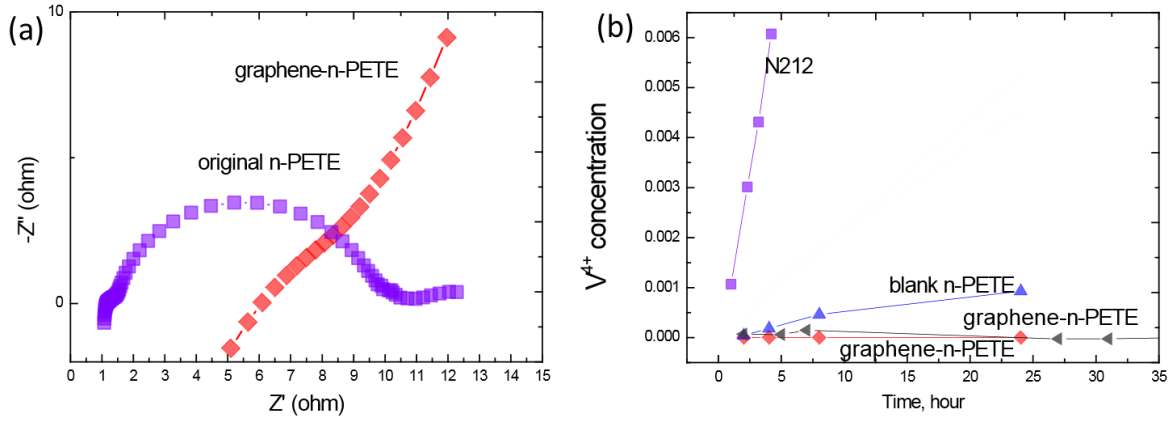

Figure 32. (a) Vanadium ion concentration vs time for the single layer graphene transferred n-PTET membrane (SLG-n-PETE), and (b) comparison of different n-PETE membranes.

Lastly, the VRFB performance of the n-PETE membrane was evaluated. A typical range of current density used for VRFB test is 20-100 mA/cm^2. However, this current range is found not suitable for testing the n-PETE membranes, because the active area of the n-PETE membrane is only 14% of its footprint area. For instance, when a current of 100 mA is applied, the equivalent current density for 1 cm^2 footprint area of n-PETE membrane equals to 100/0.14 = 714 mA/cm^2. This extremely high current density would result in a

large ohmic and ion transport overpotential. Thus, the current density adopted in this work is scaled down according to the active area (14%), by multiplying with a conversion factor of 0.14. The conversion between the actual applied current (2.8-28 mA/cm2) and the equivalent current density (20-200 mA/cm^2) is shown in **Figure 33b**. It was found that the pristine n-PETE membrane shows an acceptable performance of CE ~90%, VE ~95%, and EE ~85% at an equivalent current of 100-200 mA/cm^2 (14-28 mA/cm^2 actual current), similar to that of the Nafion 117. The results indicate the n-PETE membrane is well infilled, otherwise a much poor CE and EE would be observed due to the fast vanadium cross over through the defects.

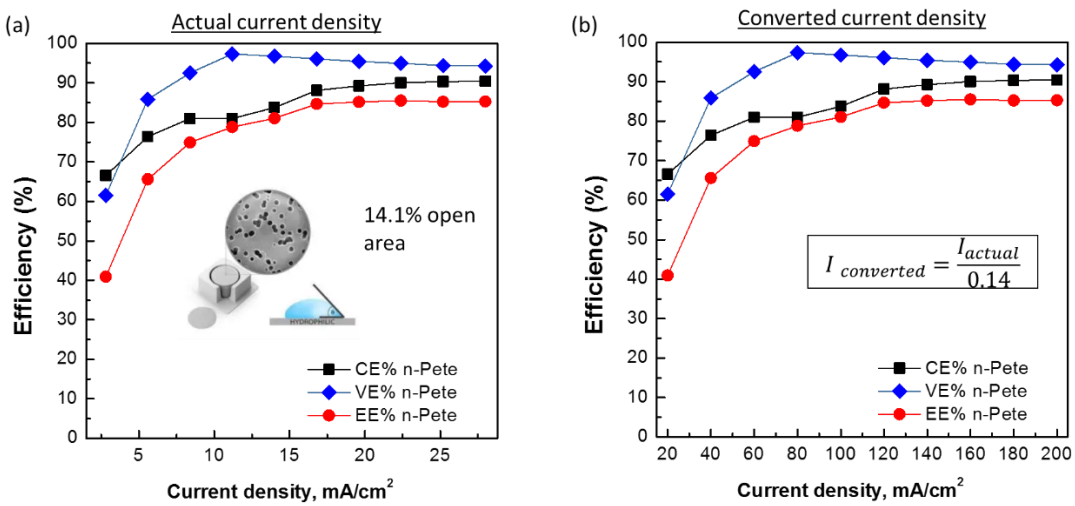

Figure 33. VRFB performance of n-PETE membrane at (a) actual current density, and (b) converted current density.

The VRFB with graphene-transferred n-PETE membranes were also tested under the same condition. Out of three tested membranes, two membranes (graphene-n-PETE-1 and graphene-n-PETE-2) showed higher CE than the pristine n-PETE membrane (**Figure 34**), mainly due to the mitigated vanadium cross over by the graphene layers. However, since the graphene layer can also impede the proton transport, the VE with these two membranes is lower than that of pristine n-PETE. As a result, the EE of the graphene-transferred n-PETE is close to that of the pristine n-PETE. It was found that another graphene-coated n-PETE membrane (graphene-n-PETE-3) showed almost the identical CE, VE, and EE as compared to the pristine n-PETE, presumably due to the large defective area on the graphene layer induced by the circulating electrolyte.

Despite some inconsistency, the battery performance results demonstrated the feasibility of using a graphene coating technique to regulate the ion selectivity and improve battery performance. To prevent the damage of graphene during the battery operation, one effective strategy is to make sandwiched membrane

by combinedly using the pore-filled PETE and PTFE membranes (**Figure 35**). In this sandwiched membrane, graphene is located between the two pore filled membranes, thus, avoided from the direct exposure to electrolyte solution

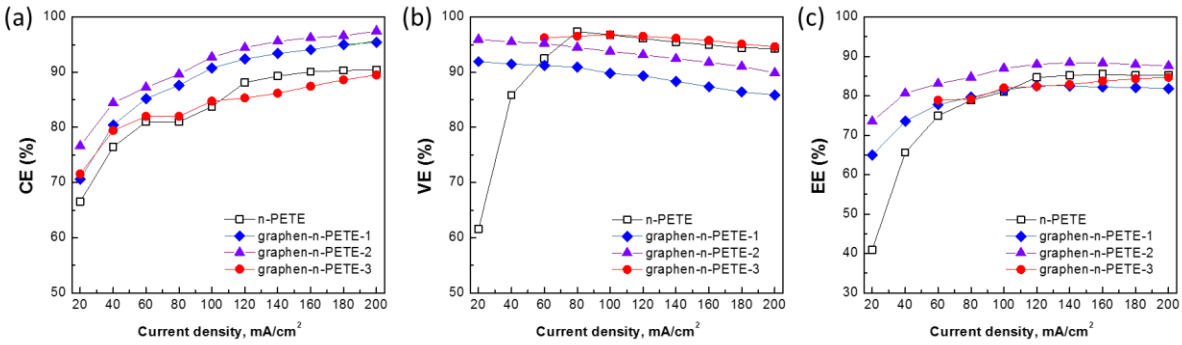

Figure 34. VRFB performance of n-PETE membrane and graphene-n-PETE membrane.

4.3.4 Summary

The effect of 2D layers on the ion transport was studied using a model SiN_x device. The ion transport measurement results indicated that 2D-graphene can effectively increase the proton/vanadium ion selectivity of the ion-conducting membrane. Further, by transferring graphene on a dimensionally stable pore-filled membrane substrate, an improved ion selectivity was achieved. The enhanced ion selectivity translates into better electrochemical performance in the flow cell charge-discharge test. Our results demonstrate the potential of using 2D films to develop hybrid proton exchange membranes (PEMs). Our findings in this study also helped to establish a firmer basis for designing superior hybrid membranes for RFBs and related applications. Nevertheless, the issues that limit current membrane development, such as the influence of defects and the high membrane resistance, still need to be addressed in future studies.

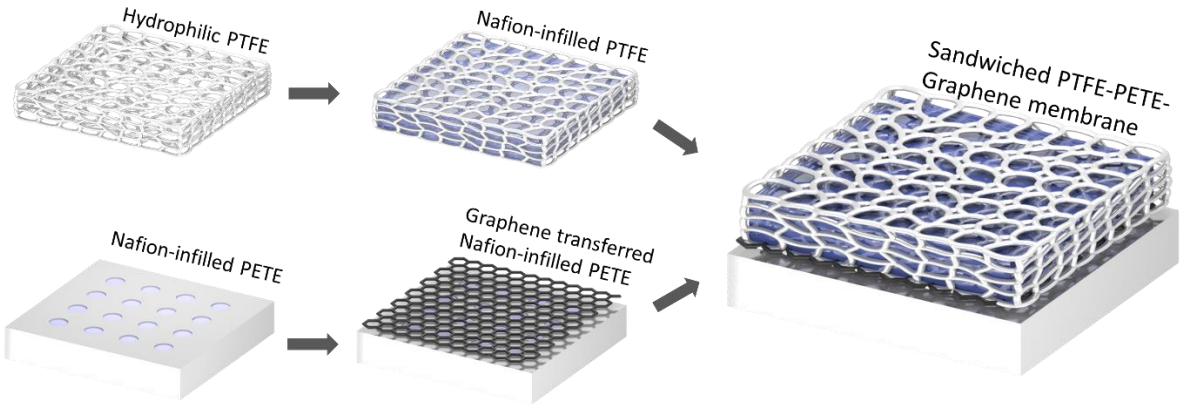

Figure 35. Proposed membrane structure for a sandwiched PTFE-PETE-Graphene membrane.

V. POLYSULFIDE-BLOCKING COMPOSITE ION EXCHANGE MEMBRANE FOR LITHIUM POLYSULFIDE (LI-PS) REDOX FLOW BATTERIES.

In Chapter 3 and Chapter 4, we have used vanadium redox flow batteries (VRFBs) to evaluate the performance of our membranes. However, the concept of VRFB has been raised about a few decades ago. Although MW-scale VRFB stations have been reported, the wide application of VRFB will be inevitably limited by their low energy density and the high cost of raw materials. Thus, it is imperative to develop a high energy density battery and the corresponding membrane technologies to meet the increasing demand for cost-effective, efficient smart-grid and vehicle electrification.

In recent years, lithium-sulfur battery (LSB) has attracted tremendous interest because of its high theoretical energy density (2567 W h kg^{-1}), natural abundance, environmental friendly, and low cost[129-131]. Despite its compelling merits, the practical application of conventional LSB using solid sulfur cathode is restricted by several technical and economic limitations: (1) the complicated carbon/sulfur cathode synthesis procedures are difficult to be generalized for large-scale manufacturing; (2) the actual battery capacity is limited due to the low sulfur loading and confined cell space; (3) the scalability of the LSB is still questionable because of the sluggish reaction kinetics and ion transport when it comes with higher sulfur loading and larger cell size. These obstacles severely impede the translation of the lab-scale LSB systems to commercially viable devices.[132] In this regards, lithium/polysulfide redox flow batteries (Li/PS RFBs), which utilizes liquid lithium polysulfide (Li_2S_8) catholyte to replace solid sulfur cathode (**Figure. 36a**), have gained extensive attention in recent years. This new battery technology integrates the high capacity feature of Li/sulfide chemistry and the general advantages of flow batteries, including flexible system design, safer operation, and long cycle life[49, 133]. These attractive features mitigate the aforementioned limitations of the conventional LSBs. Meanwhile, compared to the traditional aqueous flow batteries (e.g. all-vanadium flow batteries), Li-PS RFB shows advantages of higher energy density and much lower material costs, attributed to the natural abundance of the sulfur and lithium[49].

However, the critical issue that hinders the research progress of Li-PS RFB is the dissolution and crossover of soluble polysulfides (PS) intermediates. The repeated diffusion and migration of PS

between the sulfur/sulfide cathode and lithium anode can cause rapid capacity decay, poor coulombic efficiency, and unexpected electrode fouling[134]. This problem is especially detrimental for Li-PS RFB because of the exitance of highly concentrated PS in electrolyte. To address this challenging issue, one effective strategy is to employ a highly selective membrane separator which can suppress PS crossover while allowing fast lithium ion-conducting. Unfortunately, commercial battery separators (e.g. Celgard) are incompetent in addressing the shuttle effect since those membranes are freely permeable to polysulfide ions. Thus, the implementation of non-porous ion exchange membranes (IEMs) appeared to be a prospective manner, referring to their widespread adoption and recognized performance in many aqueous RFBs as ionic sieves(**Figure 36b**). Nonetheless, the conventional IEMs are unfavorable for Li-PS batteries due to their poor stability in non-aqueous solvent and insufficient Li^+/PS^- ion selectivity. Herein, to successfully adopt Li-PS RFBs for a large-scale electrochemical storage technology, it is imperative to develop new membrane materials that are chemically/electrochemically compatible with Li/PS chemistry while being able to efficiently suppress the polysulfide shuttling in Li/PS RFB.

In this study, we demonstrated a high-performance Li-PS RFB using a multifunctional and highly ion-selective bi-layered membrane, which is comprised of an ion-exchange polymer infiltrated carbon nanotube (CNT) layer and a boron nitride nanotube (BNNT) layer. A lithiated biphenyl-based ion-exchange polymer (BPSA-Li) was used in this study due to its outstanding ion selectivity and excellent stability in organic electrolyte. The CNT layer can effectively reduce interfacial resistance and play additional roles as mechanical support and PS absorbant[135-137]. The BNNT layer facing the lithium anode is used for further mitigate PS penetration and manipulate the lithium dendrite growth[138]. This wise combination lets the bi-layered membrane showing an almost complete rejection for polysulfide species while keeping a high ion selectivity. The Li-PS RFB assembled with the bi-layered membrane exhibit superior electrochemical performance, which makes it a promising technology for grid-scale energy storage as well as a broad spectrum of other applications.

5.1 Materials and characterization methods

Chemicals

All chemicals including, 1,2-dimethoxyethane (DME), 1,3-dioxolane (DOL), lithium bis(trifluoromethanesulfonyl)imide (LiTFSI) were purchased from Sigma-Aldrich and used without further purification. Lithium disulfide (Li_2S) and lithium metal foil were purchased from Fisher Scientific. Carbon nanotubes were provided by Samsung.

Membrane fabrication

The bi-layered CNT/BPSA/BNNT membrane was fabricated via the following steps. First, the CNT membrane was prepared by extending the Samsung CNT on a Teflon plate. Afterward, the CNT membranes were wetted by IPA and vacuumed overnight. The BPTA precursor was infiltrated into the CNT membrane afterward under vacuum and dried overnight to obtain the BPTA infiltrated CNT membrane. BNNT film was fabricated by a filter BNNT solution through a PVDF membrane. Subsequently, the BNNT film was peeled off and attached to the BPTA/CNT membrane surface using a 5% BPTA/NMP solution as glue. Later, the BPTA polymers were transferred into BPSA via extensive oxidation reaction inside 6M formic acid and 30 % H_2O_2 solution. The BPSA polymer was transferred into -Li form by immersing in 1.0 M LiOH in H_2O: ethanol (1:1 by weight) mixture at 80 °C for 12 h under stirring. The resulting lithiated membrane film was subsequently rinsed in deionized water to remove the remaining salt and solvent. After vacuum drying at 60 °C overnight, the membrane was transferred into an argon-filled glove box and immersed in the electrolyte solution before conductivity or battery test.

Characterization of CNT/BNNT/BPSA double-layer membrane

The morphology of the bilayer membrane was characterized by field emission scanning electron microscope (FESEM, Hitachi S4800). AFM measurements were performed on a TT-2 AFM (AFM workshop) in the tapping mode. Raman spectra were obtained at room temperature using the confocal Raman microscope (Raman-AFM, WITec alpha 300 RA). The excitation wavelength was 532 nm from a Nd:YAG laser.

Polysulfide Permeation test

The polysulfide permeability across the membranes was evaluated by using a diffusion cell inside Argon filled glovebox. The feed side reservoir was initially filled with 0.1 M Li_2S_8 in DOL/DME (1:1, v/v) solution and the permeate side reservoir was filled with the same amount of DOL/DME

(1:1, v/v) solution. A magnetic stirrer was placed in each cell and kept for stirring during the test to avoid concentration polarization. The polysulfide concentration at the permeant side was monitored using UV-Vis spectroscopy. The testing samples were sealed carefully in a UV quartz cuvette with Teflon screw cap and septum, then quickly transferred to UV chamber for testing. The PS concentration was determined from the changing of absorbance signals. The PS permeability through the membrane was calculated from Fick's law:

$$\mathrm{V}_B \frac{d\mathrm{C}_B(t)}{dt} = \mathrm{A}\frac{P}{L}\left(\mathrm{C}_A - \mathrm{C}_B(t)\right)$$

where V is the volume of solution, C_i is ion concentration, t is time, A is area, P is permeability, and L is membrane thickness.

Conductivity measurement

The conductivity of the membrane was tested by electrochemical impedance spectroscopy (EIS). Before the measurement, the prepared membranes were immersed in 1M lithium bis(trifluoromethylsulfonyl)imide (LiTFSI) in 1:1 volume ratio of 1,3-dioxolane (DOL)/dimethyl ether (DME) solution for 1 day. Soaked membranes were sandwiched between two stainless steel electrodes. Potential electrochemical impedance spectroscopy (PEIS) was tested with 50 mV AC bias scanning from 1 MHz to 100 mHz. The high-frequency x-axis intercept was taken to be the resistance of the membrane. The membrane conductivity was then calculated using the equation:

$$\sigma = \frac{L}{A \times R}$$

Where σ is the conductivity, mS/cm; L is the membrane thickness, cm; A is the active area, cm2; and R is the membrane resistance, Ω.

Battery test.

In the single RFB cell, lithium foils were employed as anode and PS (Li_2S_8) solution was used as catholyte. The 1M Li_2S_8 catholyte solution was prepared by reacting stoichiometric amounts of Li_2S in electrolyte (DOL/DME v/v = 1:1) at 70 ^{o}C for 24 hour[139] and then diluted to the desired concentration. 1M LiTFSi was added to the solution as supporting electrolyte and stirred overnight. Before each test, the membranes were soaked in the corresponding electrolyte solution for 1 day. During the test, the catholyte solution was circulated through the battery using a peristaltic pump

connected with Teflon tubing kits (Cole-Parmer). The structure and photo of the RFB single cell is displayed in Appendix I. The batteries were charged and discharged on an 8-channel battery analyzer (MTI Corporation). The voltage range for cycling was controlled between 2.15 to 2.8 V, to prevent the formation of insoluble polysulfide species, e.g. Li_2S and Li_2S_4. The single stationary battery test was performed using a Swagelok-type cell, in which lithium metal was used as an anode and liquid polysulfide solution as catholyte. The voltage range for the rate and cycle test is 1.7-2.8 V.

5.2 Results and discussion

A schematic working principle for the bi-layered membrane is demonstrated in **Figure. 36c** and is compared with the conventional porous separators, e.g. Celgard. It is well known that the PS

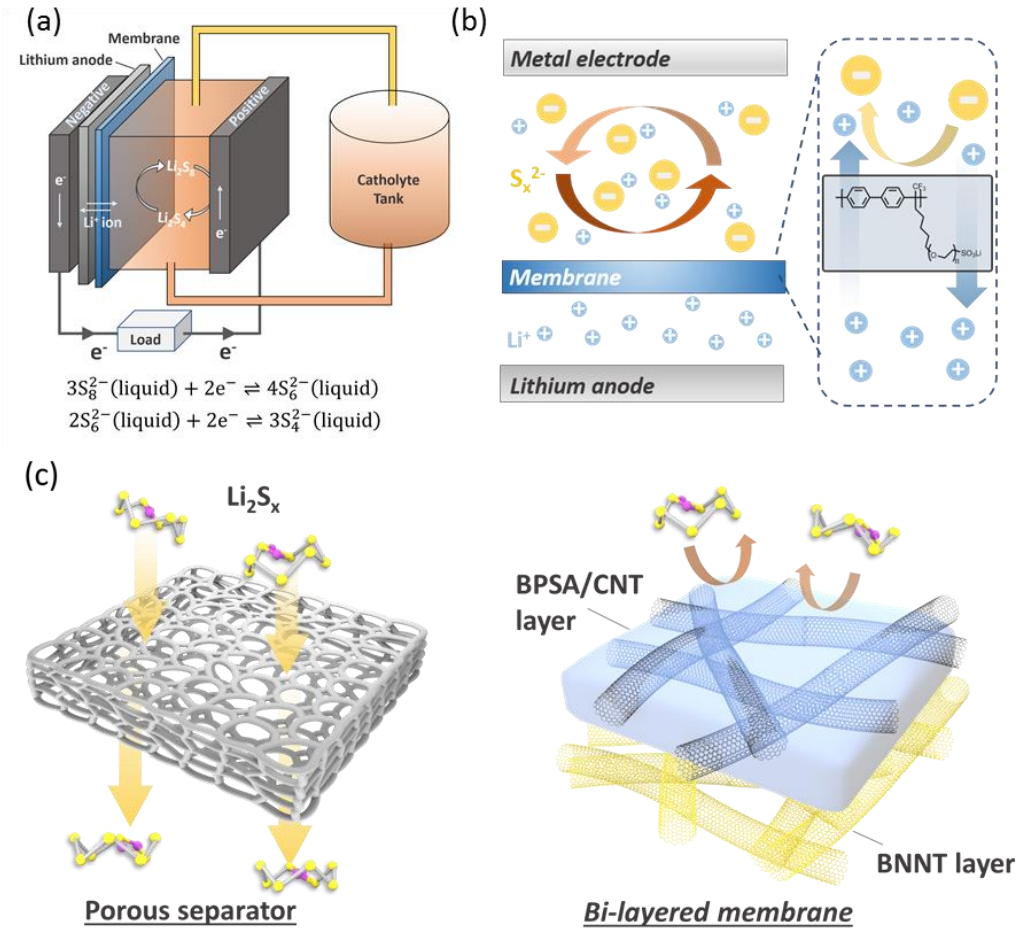

Figure 36. (a) Schematic illustration of Li-PS RFB and (b) concept of using ion exchange membrane to attenuate polysulfide shuttle effect. (c) Working principle of the CNT/BPSA/BNNT bilayer membrane and comparison to conventional porous separator.

species can travel freely through the porous structure of Celgard and react with the anode. In this case, the separator solely functions as an electronic insulator between cathode and anode. Unlike the porous separators, ion exchange membranes (IEMs), which possess negatively charged groups, allows the traverse of lithium-ion in the supporting electrolyte while repels polysulfide anions via Donnan interaction. Subsequently, a superior Li^+/PS selectivity can be achieved by IEMs. However, the traditional ion exchange membranes typically exhibit significant dimensional change in the organic electrolyte, which lets the membranes lose their ion selectivity and mechanical strength. Therefore, we fabricate our composite membrane by using a biphenyl polymer, BPSA-Li, which is highly stable in the 1,3-dioxolane (DOL)/1,2-dimethoxyethane (DME) organic solvent. As demonstrated in Appendix Fig. A8, the membrane keeps its dimensional integrity after soaked in DOL/DME (1:1 vol) for 48 hours with negligible swelling or shrinkage observed. Further, we rationally engineered our membrane structure by infiltrating the BPSA-Li into an entangled CNT layer and subsequently covered with a BNNT layer, in order to acquire the desirable functionalities from these inorganic nanomaterials. The highly conductive CNTs can reduce the interfacial resistance between membrane surface and carbon electrodes, while the BNNT layer could curb the lithium dendrite growth and prevent short circuit through the connection of CNT to lithium metal.

The morphology of the membrane was characterized using scanning electron microscopy (SEM) (**Figure 37**). As shown in the SEM images in **Figure 37 a-d**, the bi-layered membrane possesses 2 distinct layers with thickness ~5 μm. These two layers are attached together by a very thin polymer glue layer. The top and cross-sectional view of the CNT/BPSA layer were displayed in **Figure 37 a&b**. It was found that the CNT layer has been entirely infilled with BPSA-Li polymers and no pinholes and defect are observed. On the other side of the CNT/BPSA layer, a porous BNNT layer was uniformly deposited without agglomeration. (here we need to add a description for AFM images after data is collected.) The quality of CNT was examined by Raman spectroscopy. As shown in the Appendix Fig A7, the ratio for the intensity of the G-band peak (I_G) over the D-band peak (I_D) is close to 20, indicating the CNT is highly graphitized, which usually gives higher electronic conductivity.

The permeation resistance to the active species crossover is a crucial criterion for membrane/separator used in redox flow battery[140]. To quantitatively evaluate the polysulfide-blocking ability of our bilayer membrane, a polysulfide permeation test was performed on the bi-layer membrane, commercial porous membrane (Celgard), and benchmark ion exchange membrane (Nafion). During the permeation experiment, the amount of polysulfide permeate across separators can be measured using UV-vis spectroscopy. For a bilayer membrane, there is no detectable UV signal of polysulfides (Li_2S_8) in the permeate side solution within a period of 24 h (**Figure. 38**), demonstrating an excellent sieving effect toward polysulfide species. In comparison,

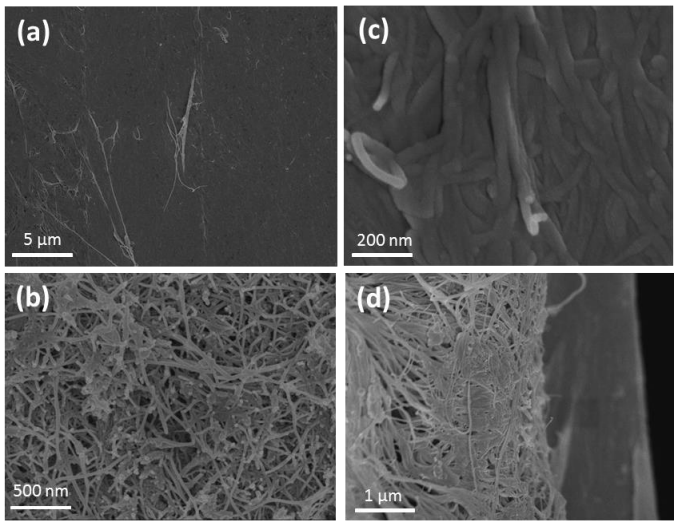

Figure 37. SEM image of (a) CNT layer (low resolution), (b) top surface (high resolution), (c) bottom surface, and (d) cross-section of BPSA/CNT/BNNT bilayer membrane.

the polysulfide species can pass quickly through the Celgard and Nafion membrane, as evidenced by a sharp increase of polysulfide concentration in the permeate solution (Figure 38a). From the quantitative result obtained by UV measurement, we further calculated the PS permeability of the tested membranes based on the approximation using Fick's law. The permeability of PS across Celgard and Nafion was found to be 2.2×10^{-7} and 3.6×10^{-8} cm^2/s, respectively. In comparison, the PS permeability across the bilayer membrane is almost negligible ($<1 \times 10^{-11}$ cm^2/s, which is the smallest number can be capture using our UV). The superior rejection property of our bilayer membrane is also evident from the color change of the collected permeation solution (Figure 38b). The permeate solution adjacent to the bilayer membrane is almost transparent after 24 hours of permeation test, while the solution with Nafion has already turned into yellow color, indicating the traversing of a considerable amount PS species across the separators.

The effect of membrane separators on the battery electrochemical performance was further evaluated. A Swagelok-type stationary cell was first employed as a model testing system. To mimic the flow battery, the stationary cells utilize the polysulfide (Li_2S_8) solution as the starting catholyte, a porous carbon as electrode, a lithium metal foil as an anode, and two stainless steel current collectors. The electrochemical performance of these batteries was first characterized by cyclic voltammetry (CV) and electrochemical impedance spectroscopy (EIS) measurement. The CV test was performed in a voltage range of 1.6-3.0 V *vs.* Li/Li^+ with different scan rates. As shown in **Figure 38d**, typical cathodic peaks at 1.8-2.1 V and 2.3-2.4 V, and an anodic peak at 2.4-2.5 V are observed with all separators. Till now, only the CV curve with bilayer membrane has been collected, the curve with other membrane will be updated in the future experiments.

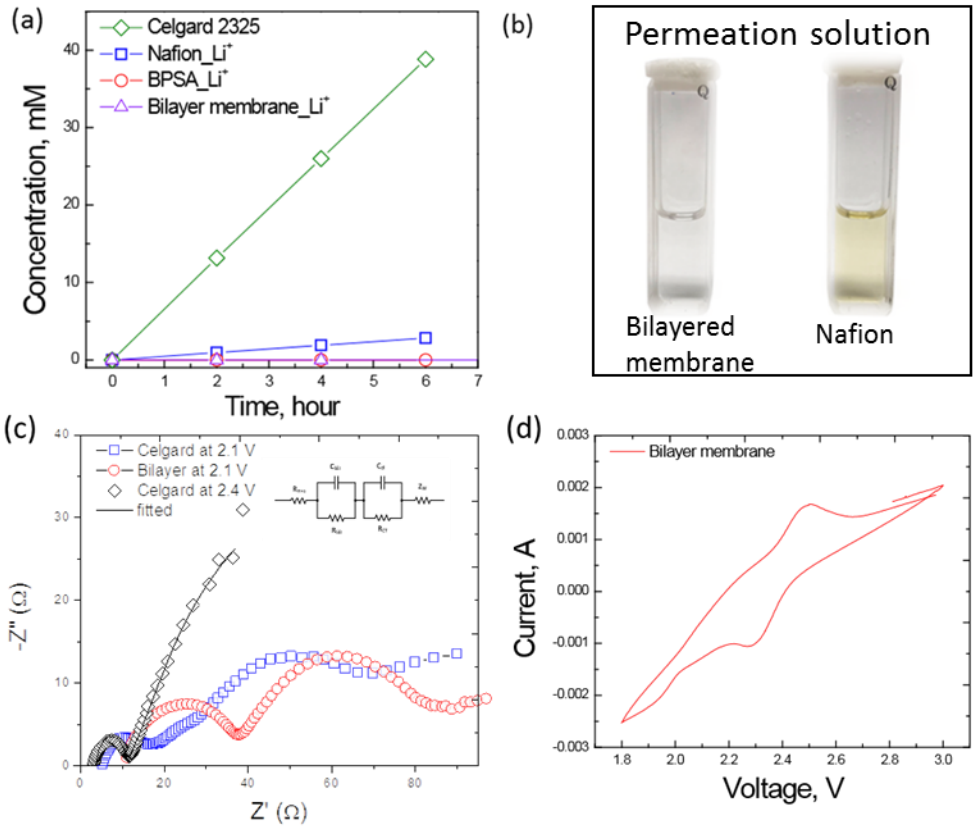

Figure 38. Membrane ion transport property and electrochemical performance. (a) PS concentration in permeate solution vs time. (b) digital photo of the permeation solution after diffusion test. (c) EIS curves of Li-PS batteries. (d) cyclic voltammetry curve of the Li-PS battery.

The battery systems with various membranes were also investigated by performing the EIS tests at a lower and higher open circuit voltage (OCV). To acquire detailed information, the EIS spectra are fitted with an appropriate equivalent circuit (**Figure. 39c**), in which R_0 represents the membrane ionic resistance, R_{inter} is the interfacial resistance between membrane and electrode, and R_{ct} is the charge transfer resistance. It is well known that the low membrane resistance and high ionic conductivity are essential for achieving satisfactory voltage efficiency and high sulfur utilization. Here we calculated the through-plane conductivity of membranes using the membrane ionic resistance (R_0) obtained from EIS spectra (Table 11). Of note, although the conductivity of the bilayer membrane (0.017 mS/cm) is slightly lower than the lithiated Nafion (0.046 mS/cm), the its resistance (30.1 Ω) is comparable to that of Celgard (4.6 Ω) and Nafion (107.2 Ω) by optimizing the thickness. More importantly, it was found that the interfacial resistance (R_{inter}) of the bilayer membrane is much less than that of Nafion and Celgard. The interfacial resistance is usually affected by solid sulfur/sulfide layer formed in between membrane and electrode. Therefore, a likely cause for the lower interfacial resistance of the bilayer membrane could be that most polysulfides have been retained to the cathode side, which prevents the formation of a solid layer on the lithium metal surface[141]. Moreover, according to Manthiram, et al.[142], conductive CNTs can provide electro pathway through the insulating sulfur/sulfide layer by contacting directly with the carbon cathode, which could be another factor contributing to the lowered interfacial resistance. As evidenced from these experimental results, the bilayer membrane demonstrates significantly improved PS blocking efficacy while keeping a high selectivity, showing great potential to be used as separators for the lithium polysulfide batteries.

Table 11. PS diffusivity, ion conductivity and selectivity of membranes.

Membrane	**Thickness (μm)**	**Swelling ratio %**	**Areal Resistance (Ω cm^2)**	**Conductivity (mS/cm)**	**PS Permeability (cm^2/s)**	**PS Permeance (cm/s)**	**Selectivity (mS.s/cm^3)**
Celgard 2325	25	~0	4.6	0.539	2.2×10^{-7}	8.8×10^{-5}	2.45×10^{6}
Nafion 212	50	~50-70%	107.2	0.046	3.6×10^{-8}	7.2×10^{-6}	1.28×10^{6}
Bilayer membrane	15	<1%	30.1	0.017	$<1 \times 10^{-11}$	$<2\times 10^{-8}$	N/A

The battery assembled with different membranes was galvanostatic charged and discharged in a voltage window of 1.6-3.0 V step wisely from 0.25-1 C-rate. As shown in **Figure 39**, the charge-

discharge curves with all three membranes exhibit two typical discharge plateaus around 2.3 and 2.1 V, corresponding to the reduction processes of $S_8 \rightarrow Li_2S_{4-6}$ and $Li_2S_{4-6} \rightarrow Li_2S_{1-2}$, respectively. The bi-layered membrane shows a much better rate performance than Celgard. Note that the battery didn't work properly with Nafion, presumably due to its high resistance.

Lastly, the performance of bilayer membranes was examined on the Li-PS flow battery circulated with 0.1-0.3 M of PS solution. The flow battery assembled with bilayer membrane, Celgard and

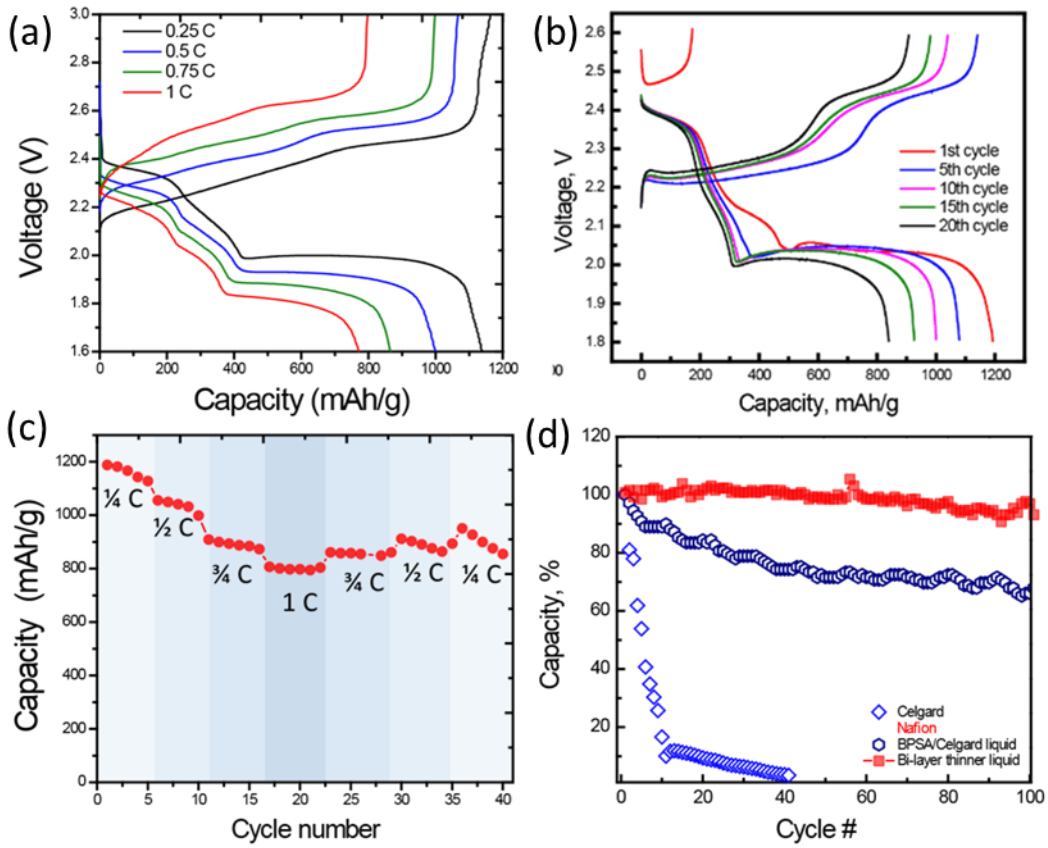

Figure 39. Battery performance evaluation. harge discharge curve with bilayer membrane at (a) different c-rates, and (b) different cycles. (c) rate performance for the Li-PS battery with bilayer membranes. (d) capacity retention of the Li-PS RFB with different membranes.

Nafion was charged/discharged for 100 cycles with a cut-off voltage of 2.15 V for discharge. The narrower potential window used here was mainly to prevent the formation of insoluble Li_2S and Li_2S, which would otherwise lead to the clogging of porous carbon and pipeline. The capacity retention of Li-PS RFB with different membranes was displayed in **Figure 39d**. The RFB with a bi-layered membrane shows a capacity retention of 90% after 100 cycles. In comparison, the capacity retention with Celgard and BP-Sa coated

Celgard membranes are only <10% and 70%, respectively. This significantly enhanced capacity retention is contributed by the much lower polysulfide diffusivity of the bi-layer membrane than BP-SA coated Celgard membrane and Celgard, which effectively mitigates the PS shuttle phenomenon and prevent the lithium surface corrosion.

5.3 Summary

In summary, we have designed and prepared a bilayered composite ion exchange membrane for lithium–polysulfide redox flow battery. The membrane is comprised of a BNNT layer and a CNT layer infilled with ion-exchange polymer (BPSA). It was found that the bilayer membrane plays the role of an efficient ionic sieve towards polysulfides while having a negligible influence on the transfer of Li^+ ions across the separator. Moreover, the proposed separator can retain its structural stability and reliability under electrochemical conditions in Li-PS cells. The Li-PS RFB with the bilayer membrane exhibited sustainably enhanced cycling stability and a lower capacity-fading rate. The strategy demonstrated here may guide us in developing functional separators for high energy density and low-cost organic-based redox flow battery.

VI FROM 2D TO 3D: NANOENGINEERED 3D NM-THICK BIOMIMETIC MEMBRANE FOR ULTRAFAST SELECTIVE MASS TRANSPORTATION

(Previously published as Wang, T., Liang, S., Qi, Z., Biener, M., Voisin, T., Hammons, J. A., & Biener, J. (2020). "A 3D nm-thin biomimetic membrane for ultimate molecular separation." *Materials Horizons*, DOI: 10.1039/D0MH00853B -Reproduced with permission from The Royal Society of Chemistry.)

The ultimate goal in membrane technologies is to combine high permeability and high selectivity. Nature resolved these challenges by developing complex three-dimensional (3D) functional membrane architectures that provide organs like kidney, liver, lung, and intestinal villi with their unique functionalities. In particular, the formation of urine is a process that begins with the glomerular filtration in kidney. In the average 70 kg adult, glomerular filtration rate is about 180 L/day of glomerular filtrate and such high filtration rate is mainly based on hydrostatic pressure and its unique 3D morphology comprising of a bundle of capillaries with 645 cm^2 of filtration area per 100 cm^2 of projected area (left panel of **Figure 41a**)[143]. Conventional approaches to fabricate high-performance synthetic membranes, however, are still based on two-dimensional (2D) structures, suffering from the trade-off relationship between the permeability and selectivity. In recent years, the development of ultra-thin membranes has attracted much attention [144-147], which increases the overall flux via shortening the mass transport pathway. However, the surface area of 2D membranes is intrinsically limited, not to mention the high probability of membrane failure due to the poor mechanical stability of ultra-thin membrane structures. Other than a 2D flat-sheet structure, rippled nanofilm geometries were reported to increase the surface area and hence improve the permeance [148, 149]. However, the ripples in these membrane structures were not self-supportive so that further increase the surface area for performance optimization is limited.

Inspired by the glomerular structure, we have engineered a self-supportive 3D nm-thin membrane (3DM) with well-defined architectures that can offer extremely high filtration area, ultra-short pathway via nm-thin selective layer, and low tortuosity for fast mass transport. To realize the 3DM, we use modified nanoporous gold (np-Au) with bi-continuous unimodal pore size distribution, as a template to generate two independent, interwoven mesopore channels resembling the morphology of nature's 3DMs. We employ atomic layer deposition (ALD) with a self-limiting character that warrants uniform and conformal coatings with atom-scale thickness control, to produce highly selective nm-thin membrane. The derived 3DM is self-supportive since each tubular ligament is connected three-dimensionally with adjacent ligaments, resulting in excellent stiffness and strength[150, 151]. Extraordinary separation performance is also demonstrated in this work.

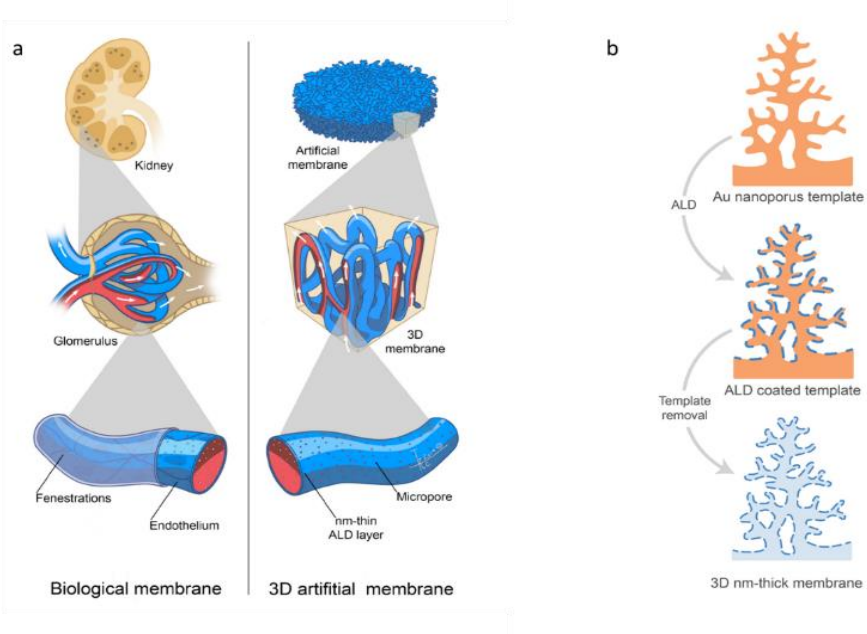

Figure. 40 Conceptional designs and fabrication schematics. (a) Morphological schematics of glomerulus filtration in kidney and 3D membrane. (b) 2D illustrations of the 3D nm-thin membrane fabrication from nanoporous gold templating plus atomic layer deposition (ALD) approach. The fabrication details can be found in Appendix III.

6.1 Materials and characterization methods

Fabrication of 3D membranes

A sheet of $Ag_{70}Au_{30}$ alloy was cut into ~ 200 μm thick discs with ¼ inch in diameter. The disc samples were annealed at 900 ºC in air for 12 h before being dealloyed by concentrated nitric acid at room temperature for 48 h. The resulting nanoporous discs were washed by deionized water and dried in air. Thereafter, a thin layer of gold (approximate 500 nm) was sputtered onto one side of the discs to make closed nanochannels in the nanoporous gold discs (top panel of **Figure. 40b**). Then nanometer thick Al_2O_3 and TiO_2 films were deposited onto the nanoporous gold templates (middle panel of **Figure. 40b**) by ALD using the well-established trimethyl-aluminum ($AlMe_3/H_2O$) and titanium tetrachloride ($TiCl_4/H_2O$) ALD processes in a warm wall reactor (wall and stage temperature of 125 ºC for Al_2O_3 and 110 ºC for TiO_2) on ALD-200L system (Kurt J. Lesker Company). Long pump, exposure, and purge times (20/300/300 s) were used to ensure the gas precursors penetrate through the np-Au discs and achieve uniform coatings. The Al_2O_3/gold and TiO_2/gold samples were immersed into a mixture of 2 g KI, 1 g I_2, 2 g H_2O, 8 g acetone and 8 g ethanol for 48 h to totally remove the gold template (bottom panel of **Figure 40b**). The additional freestanding 2D ALD film on the sealing Au layer will peel off automatically, leaving the inner tubular channel opened on this side, which we note as a negative side (right panel **of Figure. 40a**). The final discs

were rinsed with acetone and then dried by super critical CO_2 drying process to afford semitransparent 3D membranes of Al_2O_3 or TiO_2.

Structural, morphological, and compositional characterizations

The morphology of the 3D membranes was characterized with a field emission scanning electron microscope (JEOL 7401-F) at 20 keV (20 mA) in secondary electron imaging mode with a working distance of 5-8 mm. Transmission electron microscopy (TEM) was conducted using Philips CM300 FEG system. Specific surface area and pore size distributions were analyzed by nitrogen adsorption/desorption isotherms using Brunauer-Emmett-Teller (BET), Barret-Joyner-Halenda (BJH), and density functional theory (DFT) methods, with an ASAP 2020 surface area analyzer (Micromeritics Instrument Corp.). We note that this porosity analysis cannot detect pore sizes smaller than the diameter of N_2 molecule itself (3.64 Å).

Small Angle X-ray Scattering (SAXS) modeling

In order to resolve the wall thickness and heterogeneity, SAXS experiments were conducted in the q-range: $0.05\ Å^{-1} < q < 2.5\ Å^{-1}$. Only data out to $q = 0.7\ Å^{-1}$ was analyzed using small angle scattering theory, which can resolve scattering heterogeneities between 1 nm and 12 nm[152]. The SAXS experiments were performed at the Advanced Light Source, beamline 7.3.3 using monochromatic X-rays with a wavelength of 1.2398 Å and a beam area of 0.3 mm by 0.7 mm. The as-prepared TiO_2 membranes were placed in the beam such that the entire membrane thickness was oriented normal to the X-ray beam path. Only the electron density fluctuations on the length scales associated with the TiO_2 wall were resolved, while the size of the inner and outer tube radii (~50 nm) and overall fibrous network (100s of nm) were not; these dimensions would only be accessible by scattering at lower q. Detailed SAXS analysis and modeling can be found in Appendix.

Zeta potential measurements and surface charge calculations

The zeta potential was measured using streaming current method on a SurPASS 3 electrokinetic analyzer (Anton Paar GmbH, Graz, Austria). Sample size is 10 mm × 20 mm. A 1 mM KCl electrolyte was used for the measurement. The electrolyte was purged with nitrogen for 10 minutes prior to the measurement and during the entire measurement to prevent the dissolution of CO_2. A pH scan measurement was performed beginning at pH 5.5 (pH of fresh 5 mM KCl) and ramped down to pH 3 by the addition of 0.05M HCl. The zeta potential was determined at roughly every 0.5 pH units after the sample was rinsed for 5 minutes using the pH adjusted electrolyte. A basic pH ramp was then performed by following the exact same procedure as above. The pH, in this case, was adjusted by the addition of 0.05M NaOH.

Membrane characterization

Gas and water transport properties of the 3DM were characterized by the method described in our previous studies[153-155]. For the evaluation of gas permeance, the flux of gas through the 3D membrane was measured using a constant pressure system equipped with a calibrated digital mass flow meter. To evaluate whether there is any viscous flow through any large pinholes or large structural defects, N_2 permeability of the 3DM was measured at different pressure in a range of 0.1 to 10 psi. After the 3DM showed the independency on the applied pressure, other gases such as H_2, He, CH_4, Ar, and CO_2 were tested[153].

For the evaluation of the dye molecule/ion rejection, typical ion rejection test for the characterization of nanoporous membranes was carried out using home-made filtration cell as described in detail elsewhere[153, 155]. Low-concentration electrolyte solutions were used throughout this study to ensure that the Debye length (λ_D) was large enough so that a complete double-layer overlap could be achieved within the nanochannels. For the pressure driven-flow test, 2mL of feed solution (e.g. 0.3mM of PFCN) was pressurized at 0.69 bar with a controlled nitrogen gas line, while the permeate was at atmospheric pressure. After 200 μl of solution permeated through the membrane, permeate solutions were collected for UV-analysis[153, 155]. The detailed UV-vis spectroscopy data can be found in Appendix.

In the osmotic pressure method, the osmotic water flux measurement cell was fabricated using 3D printer (Form 2 printer, Formlabs, Somerville, MA, USA). Each cell composes of a chamber in connection with a square-shape capillary tube (0.25 cm^2 cross-section area), as shown in Appendix Fig. S3. At the beginning of the measurement, 10.0 ml of 1.0 mM DB71 dye and deionized water were filled in the feed side and permeate side of the cell, respectively. The solution at both sides of the cell was mixed continually by magnetic stirrers to reduce external concentration polarization. At initial stage, the solution in the capillary tube in both cells were at the same level. The volume change in both cells was calculated by measuring the difference of the solution level at designated time interval. The concentration of the dye in both cells was measured using UV-vis spectroscopy at the same time interval to correct the osmotic pressure difference, which caused by the change of concentration over time. The increase of the difference of the solution level can result in the change in pressure difference across the membrane, which was taken into consideration for the calculation of the osmotic water permeance[156].

In the diffusion set-up for the Donnan exclusion test, a 10 ml solution with dye/ion concentration of 0.1 mM was filled in the feed side of the cell and same amount of DI water was fill in the permeate side cell (PermeGear, Inc. USA). The solution in each cell was continually mixed by magnetic stirrers. The collected permeate solution were analyzed subsequently by UV-1800 ultraviolet-visible spectrophotometer (Shimadzu. Japan) to determine the concentration of the ions. The permeability of the ions was calculated by linearly fitting the concentration in the permeation solution with time.

Li^+ conductivity and Li_2S_8 diffusion test

Li^+ conductivities of the 3DMs with varying ALD TiO_2 layer thicknesses were measured by placing them in between two Li metal electrodes with fixed spacing filled with liquid electrolyte. The Li metals are in contact with two stainless steel current collators. 1M Lithium bis(trifluoromethanesulfonyl)imide (LiTFSI) in Tetraethylene glycol dimethyl ether (TEGDME) was used as the liquid organic electrolyte. lectrochemical impedance spectroscopy (EIS) was recorded using a VSP-300 multichannel potentiostat (Bio-Logic Science Instruments). The solution and contact resistances were removed as background to obtain the resistance from the 3DMs. For the Li_2S_8 diffusion test, solution was prepared as described in detail elsewhere[103, 157]. One side of the diffusion cell was filled 0.1 M Li_2S_8 in 1,3-dioxolane/1,2-dimethoxyethane (DOL/DME, 1:1 by volume) and another side reservoir was filled DOL/DME solution. A magnetic stirrer was placed in each side of diffusion cell to prevent concentration polarization. The concentration of the S_8^{2-} ion was monitored using UV-Vis spectroscopy.

6.2 Results and discussion

6.2.1. Structural, morphological, and compositional properties

The fabrication process of the 3DM is shown in **Figure 40b**. Detailed information can be found in the Methods section. As illustrated in **Figure 40b** and evidenced in **Figure 41a**, both the inner and outer tubular channels of 3DM are three dimensionally self-connected and separated by a porous TiO_2 layer, resulting in a gyroid-like membrane morphology that ensures no closed spaces or voids in the membrane structures. For the 3DM application, it is critical that only one of the two independent pore system can be accessed from each side of the membrane. Here, we call the side opened to the outer tubular channel as positive side (left panel of **Figure. 41a**), while the other side opened to the inner tubular channel as negative side (right panel of **Figure. 41a**). Although pinholes cannot be theoretically excluded, high resolution scanning electron microscope (SEM) and abbreviation-corrected high-resolution transmission electron microscope (TEM) (**Figure. 41b & c**) analysis did not detect any large-sized pinhole or structural defects. Fig. 2d shows the pore size distribution measured using N_2 desorption isotherm. The pore size around 50 nm is attributed to the diameter of inner and outer tube channels determined by the np-Au template. The micropores below 2 nm are attributed to selective pores in the TiO_2 layer which exhibit a size distribution between 0.4-0.8 nm and 1.1-1.7 nm. The existence of sub-nm pores in amorphous TiO_2 is expected due to the fluctuation of local bonding conditions. In order to explain the relationship between TiO_2 layer structure and pore size, we employed small-angle X-ray scattering (SAXS) analysis based on a concentric cylinder shell model (Fig. 2e)[158]. The results confirm that the ALD layer thickness only varies by 6% throughout the 200-μm-thick sample (see Appendix for details). The χ^2 obtained from the SAXS model can be improved by introducing heterogeneous electron density fluctuations (on the order of ~ 1 nm) in the ALD layer by simulated annealing. While only heterogeneity normal to the wall surface can be accounted for in the SAXS modeling,

the size of the fluctuations in **Figure. 41e** are in good agreement with the microporosity observed in the N_2 desorption experiments. The one-side volume-specific surface area of a 4-nm-thin TiO_2 3DM is 3.0×10^4 m^2/L as determined by Brunauer-Emmett-Teller (BET) analysis, which is larger than the surface area of the corresponding np-Au template (2.3×10^4 m^2/L). Extra 7,000 m^2/L surface area may be attributed to the micropores within the ALD layer. The surface area for the entire 200-μm-thick sample is 6,000 times larger than the footprint area, which greatly enhances the mass transport through the 3D ALD layer.

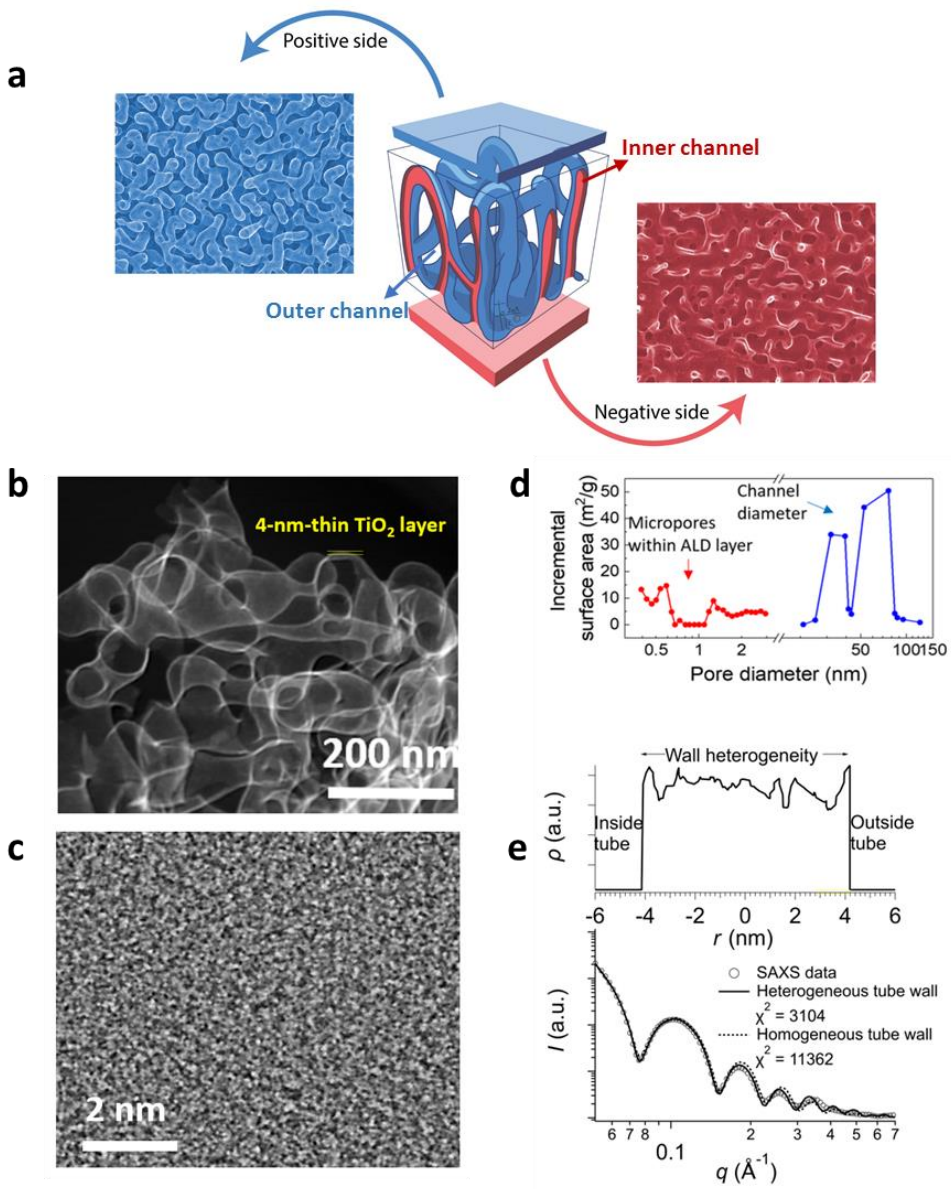

Figure 41. Morphological and pore size characterizations. (**a**) SEM images of the positive side (blue) and negative side (red) of the 3DM. (**b**) High-resolution transmission electron microscopy (HRTEM) image of 3D membrane. (**c**) Aberration-corrected HRTEM image of an amorphous TiO_2 selective layer. (**d**) Mesopore size distributions (blue) calculated from Barrett-Joyner-Halenda (BJH) methods and micropore size distributions (red) based on density functional theory (DFT). The split of the peak around 50 nm is due to the channel size difference as the np-Au used here has 70% porosity, making the outer tube channel larger than the inner tube channel. (**e**) Log-log plot of the background subtracted SAXS data (grey circles) with the least squares fit of a narrow size-distribution of hollow cylinders with a homogenous shell (dashed line) and a heterogeneous shell obtained by simulated annealing of the electron density within the shell (solid line). The scattering length density of the heterogeneous shell wall obtained by simulated annealing is shown in the top graph.

6.2.2. Separation performance

The gas permeance through a 2-nm-thin 3D TiO_2 membrane as a function of the inverse square root of the molecular weight, M_w, shows a nearly linear relationship with a bit offset for H_2 (**Figure. 42a**). This suggests that the gas transport through our 3DM is mainly dominated by Knudsen diffusion where the mean free path of gas molecules is larger than the pore width. A H_2 permeance of 3.4×10^{-5} mol m^{-2} s^{-1} Pa^{-1} is achieved with a H_2/CO_2 separation factor of 6.09. The higher separation factor than theoretical Knudsen prediction (4.69) implies that enhanced H_2 interaction with TiO_2 may play a role [159, 160]. The H_2 permeance of the 3DM is at least one order of magnitude higher than other sub-nm pore membranes (e.g. silica [161], graphene [162]) or mesoporous membrane[163] due to synergic effect of high surface area and thin selective layer (inset in **Figure. 42a**).

Water permeation rates through the 3DM were measured using two different methods: the pressure-driven flow and the osmotic pressure method. In the pressure-driven flow test, external pressure (6 psi) was directly applied to a home-made filtration cell[153, 155, 164]. The water permeation rate under the external pressure was found to be ~1,260 L m^{-2} h^{-1} bar^{-1} (calculated based on footprint-based surface area). For the osmotic pressure method, the water flux of the 3D nm-thick membrane was measured using a home-made diffusion cell fabricated via 3D printing. 1 mM DB71 solution was used as the drawing solution to generate osmotic pressure gradient (0.35 psi). The UV-vis spectrophotometer result showed that there was no trace of DB71 in the permeation solution after 48 hours of measurement, indicating a complete rejection of the DB71 molecules. Since the membrane has high rejection towards DB71, the change of the osmotic pressure caused by the diffusion of DB71 is negligible. As shown in Appendix Fig. S3, the dye solution level in the left reservoir increases quickly, and membrane shows a water permeability of 892 L m^{-2} h^{-1} bar^{-1}. The difference in the water permeation rates measured by two different methods is attributed to the presence of

a concentration polarization of DB71 on the membrane surface which can reduce the water flux through the membrane. Since this difference is not significant, we used the diffusion method to prevent any potential crack formation of the nm thin selective layer during the ion exclusion test.

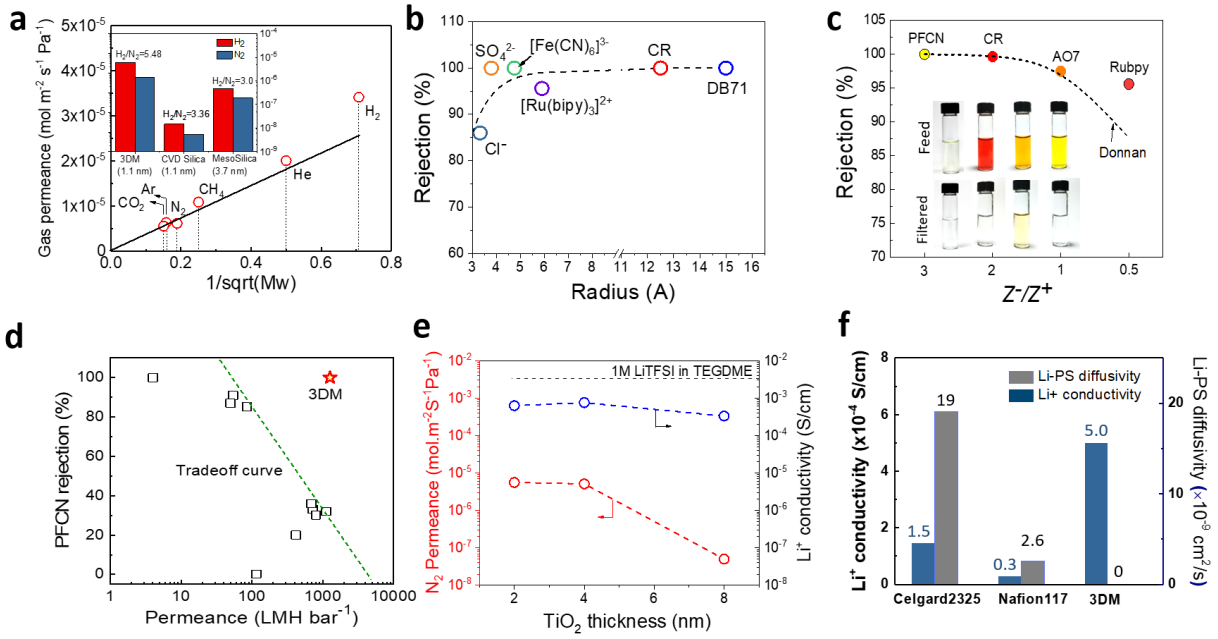

Figure 42. Separation properties. (**a**) Gas permeance as a function of the inverse square root of molecule weight. Inset shows H_2/N_2 selectivity (on the top of bar graph) and H_2 permeance (right y-axis) of the 3DM compared to 1.1-nm-pore size CVD microporous silica membrane[161] and 3.7-nm-pore size mesoporous silica membrane[163]. (**b**) Experimental ion and dye rejection ratio of a 4-nm-thin 3DM as a function of the molecule's hydrated radius. (**c**) Rejection ratio of ions with different valences and estimation from the Donnan exclusion model. (**d**) Comparison of water permeance and PFCN separation performance of the 3DM with other state-of-the-art membranes. Detailed information on other high flux membranes is available in the Appendix. (**e**) N_2 permeance and Li^+ conductivity of 3DMs with varied TiO_2 thickness. (**f**) Li^+ conductivity and Li-PS diffusivity values of Celgard 2325, Nafion 117, and 3DM. Li-PS diffusivity was evaluated by using UV-vis spectroscopy.

We evaluated the ionic separation properties of our 3DM through filtration experiments using different types of dyes and ions. **Figure. 42b** and Table 12 show the molecular sieving properties of the 4-nm-thin 3DM for NaCl, $MgSO_4$, potassium ferricyanide (PFCN), ruthenium-tris(2,2'-bipyridyl)dichloride (Rubypy), Direct Blue 71 (DB71), and Congo red (CR). The 3DM demonstrated its high rejection performance, > 90%, for the ions with hydrated radii larger than 3.7 Å. NaCl rejection (86%) is lower than $MgSO_4$ (~100%) which can be observed in many other membranes[165-167] . From the BET measurement, the average pore size on the ALD layer (1.1 nm) is smaller than the molecular dimension of DB71 and CR, implying that the higher rejection rate for these molecules could be attributed to the size exclusion effect[168]. However,

the 3DM also exhibited a high rejection rate of ~100% for PFCN and $MgSO_4$, although their hydrated diameters are smaller than the pore size on the ALD layer, while slightly lower rejection rates of 95.63% was observed for Rubypy.

Table 12. Separation performance and Donnan prediction of 3D-nm-thick membrane for charged species.

Molecules/ions	Feed Concentration (mM)	Hydrated diameter, nm	Molecular Dimension, nm	Rejection (Experiment)	Rejection (Donnan)	Ion Valence	Ion Permeability (cm^2/min)
DB71 ($C_{40}H_{28}N_7NaO_{13}S_4$)	0.1	N/A	3 x 1.5 x 1	**~100%**	**100%**	-4	N/A
$[Fe(CN)_6]^{3-}$	0.5	0.95	0.9 x 0.9	**99.65%**	**99.99%**	-3	3.606E-10
Congo Red ($C_{32}H_{22}N_6Na_2O_6S_2$)	0.1	N/A	2.5 x 0.7	**~100%**	**99.99%**	-2	N/A
SO_4^{2-}	0.1	0.758	0.15 (radius)	**~100%**	**98.81%**	-2	N/A
Acid Orange 7 ($C_{16}H_{11}N_2NaO_4S$)	0.1	N/A	0.73 x 1.36 x 0.23	**97.5%**	**99.40%**	-1	1.462E-09
$[Ru(bpy)_3]^{2+}$	0.1	1.180	0.53 (radius)	**95.63%**	**92.26%**	+2	4.625E-09

To investigate charge-based ion selectivity of the 3DM, we first measured zeta potential and Appendix Fig. A11 shows an iso-electrical point (IEP) around pH 4, suggesting that the membrane surface is negatively charged at pH=7. The estimated surface charge density is 8.389×10^{-3} C/m^2 which is close to the value reported from literature[169]. Due to the electrostatic interactions, the Donnan potential on the membrane/solution interface tends to exclude the co-ions, which gives higher rejection for the negatively charged ions[170]. The estimated Debye length (λ_D) in the presence of 0.1 mM PFCN is 12.4 nm, greater than the micropore size of the 3DM. Therefore, the high rejection rate for PFCN seems to be mainly due to the electrostatic repulsion given by the negative surface charge of the 3DM, which is similar to the observation in the sub-2 nm carbon nanotube pores[170]. Another important consequence of the Donnan exclusion is the dependence of the rejection rate on the ratio of the valency of anion (z-) and cation (z+), as suggested by Equation S1 in SI. This is supported by the fact that the 3DM shows a slightly lower rejection rate for AO7 and Rubypy, which has the z-/z+ ratio of 1 and 0.5 respectively, lower than that of other negative charged molecules: PFCN (3) and CR (2). Therefore, we could conclude that the high rejection rates of the 3DM against charged species is a combined effect of charge and size of molecules.

In **Figure. 42d**, Appendix Fig. A12, and Table 12, we compare the PFCN separation performance of the 3DM with other high flux membranes reported so far, including a nanostrand-channeled graphene oxide (NSC-GO) membranes (691 L m^{-2} h^{-1} bar^{-1}), and a WS_2 nanosheet membrane (750 L m^{-2} h^{-1} bar^{-1}) [171, 172]. It is important to note that the NSC-GO membrane and WS_2 membrane showed only 36 % and 33 % rejections for PFCN ions, comparing to ~100% of 3DM. The 3D membrane with very high ion rejection and water permeance of 1,260 L m^{-2} h^{-1} bar^{-1} (calculated based on footprint-based surface area) outperforms all other high flux membranes, and its separation performance is far beyond the tradeoff curve for PFCN rejection and water permeance.

Our 3DMs could also be used for Li-O_2 and Li-S battery applications. Different from the N_2 permeance, the Li^+ conductivity is insensitive to the ALD TiO_2 thickness (**Figure. 42e**). The high Li^+ transport through 3DM is attributed to the smaller ionic radius (76 pm) compared to the micropores in TiO_2 layer. Besides, the 3DM completely blocks polysulfide (S_8^{2-}), while it provides high Li^+ conductivity. The Li^+ conductivity over the polysulfide blocking ability of our 3DM is infinite comparing to Celgard 2325 and Nafion 117 (**Figure. 42f**). Therefore, potential 3DMs can be developed to only allow Li^+ transport while blocking larger molecules such as O_2 (M_w close to N_2) or lithium polysulfides (Li_2S_n, n=2-8), which is critical to solving the O_2 crossover or the Li_2S_n shuttling induced degradation issues in Li-O_2 and Li-sulfur batteries[173].

We attribute the remarkable selectivity and permeance of our 3DM to its unique bicontinuous porous structures (**Figure. 41a**). The interconnected channels provide continuous pathways for fast mass transport towards the membrane surface throughout the volume of our 3DM. Meanwhile, the thin TiO_2 ALD selective layer has high micropore density and small pore size functions as the ideal barrier to separate small molecules or ions by size with very low transport resistance (R_{micro}) compared to resistance of mesopores (R_{meso}) as described in Appendix Table A5. In contrast, as shown in **Figure 43a**, conventional synthetic membrane systems have long-range mass transport pathways as well as low membrane effective surface area (ESA). The 200-μm-thick 3DM presents ESA (600,000%) higher than biological membranes (645%)[174, 175] and conventional synthetic membranes (~100%)[176-178] by three orders of magnitude, which explains the experimentally observed ultrafast mass transport of our 3DMs. **Figure. 43b** provides insightful information on the relationship between structure and separation performance of the 3DM, biological membrane (glomerulus filtration[179]), the synthetic dialysis (Curophan and An-69[176, 177]), and thin-film composite forward osmosis membranes (TFC-FO[178]). We used direct blue 71 (DB71, 3 ×1.5 × 1 nm of molecular dimension[180]) for the 3DM to properly compare the separation performances of other membranes from literatures that used Red K-2BP (~1.8 nm of diameter calculated using Chem3D) or inulin (~2.8 nm of diameter[179]). Both in the synthetic and biological membranes, membranes with higher ESA or $1/T_{SL}$ show higher water permeance because membrane permeance is directly proportional to its surface

area and inversely proportional to its thickness. Water permeance of glomerulus filtration in kidney is higher than the commercial dialysis membranes and TFC-FO by several orders of magnitude while it is not able to exclude inulin due to its large MWCO ranges of 30-50 kDa (4.1-4.8 nm of stokes diameter). The TFC-FO shows high rejection value for the Red K-2BP, however, its permeance is the smallest due to its nonporous dense selective layer compared to other synthetic porous membranes. Although the pore size of the 3DM is around 1.1 nm, it outperforms all compared membranes in permeance as well as rejection due to its huge surface area, nm-thin membrane wall, and combination of molecular sieving and charge-based exclusion. Thus, this unique structural and surface properties provide our 3D nm-thin bio-mimic membranes with both excellent ion rejection rates and ultra-fast water transport properties, which can offer a figure of merit for membrane performance for various practical applications.

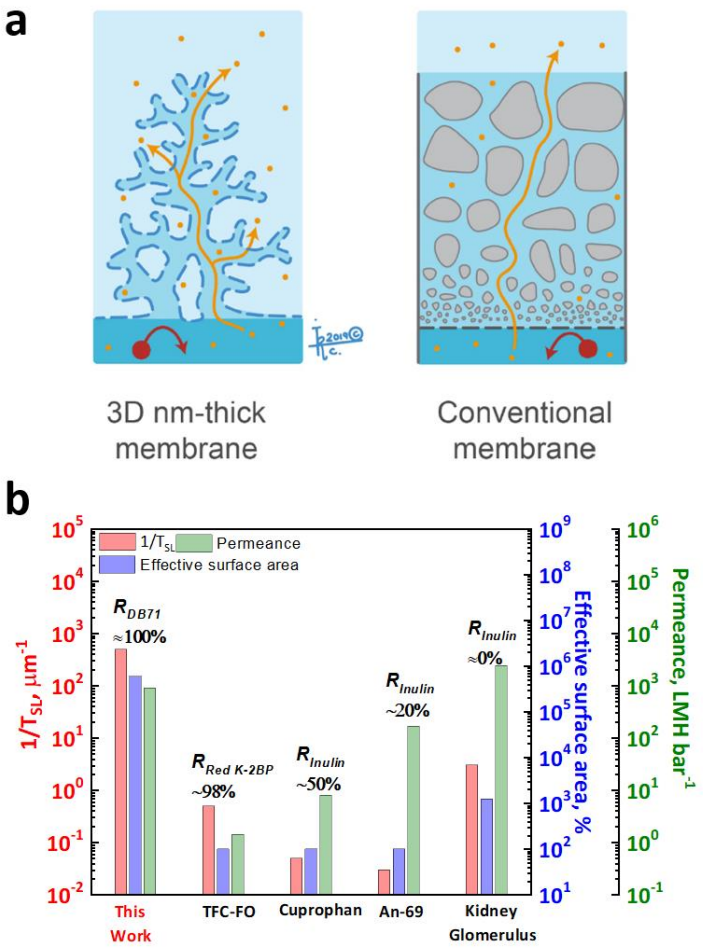

Figure 43. Membrane morphology and performance relationship. (**a**) Schematics of selective transport of molecules and ions through biomimetic structure of the 3DM (left), and conventional synthetic membrane

pore structure (right). (**b**) Comparison of reported value for active surface area and reciprocal of selective layer thickness ($1/T_{SL}$) of biological membrane, commercial and lab-fabricated osmosis membranes to those obtained in this study.

6.3 Summary

In conclusion, we developed self-supportive biomimetic 3D membranes with orders of magnitude larger surface area than the footprint area and nanometer-thin separating layer. High mass transport rates and excellent selectivity were observed in gas, water, and ion permeance experiments. The 3DM also exhibited promise in applications in energy storage area, for instance, Li-S and Li-O_2 batteries. The current approach using nanoporous gold as a template suffers from high cost and large transport resistance from tortuous channels. By adoption of machine learning based architectural optimizations and additive manufacturing techniques, the mechanical and transport properties of 3DMs can be further improved and the cost can be reduced. Different coating materials such as ductile metals and elastic polymers can also be developed to replace metal oxides to meet specific servicing environment. It can be envisioned that these 3DMs will have broad applications in gas separation, water purification, battery technologies, catalysts, and many others.

VII. CONCLUDING REMARKS

Work presented in this dissertation focused on developing nano-engineered membranes to overcome the trade-off limitation between ion selectivity and permeability, as well as establishing a fundamental understanding on the correlation between membrane structure and its ion transport/electrochemical performance. The research began with the polymer ion exchange membranes (IEMs) built on rigid biphenyl/terphenyl backbone and decorated with different side chains (**Chapter 3**). The ion transport and battery performance testing results suggested that these low-cost aromatic polymer membranes could simultaneously possess a high proton conductivity and ion selectivity, and thus overcome the conventional proton conductivity-selectivity trade-off. SAXS and DFT calculation studies further revealed that the narrowly distributed aqueous ionic domain width and the strong interaction between IEMs and vanadium ion complexes through π---H or π---F hydrogen bonding are the key contributing factors to improve ion selectivity.

Results from **Chapter 3** suggest an effective path towards the development of high-performance pure polymeric IEM. However, the use of single-component membranes cannot fully address all existing issues and the membranes are still limited for practical application. Therefore, in **Chapter 4**, we have explored feasibility to further enhance the membrane performance by introducing a nano-patterned selective layer into the pure polymer IEMs. In this study, we firstly developed a surface nano-engineered hybrid membrane with tunable ion selectivity by coating the IEM with a thin nano-cracked surface layer. Our results have shown that the nano-crack selective layer setting on the membrane surface is effective to hinder the transport of vanadium ions and therefore mitigating the cross-over flow, while it has less effect on proton conductivity resulting in enhanced ion selectivity. These results suggested that the performance of the conventional polymeric PEM can be improved with the additional nano-engineered surface layers. Encouraged by these results, we further developed a 2D-graphene coated hybrid IEM for VRFB application. From the ion transport study on the single-layer graphene transferred to silicon device and pore-filled IEM substrates, it was found that the 2D-graphene layer could effectively attenuate the vanadium species crossover. However, due to the presence of defects on the graphene and the loss of graphene layers during the flow battery test, the potential of using 2D selective layers on improving the membrane performances has not been fully exploited. Thus, the future work on this study will be focused on minimizing the adverse effect of defects on the selective ion transport of membranes.

The studies in **Chapter 3** and **Chapter 4** mainly focus on the membrane development and ion transport studies for vanadium redox flow batteries (VRFBs). However, VRFB systems have been historically limited

by their low energy density and the high cost of raw materials. The wide market penetration for the electrochemical storage systems still relies on the development of higher energy density batteries systems and corresponding membrane technologies. Thus, in **Chapter 5**, we applied a nano-engineered membrane to a non-aqueous lithium-polysulfide flow battery (Li-PS RFB) which possesses higher energy density and lower cost compared to the VRFBs. To address the detrimental shuttling effect caused by the polysulfide crossover in Li-PS RFBs, we have developed a multifunctional bi-layered membrane which has a high selectivity of lithium over polysulfide ions. This membrane is comprised of an ion exchange resin infiltrated carbon nanotube (CNT) layer and a boron nitride nanotube (BNNT) layer. The biphenyl polymer (BPSA), which has also been used in **Chapter 3**, was employed as the main component to build the membrane because of its excellent chemical stability and Li^+/PS^- selectivity. With the addition of nanotube interlayers, this bi-layered membrane exhibits remarkable stability and higher ion selectivity. The Li-PS RFB with the bilayer membrane exhibited sustainably enhanced cycling stability and a lower capacity-fading rate. The results from **Chapter 5** have proven that the nano-engineered IEMs are also applicable to the non-aqueous electrochemical systems.

The membrane structures presented in **Chapter 3-5** are depending on a two-dimensional geometry, which has limited transport area. In order to explore the ultimate membrane structure, in **Chapter 6**, we presented our efforts on making a three-dimensional (3D) membrane which consists of orders of magnitude larger surface area than the footprint area and nanometer-thin separating layer. The interconnected channels in this membrane provide continuous pathways for fast mass transport while the large surface and the thin selective layer diminish the transport resistance. As a result, this 3D membrane exhibited fast mass transport rates and excellent selectivity in gas, water, and ion permeance experiments. These great features of this nano-engineered 3D membrane make it a promising membrane material for applications in the energy storage area.

The results and conclusions presented in this dissertation have elucidated the ion transport mechanism in the nano-engineered membranes and provided a design principle to develop IEMs with high ion selectivity and permeability. Although the targeted application area of this research mainly focusses on redox flow batteries, its outcome would be applicable to other related areas.

APPENDICES

APPENDIX A. PERMISSION FROM COPYRIGHT HOLDERS

Chapter 3 and 4 contain materials from two papers published on Journal of Membrane Science (publisher Elsevier). According to the policy of publisher, permission is not required if the article is used for the author's dissertation/thesis:

Copyright Clearance Center RightsLink

Home | Help | Email Support | Sign in | Create Account

Selective ion transport for a vanadium redox flow battery (VRFB) in nano-crack regulated proton exchange membranes

Author: Tongshuai Wang,Sun Ju Moon,Doo-Sung Hwang,Hyunjin Park,Jannice Lee,Seungju Kim,Young Moo Lee,Sangil Kim
Publication: Journal of Membrane Science
Publisher: Elsevier
Date: 1 August 2019

© 2019 Elsevier B.V. All rights reserved.

Please note that, as the author of this Elsevier article, you retain the right to include it in a thesis or dissertation, provided it is not published commercially. Permission is not required, but please ensure that you reference the journal as the original source. For more information on this and on your other retained rights, please visit: https://www.elsevier.com/about/our-business/policies/copyright#Author-rights

BACK | CLOSE WINDOW

Poly(terphenylene) anion exchange membranes with high conductivity and low vanadium permeability for vanadium redox flow batteries (VRFBs)

Author: Tongshuai Wang,Jong Yeob Jeon,Junyoung Han,Jae Heon Kim,Chulsung Bae,Sangil Kim
Publication: Journal of Membrane Science
Publisher: Elsevier
Date: 15 March 2020

© 2019 Elsevier B.V. All rights reserved.

Please note that, as the author of this Elsevier article, you retain the right to include it in a thesis or dissertation, provided it is not published commercially. Permission is not required, but please ensure that you reference the journal as the original source. For more information on this and on your other retained rights, please visit: https://www.elsevier.com/about/our-business/policies/copyright#Author-rights

BACK | CLOSE WINDOW

Chapter 6 contain materials from a paper published on Material Horizons (publisher The Royal Society of Chemistry). According to the policy of publisher: “Authors contributing to RSC publications (journal articles, books or book chapters) do not need to formally request permission to reproduce material contained in this article provided that the correct acknowledgement is given with the reproduced material.”

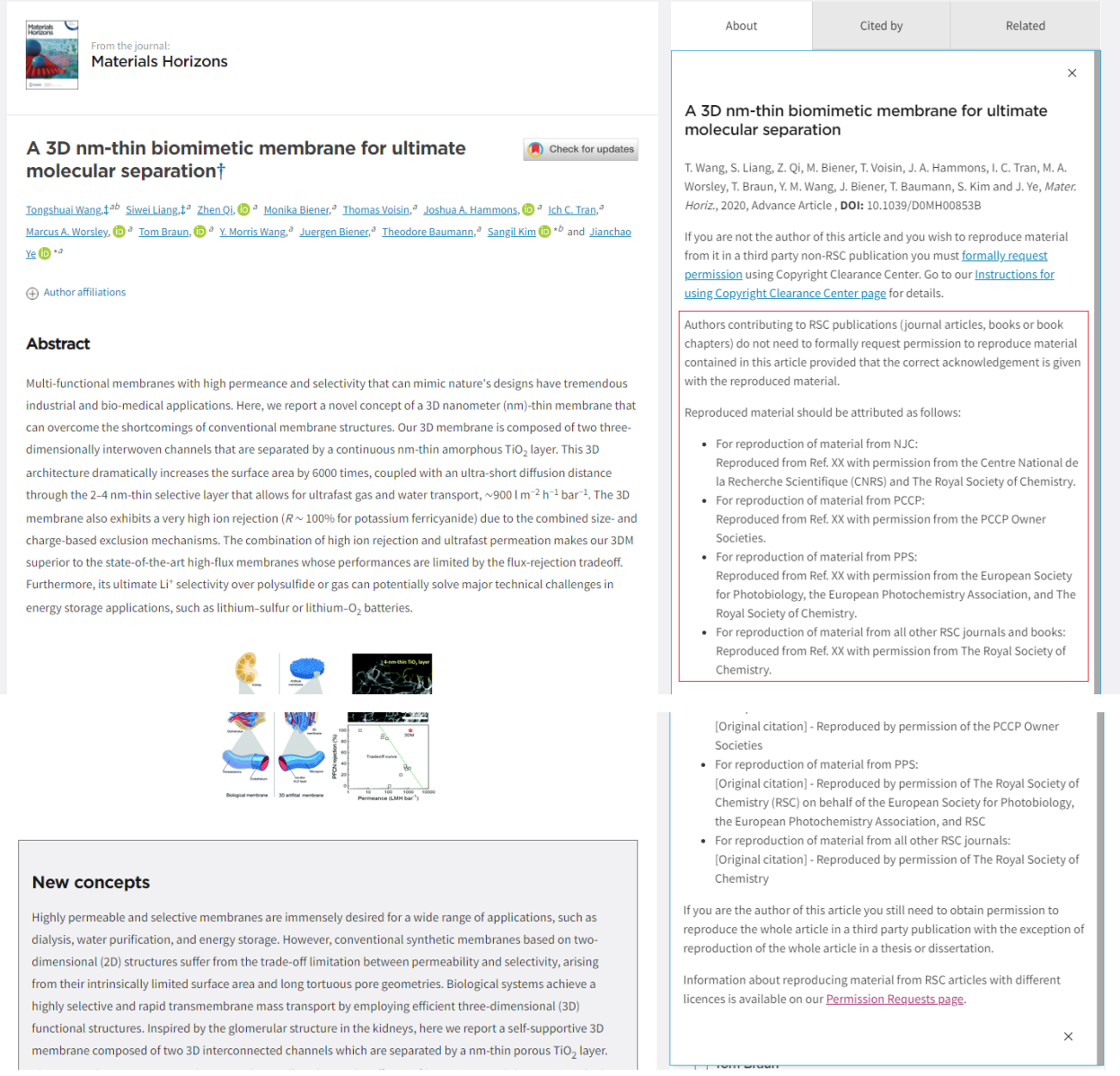

From the journal:
Materials Horizons

A 3D nm-thin biomimetic membrane for ultimate molecular separation†

Check for updates

Tongshuai Wang,‡[ab] Siwei Liang,‡[a] Zhen Qi,[a] Monika Biener,[a] Thomas Voisin,[a] Joshua A. Hammons,[a] Ich C. Tran,[a] Marcus A. Worsley,[a] Tom Braun,[a] Y. Morris Wang,[a] Juergen Biener,[a] Theodore Baumann,[a] Sangil Kim*[b] and Jianchao Ye*[a]

Author affiliations

Abstract

Multi-functional membranes with high permeance and selectivity that can mimic nature's designs have tremendous industrial and bio-medical applications. Here, we report a novel concept of a 3D nanometer (nm)-thin membrane that can overcome the shortcomings of conventional membrane structures. Our 3D membrane is composed of two three-dimensionally interwoven channels that are separated by a continuous nm-thin amorphous TiO_2 layer. This 3D architecture dramatically increases the surface area by 6000 times, coupled with an ultra-short diffusion distance through the 2–4 nm-thin selective layer that allows for ultrafast gas and water transport, ~900 l m^{-2} h^{-1} bar^{-1}. The 3D membrane also exhibits a very high ion rejection ($R \sim 100\%$ for potassium ferricyanide) due to the combined size- and charge-based exclusion mechanisms. The combination of high ion rejection and ultrafast permeation makes our 3DM superior to the state-of-the-art high-flux membranes whose performances are limited by the flux-rejection tradeoff. Furthermore, its ultimate Li^+ selectivity over polysulfide or gas can potentially solve major technical challenges in energy storage applications, such as lithium-sulfur or lithium-O_2 batteries.

New concepts

Highly permeable and selective membranes are immensely desired for a wide range of applications, such as dialysis, water purification, and energy storage. However, conventional synthetic membranes based on two-dimensional (2D) structures suffer from the trade-off limitation between permeability and selectivity, arising from their intrinsically limited surface area and long tortuous pore geometries. Biological systems achieve a highly selective and rapid transmembrane mass transport by employing efficient three-dimensional (3D) functional structures. Inspired by the glomerular structure in the kidneys, here we report a self-supportive 3D membrane composed of two 3D interconnected channels which are separated by a nm-thin porous TiO_2 layer.

About | Cited by | Related

A 3D nm-thin biomimetic membrane for ultimate molecular separation

T. Wang, S. Liang, Z. Qi, M. Biener, T. Voisin, J. A. Hammons, I. C. Tran, M. A. Worsley, T. Braun, Y. M. Wang, J. Biener, T. Baumann, S. Kim and J. Ye, *Mater. Horiz.*, 2020, Advance Article , **DOI:** 10.1039/D0MH00853B

If you are not the author of this article and you wish to reproduce material from it in a third party non-RSC publication you must formally request permission using Copyright Clearance Center. Go to our Instructions for using Copyright Clearance Center page for details.

Authors contributing to RSC publications (journal articles, books or book chapters) do not need to formally request permission to reproduce material contained in this article provided that the correct acknowledgement is given with the reproduced material.

Reproduced material should be attributed as follows:

- For reproduction of material from NJC:
  Reproduced from Ref. XX with permission from the Centre National de la Recherche Scientifique (CNRS) and The Royal Society of Chemistry.
- For reproduction of material from PCCP:
  Reproduced from Ref. XX with permission from the PCCP Owner Societies.
- For reproduction of material from PPS:
  Reproduced from Ref. XX with permission from the European Society for Photobiology, the European Photochemistry Association, and The Royal Society of Chemistry.
- For reproduction of material from all other RSC journals and books:
  Reproduced from Ref. XX with permission from The Royal Society of Chemistry.

[Original citation] - Reproduced by permission of the PCCP Owner Societies

- For reproduction of material from PPS:
  [Original citation] - Reproduced by permission of The Royal Society of Chemistry (RSC) on behalf of the European Society for Photobiology, the European Photochemistry Association, and RSC
- For reproduction of material from all other RSC journals:
  [Original citation] - Reproduced by permission of The Royal Society of Chemistry

If you are the author of this article you still need to obtain permission to reproduce the whole article in a third party publication with the exception of reproduction of the whole article in a thesis or dissertation.

Information about reproducing material from RSC articles with different licences is available on our Permission Requests page.

APPENDIX B. TABLES

Table A1. Comparison of VO^{2+} permeability and resistivity of membranes reported from literatures.

Samples	Type of membrane	VO^{2+} Permeability ($\times 10^{-7}$ cm^2/min)	Resistivity (Ω.cm)	Ref.
S-Radel	PEM	2.1	46.79	[181]
SPEEK	PEM	11-12	59-61	[182]
SPTKK	PEM	~1.8	73.5	[125]
SPTK	PEM	~0.7	95.2	[125]
SPAES	PEM	~1.6	~70-80	[183]
SPBI30	PEM	0.17	86	[184]
BPSH60	PEM	210	8.3	[121]
N115	PEM	33	39.4	[185]
XL100	PEM	25.7	86.1	[186]
SPFEK	PEM	9.85	58.82	[187]
Nafion117	PEM	37	16.9	[7]
Nafion212	PEM	41	13.5	[121]
BP-ArF4	PEM	10	17.36	This work
QA-PFE	AEM	~0	~200	[114]
QPPAE-2/1	AEM	~0	154	[120]
QPPP-2	AEM	0.09	400	[188]
QPEK-C-TMA+	AEM	4.8	179	[189]
C6QPSF	AEM	0.5	63	[190]
PAEK-API	AEM	1.31	250	[191]
QDAPP	AEM	1.8	108	[192]
PSF-TMA	AEM	0.26	250	[193]
PyPPEKK	AEM	0.684	143	[194]

Table A2. Comparison of VRFB efficiencies, self-discharge time, and capacity retention/decay rate with PEMs and AEMs reported from literatures.

Samples	Type of membrane	CE (%)	VE (%)	EE (%)	Current density (mA/cm^2)	Self-discharge time (hour)	Capacity retention/Cycle #	Capacity decay rate (per cycle)/Current density (mA/cm^2)	Thickness (μm)	Vanadium sulfate/H_2SO_4 concentration	Ref.
Nafion 115	PEM	91.7	92.3	84.7	50	80	N/A	N/A	127	1.5M/3M	[195]
Nafion 212	PEM	92	86	79	80	40	N/A	N/A	60	1.5M/3M	[196]
SPPEK	PEM	98.8	75.5	74.6	60	N/A	N/A	N/A	20	1.5M/3M	[181]
SPEEK40	PEM	98.5	88.8	87.5	50	170	N/A	N/A	90	1.5M/3M	[195]
SPEEK50	PEM	97.3	86.3	84.0	50	N/A	N/A	N/A	85	1.5M/3M	[195]
SPEEK60	PEM	96.1	87.6	84.2	50	N/A	N/A	N/A	90	1.5M/3M	[195]
S-PAEK-40	PEM	89.5	92.2	82.6	20	N/A	~60%/100	0.4%/20	172	1M/2M	[197]
Nafion 117	PEM	90	94	84.6	40	30	~50%/200	0.25/80	175	1.5M/2M	[91]
SPSF-62	PEM	94.9	94.0	89.2	50	29	N/A	N/A	76	1.5M/3M	[198]
SPI-50	PEM	96	93.8	90.1	40	110	78.2%/100	0.218/160	71	1.5M/2M	[199]
SPBI-30	PEM	~100 ~100	~85 ~88	~85 ~88	80 60	384	54.95%/500	0.09%/100	35	1.5M/3M	[184]
BP-ArF4	PEM	99.21 ±0.17 98.63 ±0.23 97.34 ±0.16	89.54 ±1.98 93.2± 0.93 96.42 ±0.51	88.83 ±2.12 91.93 ±1.14 93.85 ±0.65	80 60 40	209.5	84%/200	0.08%/100	88	1.6M/4M	This work

		99.21 ±0.17	89.54 ±1.98	88.83 ±2.12	20						
QA-PFE	AEM	~100	~78	~78	40	N/A	N/A	N/A	~50	1M/2.5M	[114]
QPPAE-2/1	AEM	99.3	88.9	88.4	50	N/A	70%/500	0.08%/50	N/A	1.65M/3M	[120]
AIEM	AEM	95.6	78.5	75.1	40	~300	N/A	N/A	43	1.5M/2.5M	[200]
QPPP-2	AEM	~99	~87	~87	80	N/A	92%/30	0.26%/80	~35	1.65M/3M	[188]
QPEK-C-TMA+	AEM	~99	~81	~80	30	N/A	N/A	N/A	40	1.5M/3M	[189]
QAPPEK	AEM	98.4	83.8	82.5	40	N/A	N/A	N/A	~40	1.5M/3M	[201]
DF-a2	AEM	98.5	84.6	83.3	50	35	N/A	N/A	~300	1.5M/3M	[202]
QS-AIEM	AEM	98	91.5	89.7	50	N/A	70%/80	0.375%/N/A	~40	1.5M/3M	[190]
PAEK-API	AEM	96.4	86.5	83.4	60	N/A	84%/100	0.16%/40	~130	1.5M/3M	[191]
QDAPP	AEM	99	85	85	200	N/A	94%/20	0.3%/N/A	N/A	1.7M/5M	[192]
PyPPEKK	AEM	98.4	90.3	88.9	40	N/A	N/A	N/A	45	1.5M/3M	[194]

Table A3. Separation performance and Donnan prediction of 3D nm-thin membrane for charged species.

Molecules/ions	Feed Concentration (mM)	Hydrated diameter (nm)	Molecular Dimension (nm)	Rejection (Experiment)	Rejection (Donnan)	z^-/z^+
DB71 ($C_{40}H_{28}N_7NaO_{13}S_4$)	0.1	N/A	3 x 1.5 x 1	**~100%**	**100%**	4
$[Fe(CN)_6]^{3-}$	0.1	0.95	0.9 x 0.9	**~100%**	**99.99%**	3
Congo Red ($C_{32}H_{22}N_6Na_2O_6S_2$)	0.1	N/A	2.5 x 0.7	**~100%**	**99.99%**	2
$MgSO_4$	0.1	0.85 (Mg^{2+})	N/A	**~100%**	**98.81%**	1
Acid Orange 7 ($C_{16}H_{11}N_2NaO_4S$)	0.1	N/A	0.73 x 1.36 x 0.23	**97.5%**	**99.40%**	1
NaCl	0.1	0.54 (Na^+)	N/A	**86.0%**	**99.40%**	1
$[Ru(bpy)_3]^{2+}$	0.1	1.180	0.53 (radius)	**95.63%**	**92.26%**	0.5

Table A4. Comparison of the separation performance of the 3DM with other high flux membranes and commercial NF membranes.

Membrane	Rejection	Salt/Dye	Permeance (LMH/bar)	Reference
PSS/PDADMAC (NF)	95%	$MgSO_4$	13.9	[203]
PEI/TMC (NF)	~78%	$MgSO_4$	9.5	[165]
DETA/TMC (NF)	~83%	$MgSO_4$	~4	[165]
GOQD NF	~87.16%	$MgSO_4$	18.4	[204]
GO/PA-PES TFN	~83.2%	$MgSO_4$	4.8	[205]
Dow NF270	99.3%	$MgSO_4$	13.2	[166]
GO framework membranes	~30 %	$MgSO_4$	~17	[166]
GNM	82.8 %	$MgSO_4$	4.76	[206]
G-CNT	~40%	$MgSO_4$	11.3	[206]
Dow/Filmtec BW30(RO)	99.7%	$MgSO_4$	~3	[207]
Dow/Filmtec XLE (RO)	99.2%	$MgSO_4$	7.4	[207]
PA-TiO_2	95%	$MgSO_4$	9.1	[208]
ZIF-8/GO	77%	$MgSO_4$	~4	[209]
3DM	~100%	$MgSO_4$	~900	This work
WS_2 Nanosheet Membranes	33 %	$K_3[Fe(CN)_6]$	704-747	[172]
NSC-GO	36 %	$K_3[Fe(CN)_6]$	691	[171]
VACNT	91 %	$K_3[Fe(CN)_6]$	54	[170]
MXene	32 %	$K_3[Fe(CN)_6]$	1120	[210]
PES	0.2 %	$K_3[Fe(CN)_6]$	115	[210]
SWCNT-intercalated GO	30.1 %	$K_3[Fe(CN)_6]$	~800	[211]
HLGO	~100%	$K_3[Fe(CN)_6]$	~4	[212]
S-rGO-18	85.2%	$K_3[Fe(CN)_6]$	~ 85	[213]
Single-layer graphene	~87 %	$K_3[Fe(CN)_6]$	~50	[214]
PA/PTFE	20 %	$K_3[Fe(CN)_6]$	420	[215]
3DM	~100%	$K_3[Fe(CN)_6]$	892	This work

Table A5. Experimental and calculated gas flux and water permeance, total mass transfer resistance through mesoporous channels (R_{meso}) and micropores (R_{micro}).

	Experimental	**Calculated**	**Ratio (Exp/Cal)**	R_{meso} **(Pa·s/m^3)**	R_{micro} **(Pa·s/m^3)**
N_2 volumetric flux	4.53×10^{-8} m^3/s	6.66×10^{-8} m^3/s	0.68	6.74×10^{14}	3.19×10^{5}
He volumetric flux	1.11×10^{-7} m^3/s	1.85×10^{-7} m^3/s	0.60	2.54×10^{14}	1.21×10^{5}
Water permeance	891.90 LMH/Bar	722.69 LMH/Bar	1.23	5.88×10^{16}	2.97×10^{8}

Table A6. Dimensions and effective surface area (ESA) for the studied membranes. The sample projection area for kidney glomerulus is calculated from the reported mean glomerular volume by assuming a spherical geometry[216]. The glomerular actual area refers to the total surface area of capillaries inside a glomerulus[216]. Similar values were also found from other places [174, 217-220]. The sample projection areas for other commercial and lab-fabricated membranes are converted to 1 cm^2.

Membrane	Actual area (cm^2)	Projection area (cm^2)	Effective surface area (%)	Rejection (%) /Dye species or MWCO
NF270	~1	1	~100 %	99.3/$MgSO_4$
GO-Framework	~1	1	~100%	~31/$MgSO_4$
Biomax30	~1	1	~100 %	30 kDa
PVDF-Al_2O_3	~1	1	~100%	35 kDa
Single kidney glomerulus	3.8×10^{-3}	2.34×10^{-4}	1,624%	30-50 kDa
3DM	1800	0.3	600,000%	~100/$MgSO_4$

APPENDIX C. FIGURES

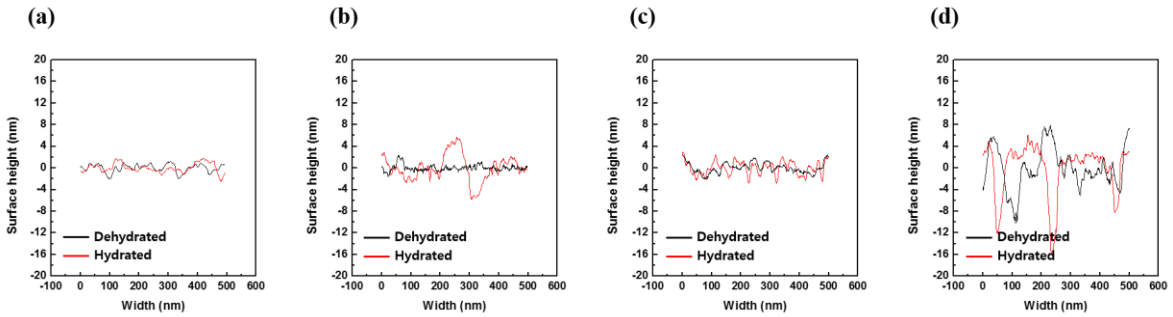

Figure A1. Depth profiles of nano-crack with two different humidification conditions. (a) BPSH60 (b) P-BPSH60 R5 (c) P-BPSH60 R7 (d) P-BPSH R10

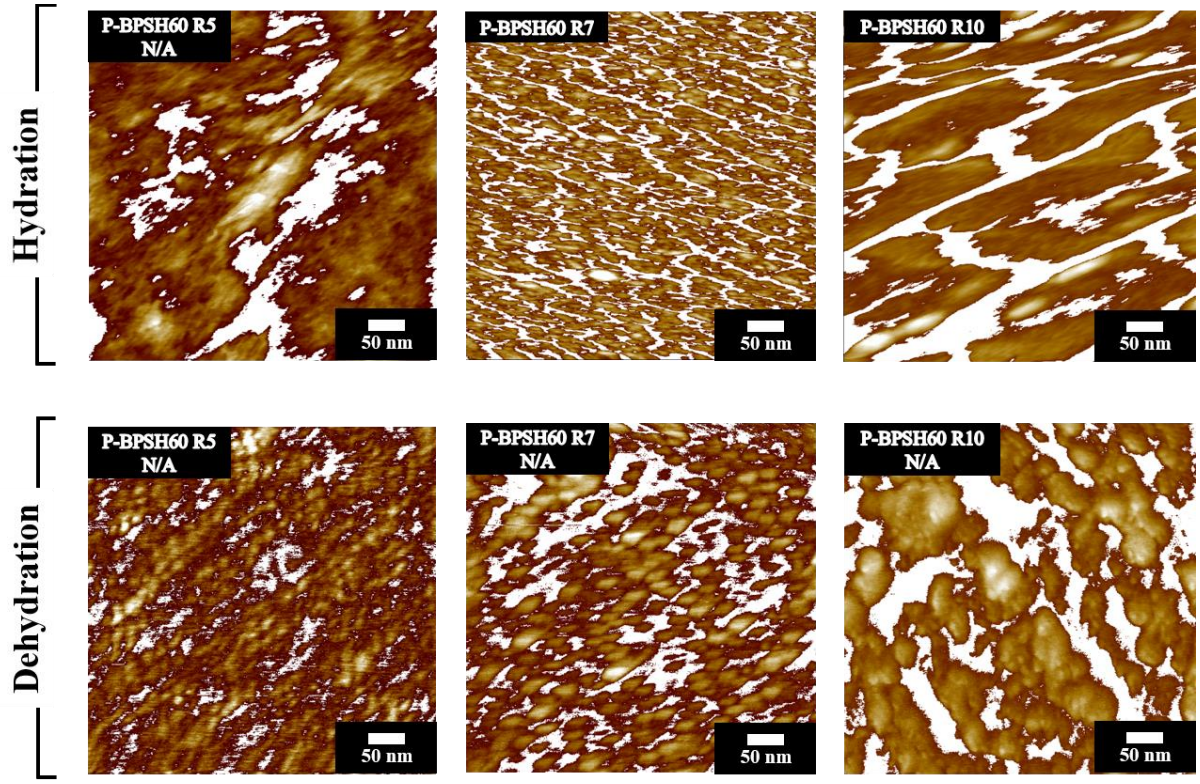

Figure A2. AFM images used to calculate the area ratio of the nano-cracks. White areas represent the nano-crack portion of each sample. The P-BPSH60 R5 membrane in hydration conditions and all dehydrated samples are marked with 'N/A' because the width of the cracks are too small to be recognized by the program.

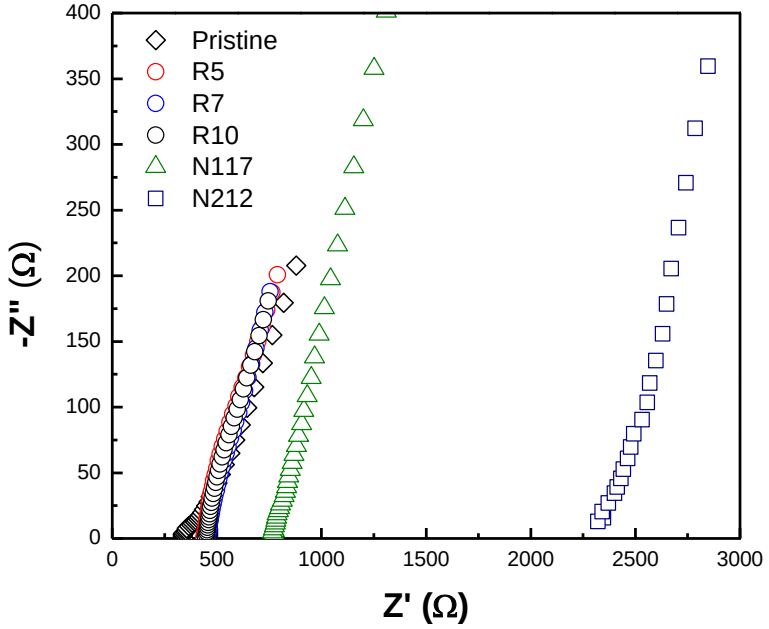

Figure A3. Nyquist plots for the conductivity tests for different membranes.

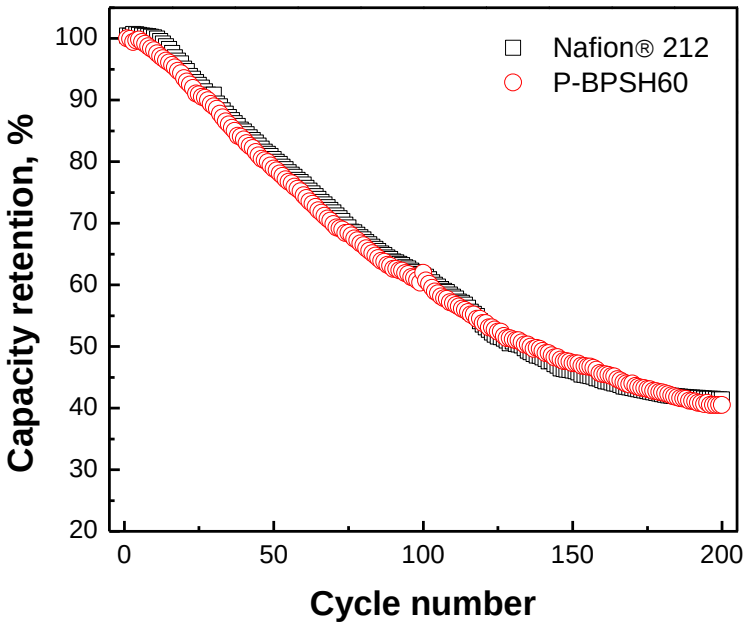

Figure A4. VRFB capacity retention during 200-cycle stability tests for P-BPSH60 and Nafion® 212 at 80 mA/cm^2 current density.

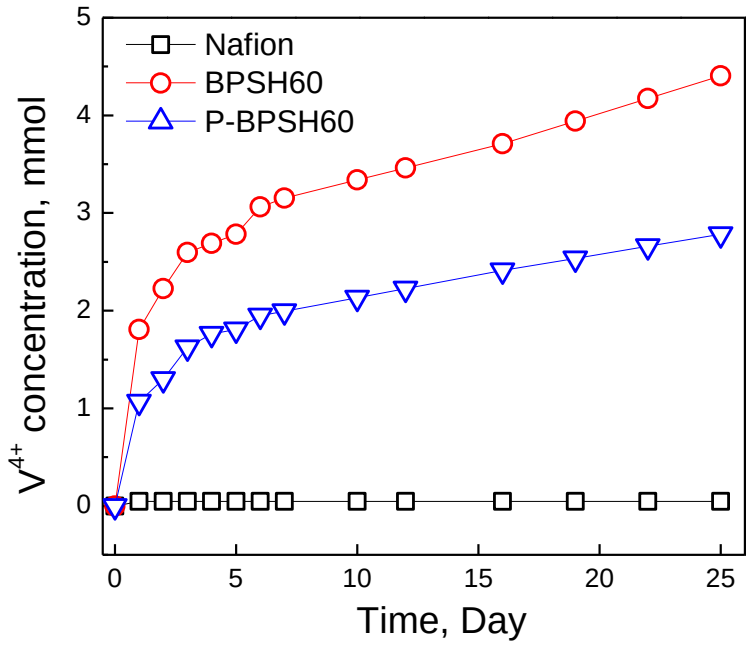

Figure A5. Increase of V^{4+} ions concentration with time of electrolyte (0.1 M V^{5+} in 4.0 M H_2SO_4) solutions containing BPSH60, P-BPSH60 and Nafion 117 membranes at room temperature.

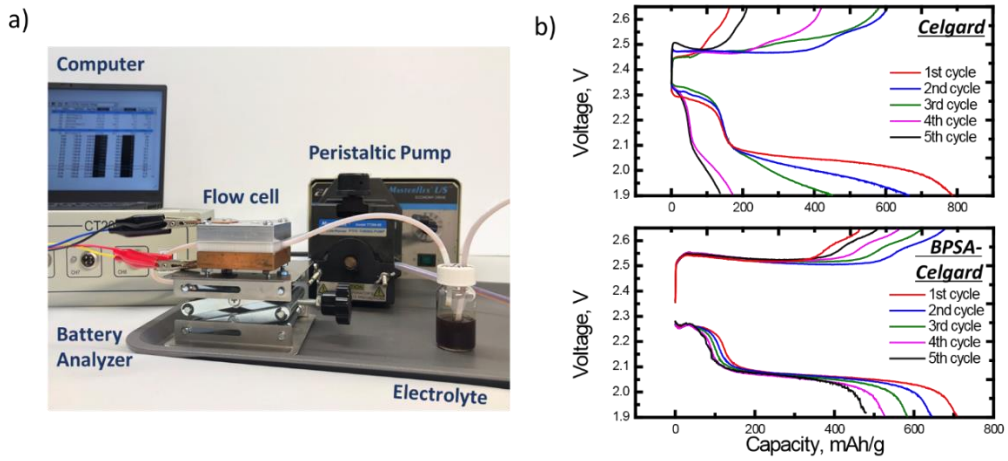

Figure A6. a. photo of Li-PS RFB cell. B. 1-5 cycle charging and discharging curve with Celgard and BPSA-coated celgards.

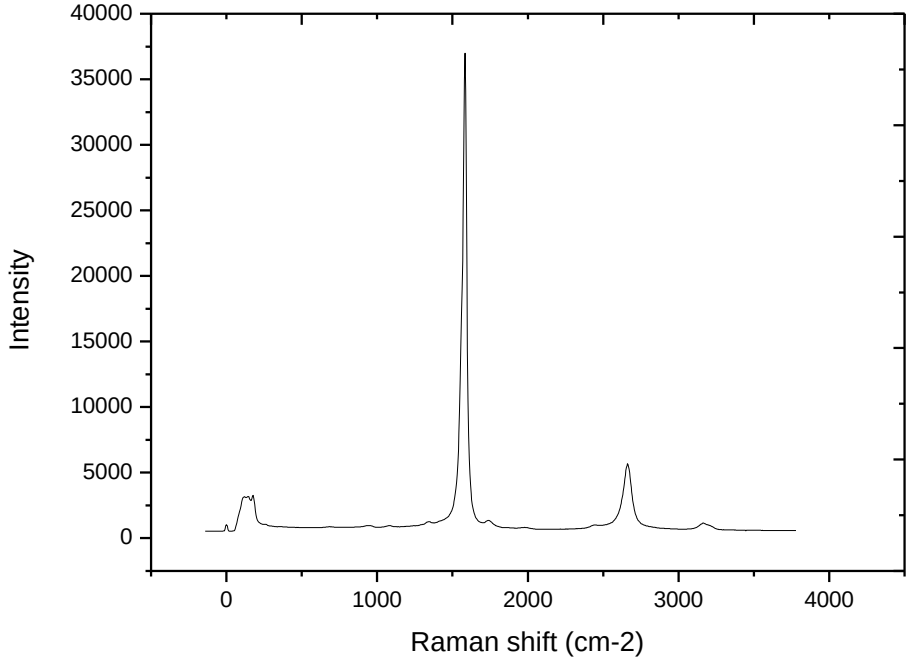

Figure A7. Raman spectrum for the CNT layer

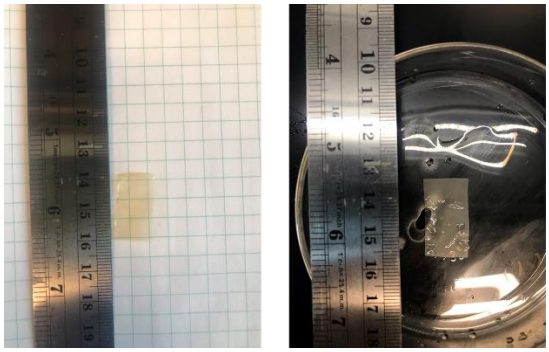

	Length	Area
Dry	2.3 cm	2.86 cm²
Wet	2.29 cm	2.61 cm²

Figure A8. Stability of membrane in DOL/DME (it is better to use bilayer membrane, it is dementially more stable)

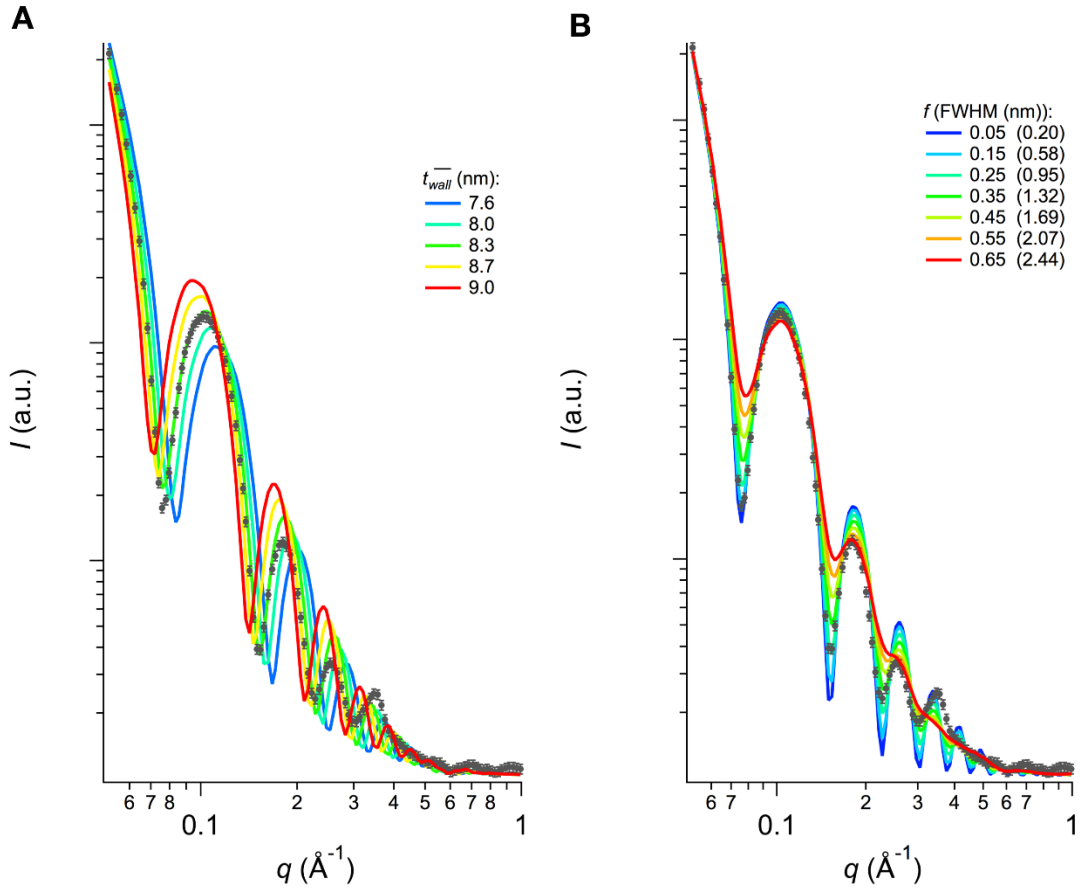

Figure A9. log-log plots of the SAXS data collected from the TiO_2 network (dark grey) with different values of $\overline{t_{wall}}$ (**a**) and *f* (**b**) to illustrate the strong sensitively of the SAXS modeling to the size distribution of wall thicknesses.

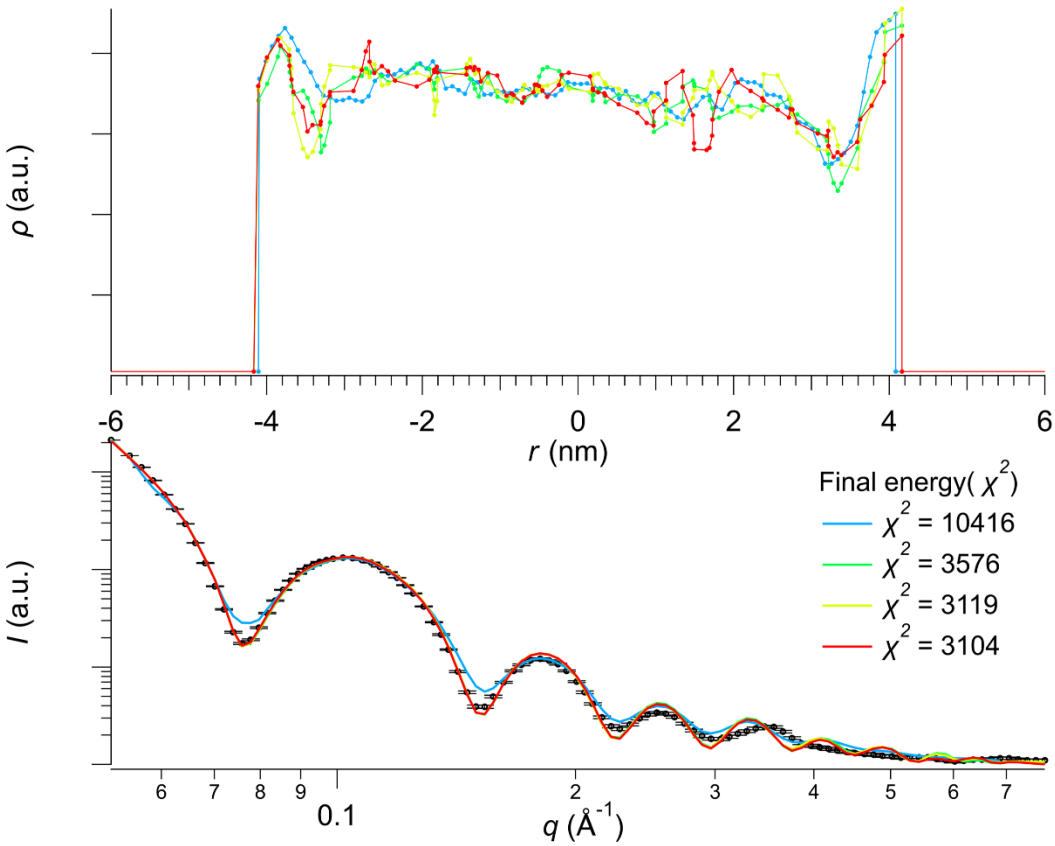

Figure A10. Simulated annealing results of the electron density through to the TiO_2 wall (top) obtained by simulated annealing with a starting temperature of 1000 (red and yellow lines) and 2000 (green) using $\overline{t_{wall}}$ and f of 8.3 nm and 0.25, respectively. A broader size distribution of (f = 0.35) was also used as an initial starting condition (blue) to determine whether the size polydispersity of $\overline{t_{wall}}$ had an effect on the wall heterogeneity found by simulated annealing. The resulting model fits are shown in the bottom log-log plot along with the data (black).

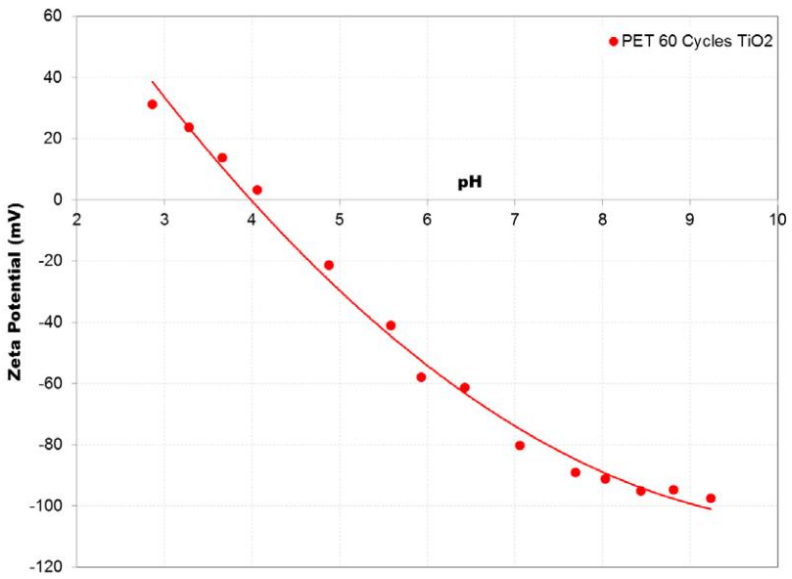

Figure A11. Zeta potential versus pH for the 3D nm-thin membrane.

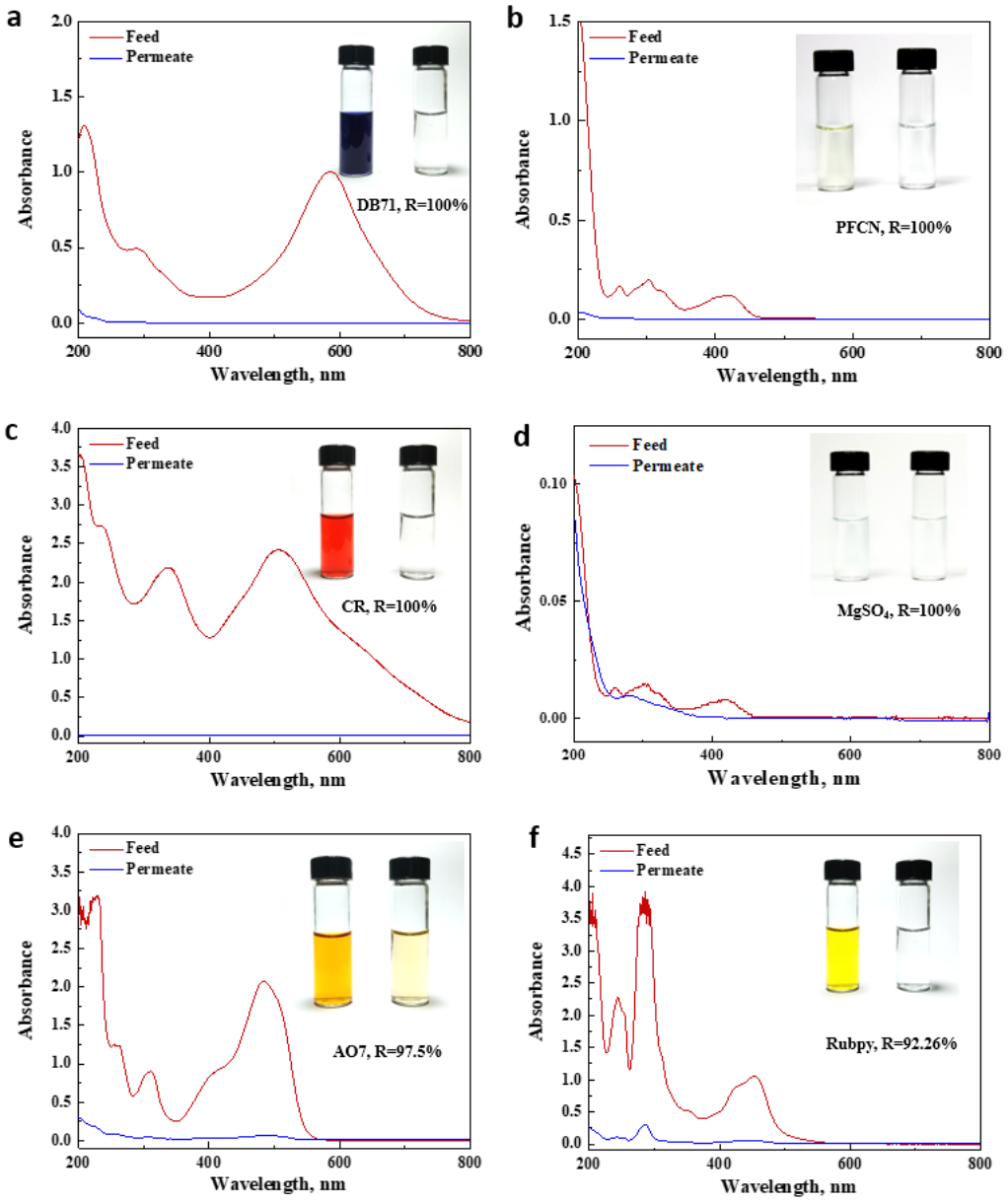

Figure A12. UV-vis spectroscopy and photos of the feed and permeation solution for the diffusion test.

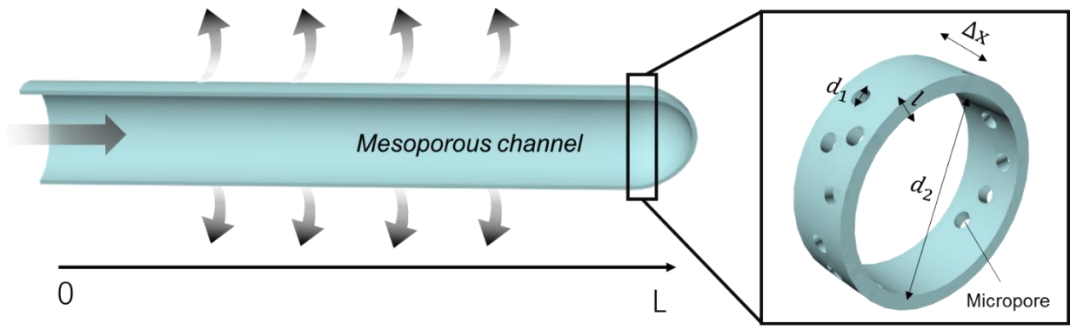

Figure A13. Schematic for the calculation of mass transport through mesoporous channels and micropores in 3DM.

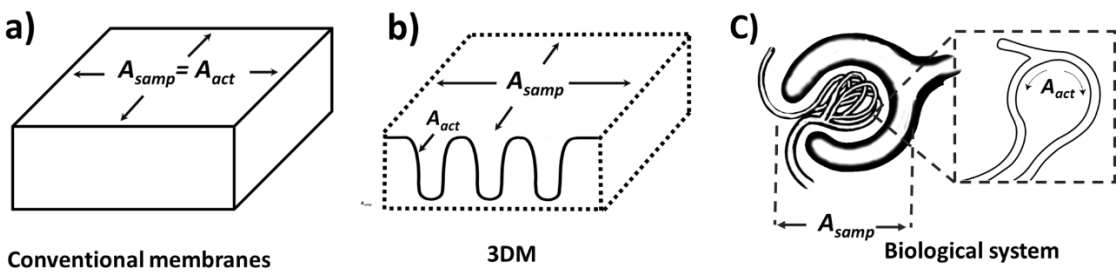

Figure A14. Schematic diagram for determining the active surface area of (a) conventional membranes, (b) 3DM, and (c) biological systems. A_{act} and A_{samp} refer to the actual membrane area and sample area (projection area), respectively**.**

APPENDIX D. METHODS

Rejection ratio estimation from Donnan theory

The rejection ratio based on Donnan theory was estimated using the following Equation[170]:

S1)
$$\mathrm{R} = 1 - \frac{c_i^m}{\mathrm{c}_i} = 1 - \left(\frac{|z_i|c_i}{|z_i|c_i^m + c_x^m}\right)^{\left|{}^{z_i}/_{z_j}\right|}$$

where, R is the rejection coefficient, $\mathrm{C_i}$ is the co-ion concentration in the solution, C_i^m is the co-ion concentration in the membrane, c_x^m is the charge concentration of the membrane, $\mathrm{z_i}$ and $\mathrm{z_i}$ are the valance of co-ions and counterions respectively.

Small Angle X-ray Scattering (SAXS) modeling

Based on TEM and N_2 desorption results, the dominant scattering morphology is expected to be from the straight-line sections of the tubes that have wall thicknesses and internal heterogeneities between 1 nm and 12 nm. To a first approximation, the SAXS data can be modeled as a system of simple concentric cylinders[158] by the equations:

S2)
$$I_{CC}(q, R, t_{wall}) = \int_0^{\pi/2} \left[\sum_{i=0}^{i=N} \left[[\rho(r_i) - \rho(r_{i+1})]V(r_i, L)G(q, \alpha, r_i, L)\right]^2\right] \sin\beta \, d\beta$$

S3)
$$G(q, \beta, r, L) = 2\left[\frac{\sin qL\cos\beta}{qL\cos\beta}\right]\left[\frac{J_1(qr\sin\beta)}{qr\sin\beta}\right]$$

S4)
$$V(r) = \pi r^2 2L$$

S5)
$$\rho(r) = \begin{cases} \rho_{pore} & r \le R \\ \rho_{TiO_2} & R < r \le R + t_{wall} \\ \rho_{pore} & r > R + t_{wall} \end{cases}$$

where $V(r,L)$ is the volume of a cylinder with radius r and length $2L$ and the function $\rho(r)$ represents the scattering length density normal to the cylinder length axis with $r = 0$ at the cylinder center and $r = R$ at cylinder outer surface. The function $G(q,\beta,r,L)$ is the normalized scattering amplitude of a cylinder of revolution with radius r and length, $2L$.[152] For the case of a tube with a completely homogenous wall, the

function $\rho(r)$ is a simple Heaviside function that has a width equal to the wall thickness. Based on the N_2 desorption results (Fig. 2C), there is a size distribution of the inner tube radii, which are assumed to be Gaussian distribution, $D_R(R, \bar{R}, \sigma)$, that has a mean radius of 17.5 nm and a full-width-at-half-maximum (FWHM) equal to 7.8 nm (σ = 0.19). We note that the SAXS model is somewhat insensitive to these parameters since the pore radii dominate the scattering at lower-q values not measured. Therefore, the scattered intensity from a system tubes that have a size distribution of inner radii is calculated by the equation:

S6)
$$I_{TiO2}(q) = K \sum_{R=0.5\bar{R}}^{R=2\bar{R}} \frac{I_{CC}(q, R, L, t_{wall}(R)}{V(R, L)} D_R(R, \bar{R}, \sigma)\, \Delta R + b$$

S7)
$$t_{wall}(R) = \overline{t_{wall}} + (R - \bar{R}) \frac{\overline{t_{wall}}}{\bar{R}} f$$

where K is a constant that is proportional to the total volume fraction of cylinders and contrast, b is the flat background and the intensity is normalized by the volume of the cylinder so that the Gaussian function, $D_R(R, \bar{R}, \sigma)$, is the volume distribution.[221] While Equation S6 is somewhat insensitive to the size distribution of inner tube radii (within reason), the size distribution of wall thicknesses will significantly affect the shape of $I_{TiO2}(q)$. Therefore, a fractional standard deviation parameter, f, is used in Equation S7 to calculate the size distribution of wall thicknesses. When $f < 1$, the FWHM of the distribution in t_{wall} is a narrower fraction of the mean compared to the inner pore radius. In total, there are four parameters: K, $\overline{t_{wall}}$, f and b that are fit to the data using the lmfit[222] package for python. From the model fitting, the values of $\overline{t_{wall}}$ and f were found to be 8.3 nm and 0.25 , respectively; a value of 0.25 for f, corresponds to a FWHM slightly less than 1 nm. There is very high certainty in the value of both f and $\overline{t_{wall}}$, as small changes in the size distribution significantly affects the model and shown in Supplementary Fig 1. Based on the model sensitivity to the parameters $\overline{t_{wall}}$ and f in Supplementary Fig. 1, we conclude from the SAXS data that wall thicknesses between 7.8 nm and 8.8 nm dominate irradiated volume of the TiO_2 tubular network; this corresponds to a variation in $\overline{t_{wall}}$ of ± 6 %.

While the overall wall thickness can be resolved well with simple least squares fitting of Equation S6, there is some slight misfit at $q > 0.15$ Å^{-1}, which suggest the presence of scattering heterogeneities that are smaller than the wall thickness (sizes less than ~ 4 nm); the model fit cannot be accounted for by simple addition of an extra Guinier region, as no clear Guinier knee is present at high-q. With the assumption that such heterogeneities can only exist inside the tube wall, a simulated annealing algorithm[223] can be employed to determine if: 1) heterogeneities within the shell can account for the misfit and 2) whether the heterogeneities are likely to exist at specific locations within the tube wall (e.g. concentrated in the middle, near the surface or are uniform). Unlike the case of a spherically symmetric phase, the simulated annealing performed here necessarily assumes the heterogeneities are relatively uniform parrallel to the surface. While this assumption cannot be verified, the simulated annealing procedure can determine if and where heterogeneities perpendicular to the surface can account for at least some of the misfit between the data and homogenous shell model (Equation S6).

The simulated annealing procedure, as implemented in the «simanneal»[224] package for python, randomly perturbs the initial heaviside function in Equation S5, $\rho(r)$, and evaluates the change in χ^2. Each move is evaluated and accepted depending on the unitless temperature and the change in χ^2 compared with the previous value. Details of this procedure can be found in prior work.[223] In this study, 100 points were randomly chosen within the wall. At each step, the function $\rho(r)$ was perturbed by a Gaussian function with a randomly chosen standard deviation between 1 and 10 and integrated area between 0 and 0.5. A total of 10000 iterations were made using temperature schedules starting from 1000 to 2000 and ending at 0.1. These simulations were performed using a computer with a 3.6 GHz Intel Xeon E5 Quad-Core processor and 32 GB of memory. Typical simulation times were ~ 150 hours. Based on the results from four simulations (Supplementary Fig 2), we conclude that wall heterogeneity perpendicular to the surface does improve the model fit. Moreover, the heterogeneity is consistently highest near the inner and outter surfaces, regardless of the annealing temperature and starting conditions.

Surface charge calculations

The surface charge can be calculated based on the following Equation:

S8)
$$\sigma = \sqrt{8\varepsilon_0\varepsilon_r RTc}\sinh\left(-\frac{F\xi}{2RT}\right)$$

where ε_0 is the permittivity of vacuum, ε_r is the dielectric coefficient of the solution, R is the gas constant, T the temperature (K), c the solute concentration, and F is the Faraday's constant.

Calculation for pore density, gas flux, water permeance and transport resistance

The areal pore density was estimated based on three different areas on the high resolution TEM images of 3DM. Knudsen diffusion model is applied to predict the gas flux and compare with our experiment result. The flow rate of the gas in the Knudsen region can be expressed by Equation S9 [225]:

S9)
$$Q_{gas} = \frac{2}{3}\sqrt{\frac{8\pi}{MRT}}(r)^3 V_m \frac{\Delta P}{L}\sigma A$$

Where Q_{gas} is the gas flow rate, M is the gas molecular weight, R is the ideal gas constant, T is the temperature in Kelvin, r is the radius of the pore, ΔP is the pressure drop across the membrane, L is the membrane thickness, σ is the areal pore density and A is the total area of the membrane. Here, σA can also be calculated by multiply the volumetric pore density and the total volume of the membrane.

The following assumptions are used for this calculation: 1. The gas flux through the meso-porous channels (~30 nm) and micropores (~1 nm) are all in Knudsen region. 2. The gases are considered as incompressible. 3. Assuming system is in steady state.

Since the gas is transported from both the mesoporous channels (~30 nm dia.) and the micro-pores on the TiO_2 walls (~1.1 nm). The mass balance between these two regions must be considered (Supplementary Fig. 5).

S10)
$$Q = \frac{2}{3}\sqrt{\frac{8\pi}{MRT}}\left(\frac{d_2}{2}\right)^3 V_m \frac{\Delta \mathrm{P}}{\Delta \mathrm{x}} = \int_x^L q = \int_x^L \frac{2}{3}\sqrt{\frac{8\pi}{MRT}}\left(\frac{d_1}{2}\right)^3 V_m \frac{P}{l}\sigma\pi d_2 \Delta \mathrm{x}$$

where Q is the gas flux inside the mesoporous channel, q is the gas flux through each micro-pore on the wall, d_1 is the diameter of the micropores, d_2 is the diameter of the mesoporous channel, P is the pressure at position x inside the channel, L is the total length of the channel, l is the wall thickness.

The pore size and pore density of the mesopores and micropores are determined from SEM and high resolution TEM images. The effective channel length (640 μm) was calculated by multiply the membrane thickness (200 μm) with the tortuosity factor (3.2).

The water permeance was calculated via Hagen-Poiseuille equation:

S11)
$$Q = \frac{\pi (r)^4 \Delta P}{8\mu L}$$

Where, Q is the gas flow rate, r is the pore radius, ΔP is the pressure drop across the membrane, μ is the water viscosity, and L is the membrane thickness. Similar to the calculation for gas flux, the mass balance between the water flux inside mesoporous channels and micropores is considered here.

To evaluate the individual effect of mesoporous channels and micropores on the gas and water transport, we estimate the mass transfer resistance from Knudsen and Hagen-Poiseuille equation (Supplementary Table 3). For a general mass transfer process, the flux can be represented as the ratio of driving force (concentration gradience, pressure difference etc.) to the total mass transfer resistance [226]. Therefore, $\left(\frac{2}{3}\sqrt{\frac{8\pi}{MRT}}(r)^3 \frac{V_m}{L}\right)^{-1}$ was used to estimate the mass transfer resistance of single pore from Knudsen equation and $\left(\frac{\pi (r)^4}{8\mu L}\right)^{-1}$ from Hagen-Poiseuille equation. Both variables have the unit of Pa·s/m^3. It needs to be mentioned that the information reflected by the mass transfer resistance is more qualitative rather than quantitative, since the real mass transfer process is quite complicated and often influenced by several conjugated factors.

Effective surface area calculation (ESA)

The effective surface area of the 3DM, two commercial membranes (NF 270 and Biomax 30), two lab-made membranes (GO-framework and PVDF-Al_2O_3), and kidney glomerulus using the following formula [227]:

S12)
$$\text{Effective surface area [\%]} = \frac{A_{act}}{A_{samp}} \times 100$$

The actual surface area (A_{act}) represents actual membrane surface area that contributes to the mass transport and the sample area (A_{samp}) represent the footprint area. For the GO-framework [166], PVDF-Al_2O_3 [228], and commercial membranes, the actual surface area and sample area are equal (Supplementary Fig. 6a), therefore giving an effective surface area close to 100%. For 3DM and biological systems (kidney), the total mass transfer rate is contributed by each channel inside the membrane. Hence, the topography of these membranes should be considered during the calculation (Supplementary Fig. 6 b,c). Parameters for the calculation and the effective surface area values are listed in Supplementary Table 4.

Reference

[1] L. Lu, X. Han, J. Li, J. Hua, M. Ouyang, *J. Power Sources* **2013**, 226, 272.
[2] B. Dunn, H. Kamath, J.-M. Tarascon, *Science* **2011**, 334, 928.
[3] W. Wang, Q. Luo, B. Li, X. Wei, L. Li, Z. Yang, *Adv. Funct. Mater.* **2013**, 23, 970.
[4] M. M. Thackeray, C. Wolverton, E. D. Isaacs, *Energy & Environmental Science* **2012**, 5, 7854.
[5] S. Kim, T. B. Tighe, B. Schwenzer, J. Yan, J. Zhang, J. Liu, Z. Yang, M. A. Hickner, *J. Appl. Electrochem.* **2011**, 41, 1201.
[6] C. Sun, J. Chen, H. Zhang, X. Han, Q. Luo, *J. Power Sources* **2010**, 195, 890.
[7] X. Teng, Y. Zhao, J. Xi, Z. Wu, X. Qiu, L. Chen, *J. Power Sources* **2009**, 189, 1240.
[8] J. Zeng, C. Jiang, Y. Wang, J. Chen, S. Zhu, B. Zhao, R. Wang, *Electrochemistry Communications* **2008**, 10, 372.
[9] D. Qin, Z. Liu, H. Bai, D. D. Sun, X. Song, *Scientific reports* **2016**, 6, 24365.
[10] H. Cong, M. Radosz, B. F. Towler, Y. Shen, *Separation and Purification Technology* **2007**, 55, 281.
[11] Z. Liu, B. Guo, J. Huang, L. Hong, M. Han, L. M. Gan, *Journal of power sources* **2006**, 157, 207.
[12] C. H. Park, S. Y. Lee, D. S. Hwang, D. W. Shin, D. H. Cho, K. H. Lee, T.-W. Kim, T.-W. Kim, M. Lee, D.-S. Kim, *Nature* **2016**, 532, 480.
[13] G. He, Z. Li, J. Zhao, S. Wang, H. Wu, M. D. Guiver, Z. Jiang, *Advanced Materials* **2015**, 27, 5280.
[14] Z. Yang, J. Zhang, M. C. Kintner-Meyer, X. Lu, D. Choi, J. P. Lemmon, J. Liu, *Chemical reviews* **2011**, 111, 3577.
[15] T. Nguyen, R. F. Savinell, *The Electrochemical Society Interface* **2010**, 19, 54.
[16] M. Chakrabarti, R. Dryfe, E. Roberts, *Electrochimica Acta* **2007**, 52, 2189.
[17] A. Parasuraman, T. M. Lim, C. Menictas, M. Skyllas-Kazacos, *Electrochimica Acta* **2013**, 101, 27.
[18] A. Z. Weber, M. M. Mench, J. P. Meyers, P. N. Ross, J. T. Gostick, Q. Liu, *J. Appl. Electrochem.* **2011**, 41, 1137.
[19] X. Li, H. Zhang, Z. Mai, H. Zhang, I. Vankelecom, *Energy Environ. Sci* **2011**, 4, 1147.
[20] B. Schwenzer, J. Zhang, S. Kim, L. Li, J. Liu, Z. Yang, *ChemSusChem* **2011**, 4, 1388.
[21] L. THALLER, "Ninth intersoc. energy conv", presented at *NASA Lewis Research Center, Cleveland, US (NASA TM X-71540) Eng. Conf, San Francisco, CA: August, 26-30, 1974: 924-928*, 1974.
[22] Y. Zeng, T. Zhao, L. An, X. Zhou, L. Wei, *J. Power Sources* **2015**, 300, 438.
[23] J. McBreen, E. Gannon, *Journal of The Electrochemical Society* **1983**, 130, 1667.
[24] G. P. Rajarathnam, A. M. Vassallo, *The Zinc/Bromine Flow Battery: Materials Challenges and Practical Solutions for Technology Advancement*, Springer, 2016.
[25] M. Wu, T. Zhao, H. Jiang, Y. Zeng, Y. Ren, *J. Power Sources* **2017**, 355, 62.
[26] Q. Lai, H. Zhang, X. Li, L. Zhang, Y. Cheng, *Journal of Power Sources* **2013**, 235, 1.
[27] P. C. Butler, P. A. Eidler, P. G. Grimes, S. E. Klassen, R. C. Miles, McGraw-Hill: Ohio, 2001, 37.
[28] T. Nguyen, R. F. Savinell, *Electrochemical Society Interface* **2010**, 19, 54.
[29] M. Skyllas-Kazacos, M. Rychcik, R. G. Robins, A. Fane, M. Green, *J. Electrochem. Soc.* **1986**, 133, 1057.
[30] P. Zhao, H. Zhang, H. Zhou, J. Chen, S. Gao, B. Yi, *J. Power Sources* **2006**, 162, 1416.
[31] M. Skyllas-Kazacos, M. Chakrabarti, S. Hajimolana, F. Mjalli, M. Saleem, *J. Chem. SOC., Faraday Trans.* **2011**, 158, R55.
[32] M. Zhang, M. Moore, J. Watson, T. A. Zawodzinski, R. M. Counce, *J. Electrochem. Soc.* **2012**, 159, A1183.
[33] M. Johnson, "Gridscale rampable intermittent dispatchable storage (grids) program", presented at *DOE annual storage R&D review meeting*, 2010.

[34] V. Viswanathan, A. Crawford, D. Stephenson, S. Kim, W. Wang, B. Li, G. Coffey, E. Thomsen, G. Graff, P. Balducci, *J. Power Sources* **2014**, 247, 1040.
[35] L. Li, S. Kim, W. Wang, M. Vijayakumar, Z. Nie, B. Chen, J. Zhang, G. Xia, J. Hu, G. Graff, *Advanced Energy Materials* **2011**, 1, 394.
[36] Z. González, C. Botas, P. Álvarez, S. Roldán, C. Blanco, R. Santamaría, M. Granda, R. Menéndez, *Carbon* **2012**, 50, 828.
[37] Z. González, S. Vizireanu, G. Dinescu, C. Blanco, R. Santamaría, *Nano Energy* **2012**, 1, 833.
[38] Z. González, A. Sánchez, C. Blanco, M. Granda, R. Menéndez, R. Santamaría, *Electrochem. commun.* **2011**, 13, 1379.
[39] J.-Z. Chen, W.-Y. Liao, W.-Y. Hsieh, C.-C. Hsu, Y.-S. Chen, *J. Power Sources* **2015**, 274, 894.
[40] X. Wu, H. Xu, Y. Shen, P. Xu, L. Lu, J. Fu, H. Zhao, *Electrochimica Acta* **2014**, 138, 264.
[41] J. A. Kowalski, L. Su, J. D. Milshtein, F. R. Brushett, *Current Opinion in Chemical Engineering* **2016**, 13, 45.
[42] Z. Li, S. Li, S. Liu, K. Huang, D. Fang, F. Wang, S. Peng, *Electrochemical and Solid State Letters* **2011**, 14, A171.
[43] F. R. Brushett, J. T. Vaughey, A. N. Jansen, *Adv. Energy Mater.* **2012**, 2, 1390.
[44] T. Liu, X. Wei, Z. Nie, V. Sprenkle, W. Wang, *Advanced Energy Materials* **2016**, 6, 1501449.
[45] B. Huskinson, M. P. Marshak, C. Suh, S. Er, M. R. Gerhardt, C. J. Galvin, X. Chen, A. Aspuru-Guzik, R. G. Gordon, M. J. Aziz, *Nature* **2014**, 505, 195.
[46] B. Yang, L. Hoober-Burkhardt, F. Wang, G. S. Prakash, S. Narayanan, *Journal of The Electrochemical Society* **2014**, 161, A1371.
[47] Y. Matsuda, K. Tanaka, M. Okada, Y. Takasu, M. Morita, T. Matsumura-Inoue, *J. Appl. Electrochem.* **1988**, 18, 909.
[48] P. Leung, C. Ponce-de-Leon, C. Low, A. Shah, F. Walsh, *J. Power Sources* **2011**, 196, 5174.
[49] Y. Yang, G. Zheng, Y. Cui, *Energy & Environmental Science* **2013**, 6, 1552.
[50] T. Janoschka, N. Martin, U. Martin, C. Friebe, S. Morgenstern, H. Hiller, M. D. Hager, U. S. Schubert, *Nature* **2015**, 527, 78.
[51] W. Y. Hsu, T. D. Gierke, *Journal of Membrane Science* **1983**, 13, 307.
[52] J. Xi, Z. Wu, X. Qiu, L. Chen, *J. Power Sources* **2007**, 166, 531.
[53] X. Teng, Y. Zhao, J. Xi, Z. Wu, X. Qiu, L. Chen, *J. Membr. Sci.* **2009**, 341, 149.
[54] L. Yu, F. Lin, L. Xu, J. Xi, *RSC Adv.* **2016**, 6, 3756.
[55] S. J. Peighambardoust, S. Rowshanzamir, M. Amjadi, *International journal of hydrogen energy* **2010**, 35, 9349.
[56] M. Skyllas‐Kazacos, F. Grossmith, *Journal of the Electrochemical Society* **1987**, 134, 2950.
[57] G.-J. Hwang, H. Ohya, *J. Membr. Sci.* **1996**, 120, 55.
[58] R. Gloukhovski, V. Freger, Y. Tsur, *Reviews in Chemical Engineering* **2018**, 34, 455.
[59] M. A. Hickner, H. Ghassemi, Y. S. Kim, B. R. Einsla, J. E. McGrath, *Chemical reviews* **2004**, 104, 4587.
[60] R. Gloukhovski, Y. Tsur, V. Freger, *Fuel Cells* **2017**, 17, 56.
[61] Z. Xu, I. Michos, X. Wang, R. Yang, X. Gu, J. Dong, *Chemical Communications* **2014**, 50, 2416.
[62] X. Lin, S. Kim, D. M. Zhu, E. Shamsaei, T. Xu, X. Fang, H. Wang, *Journal of Membrane Science* **2017**, 524, 557.
[63] T. Wang, F. Sun, H. Wang, S. Yang, L. Fan, *Polymer* **2012**, 53, 3154.
[64] K. H. Gopi, S. G. Peera, S. Bhat, P. Sridhar, S. Pitchumani, *international journal of hydrogen energy* **2014**, 39, 2659.
[65] A. Jasti, V. K. Shahi, *Journal of Materials Chemistry A* **2013**, 1, 6134.
[66] J. Wang, Z. Zhao, F. Gong, S. Li, S. Zhang, *Macromolecules* **2009**, 42, 8711.
[67] Q. Li, L. Liu, S. Liang, Q. Dong, B. Jin, R. Bai, *RSC Advances* **2013**, 3, 13477.

[68] O. D. Thomas, K. J. Soo, T. J. Peckham, M. P. Kulkarni, S. Holdcroft, *Polymer Chemistry* **2011**, 2, 1641.
[69] Y. Li, T. Xu, M. Gong, *Journal of membrane science* **2006**, 279, 200.
[70] K. K. Stokes, J. A. Orlicki, F. L. Beyer, *Polymer Chemistry* **2011**, 2, 80.
[71] J. Ran, L. Wu, Q. Ge, Y. Chen, T. Xu, *Journal of Membrane Science* **2014**, 470, 229.
[72] Z. Zhang, L. Wu, J. Varcoe, C. Li, A. L. Ong, S. Poynton, T. Xu, *Journal of Materials Chemistry A* **2013**, 1, 2595.
[73] H. Zhang, H. Zhang, X. Li, Z. Mai, J. Zhang, *Energy & Environmental Science* **2011**, 4, 1676.
[74] H. Zhang, H. Zhang, X. Li, Z. Mai, W. Wei, *Energy & Environmental Science* **2012**, 5, 6299.
[75] R. Yang, Z. Xu, S. Yang, I. Michos, L.-F. Li, A. P. Angelopoulos, J. Dong, *J. Membr. Sci.* **2014**, 450, 12.
[76] T. Luo, O. David, Y. Gendel, M. Wessling, *J. Power Sources* **2016**, 312, 45.
[77] Z. Jian, Y. S. Hu, X. Ji, W. Chen, *Adv. Mater.* **2017**, 29, 1601925.
[78] S. Hasegawa, N. Imanishi, T. Zhang, J. Xie, A. Hirano, Y. Takeda, O. Yamamoto, *J. Power Sources* **2009**, 189, 371.
[79] X. Yu, Z. Bi, F. Zhao, A. Manthiram, *Advanced Energy Materials* **2016**, 6, 1601392.
[80] W. Lu, Z. Yuan, Y. Zhao, H. Zhang, H. Zhang, X. Li, *Chem. Soc. Rev.* **2017**, 46, 2199.
[81] K. Schmidt-Rohr, Q. Chen, in *Materials For Sustainable Energy: A Collection of Peer-Reviewed Research and Review Articles from Nature Publishing Group*, World Scientific, 2011, 238.
[82] M. Eikerling, A. Kornyshev, A. Kuznetsov, J. Ulstrup, S. Walbran, *The Journal of Physical Chemistry B* **2001**, 105, 3646.
[83] M. Eikerling, A. Kornyshev, U. Stimming, *The Journal of Physical Chemistry B* **1997**, 101, 10807.
[84] K. Knehr, E. Agar, C. Dennison, A. Kalidindi, E. Kumbur, *Journal of The Electrochemical Society* **2012**, 159, A1446.
[85] Á. Cunha, J. Martins, N. Rodrigues, F. Brito, *International Journal of Energy Research* **2015**, 39, 889.
[86] S. Maurya, S.-H. Shin, Y. Kim, S.-H. Moon, *Rsc Advances* **2015**, 5, 37206.
[87] J. Miyake, K. Miyatake, *Polymer Journal* **2017**, 49, 487.
[88] L. Chen, S. Zhang, Y. Chen, X. Jian, *Journal of Power Sources* **2017**, 355, 23.
[89] W.-H. Lee, Y. S. Kim, C. Bae, *ACS Macro Letters* **2015**, 4, 814.
[90] W.-H. Lee, E. J. Park, J. Han, D. W. Shin, Y. S. Kim, C. Bae, *ACS Macro Lett.* **2017**, 6, 566.
[91] B. Jiang, L. Wu, L. Yu, X. Qiu, J. Xi, *J. Membr. Sci.* **2016**, 510, 18.
[92] M. Rychcik, M. Skyllas-Kazacos, *J. Power Sources* **1988**, 22, 59.
[93] J. Tolliday, E. Woods, E. Hartung, *Transactions of the Faraday Society* **1949**, 45, 148.
[94] T. Mohammadi, M. S. Kazacos, *J. Appl. Electrochem.* **1997**, 27, 153.
[95] J.-D. Chai, M. Head-Gordon, *Phys. Chem. Chem. Phys.* **2008**, 10, 6615.
[96] A. McLean, G. Chandler, *J. Chem. Phys.* **1980**, 72, 5639.
[97] M. M. Francl, W. J. Pietro, W. J. Hehre, J. S. Binkley, M. S. Gordon, D. J. DeFrees, J. A. Pople, *J. Chem. Phys.* **1982**, 77, 3654.
[98] P. J. Hay, W. R. Wadt, *J. Chem. Phys.* **1985**, 82, 299.
[99] L. E. Roy, P. J. Hay, R. L. Martin, *J. Chem. Theory Comput.* **2008**, 4, 1029.
[100] A. Ehlers, M. Böhme, S. Dapprich, A. Gobbi, A. Höllwarth, V. Jonas, K. Köhler, R. Stegmann, A. Veldkamp, G. Frenking, *Chem. Phys. Lett.* **1993**, 208, 111.
[101] X. Ling, C. Jia, J. Liu, C. Yan, *J. Membr. Sci.* **2012**, 415-416, 306.
[102] J. Si, Y. Lv, S. Lu, Y. Xiang, *J. Power Sources* **2019**, 428, 88.
[103] C. Li, A. L. Ward, S. E. Doris, T. A. Pascal, D. Prendergast, B. A. Helms, *Nano Lett.* **2015**, 15, 5724.
[104] A. Münchinger, K.-D. Kreuer, *J. Membr. Sci.* **2019**, 592, 117372.
[105] A. Münchinger, T. Wang, S. Kim, K.-D. Kreuer, *In Preparation* **2019**.

[106] I. S. Chae, T. Luo, G. H. Moon, W. Ogieglo, Y. S. Kang, M. Wessling, *Adv. Energy Mater.* **2016**, 6, 1600517.
[107] K.-D. Kreuer, S. J. Paddison, E. Spohr, M. Schuster, *Chemical Reviews* **2004**, 104, 4637.
[108] K.-D. Kreuer, G. Portale, *Adv. Funct. Mater.* **2013**, 23, 5390.
[109] K. R. Hinkle, C. J. Jameson, S. Murad, *J. Phys. Chem. C* **2014**, 118, 23803.
[110] X. Wu, J. Wang, S. Liu, X. Wu, S. Li, *Electrochimica Acta* **2011**, 56, 10197.
[111] C. Choi, S. Kim, R. Kim, Y. Choi, S. Kim, H.-y. Jung, J. H. Yang, H.-T. Kim, *Renewable and Sustainable Energy Reviews* **2017**, 69, 263.
[112] H.-J. Schneider, *Chemical Science* **2012**, 3, 1381.
[113] Q. Dai, Z. Liu, L. Huang, C. Wang, Y. Zhao, Q. Fu, A. Zheng, H. Zhang, X. Li, *Nature Communications* **2020**, 11, 13.
[114] D. Chen, M. A. Hickner, E. Agar, E. C. Kumbur, *Electrochemistry Communications* **2013**, 26, 37.
[115] H.-S. Dang, E. A. Weiber, P. Jannasch, *J. Mater. Chem. A* **2015**, 3, 5280.
[116] D. Chen, M. A. Hickner, *ACS Appl. Mater. Interfaces* **2012**, 4, 5775.
[117] Y. Li, X. Lin, L. Wu, C. Jiang, M. M. Hossain, T. Xu, *J. Membr. Sci.* **2015**, 483, 60.
[118] F. Huang, L. Hou, H. Wu, X. Wang, H. Shen, W. Cao, W. Yang, Y. Cao, *J. Am. Chem. Soc.* **2004**, 126, 9845.
[119] H. G. Kim, R. Kim, S. Kim, C. Choi, B. Kim, H. Guim, H.-T. Kim, *Journal of industrial and engineering chemistry* **2018**, 60, 401.
[120] M. S. Cha, J. Y. Lee, T.-H. Kim, H. Y. Jeong, H. Y. Shin, S.-G. Oh, Y. T. Hong, *J. Membr. Sci.* **2017**, 530, 73.
[121] T. Wang, S. J. Moon, D.-S. Hwang, H. Park, J. Lee, S. Kim, Y. M. Lee, S. Kim, *J. Membr. Sci.* **2019**, 583, 16.
[122] D. Zhang, X. Yan, G. He, L. Zhang, X. Liu, F. Zhang, M. Hu, Y. Dai, S. Peng, *J. Mater. Chem. A* **2015**, 3, 16948.
[123] S. Peng, X. Yan, D. Zhang, X. Wu, Y. Luo, G. He, *RSC Adv.* **2016**, 6, 23479.
[124] Z. Li, W. Dai, L. Yu, L. Liu, J. Xi, X. Qiu, L. Chen, *ACS Appl. Mater. Interfaces* **2014**, 6, 18885.
[125] D. Chen, S. Wang, M. Xiao, Y. Meng, *Energy & Environmental Science* **2010**, 3, 622.
[126] D. W. Shin, M. D. Guiver, Y. M. Lee, *Chemical reviews* **2017**, 117, 4759.
[127] H. Zhang, H. Zhang, X. Li, Z. Mai, W. Wei, *Energy Environmental Science* **2012**, 5, 6299.
[128] S. Hu, M. Lozada-Hidalgo, F. C. Wang, A. Mishchenko, F. Schedin, R. R. Nair, E. W. Hill, D. W. Boukhvalov, M. I. Katsnelson, R. A. W. Dryfe, I. V. Grigorieva, H. A. Wu, A. K. Geim, *Nature* **2014**, 516, 227.
[129] A. Manthiram, Y. Fu, S.-H. Chung, C. Zu, Y.-S. Su, *Chemical reviews* **2014**, 114, 11751.
[130] X. Zhou, T. Zhao, L. An, Y. Zeng, L. Wei, *J. Power Sources* **2017**, 339, 1.
[131] Z. W. Seh, Y. Sun, Q. Zhang, Y. Cui, *Chem. Soc. Rev.* **2016**, 45, 5605.
[132] L. Qie, C. Zu, A. Manthiram, *Adv. Energy Mater.* **2016**, 6, 1502459.
[133] H. Chen, G. Cong, Y.-C. Lu, *Journal of energy chemistry* **2018**, 27, 1304.
[134] R. M. Darling, A. Z. Weber, M. C. Tucker, M. L. Perry, *J. Chem. SOC., Faraday Trans.* **2015**, 163, A5014.
[135] X. Cheng, W. Wang, A. Wang, K. Yuan, Z. Jin, Y. Yang, X. Zhao, *RSC Adv.* **2016**, 6, 89972.
[136] Q. Xu, G. Hu, H. Bi, H. Xiang, *Ionics* **2015**, 21, 981.
[137] L. Tan, X. Li, Z. Wang, H. Guo, J. Wang, L. An, *ChemElectroChem* **2018**, 5, 71.
[138] Y. Fan, D. Liu, M. M. Rahman, T. Tao, W. Lei, S. Mateti, B. Yu, J. Wang, C. Yang, Y. Chen, *ACS Appl. Energy Mater.* **2019**, 2, 2620.
[139] D. Chen, M. A. Hickner, *Physical Chemistry Chemical Physics* **2013**, 15, 11299.
[140] H. Prifti, A. Parasuraman, S. Winardi, T. M. Lim, M. Skyllas-Kazacos, *Membranes* **2012**, 2, 275.
[141] W. Bao, Z. Zhang, C. Zhou, Y. Lai, J. Li, *J. Power Sources* **2014**, 248, 570.

[142] Y.-S. Su, A. Manthiram, *Nat. Commun.* **2012**, 3, 1.
[143] A. Bohle, B. Aeikens, A. Eenboom, L. Fronholt, W. R. Plate, J. C. Xiao, A. Greschniok, M. Wehrmann, *Kidney international. Supplement* **1998**, 67, S186.
[144] J. Zhao, Q. Deng, A. Bachmatiuk, G. Sandeep, A. Popov, J. Eckert, M. H. Rümmeli, *Science* **2014**, 343, 1228.
[145] B. Mi, *Science* **2014**, 343, 740.
[146] H. W. Kim, H. W. Yoon, S.-M. Yoon, B. M. Yoo, B. K. Ahn, Y. H. Cho, H. J. Shin, H. Yang, U. Paik, S. Kwon, *Science* **2013**, 342, 91.
[147] H. Li, Z. Song, X. Zhang, Y. Huang, S. Li, Y. Mao, H. J. Ploehn, Y. Bao, M. Yu, *Science* **2013**, 342, 95.
[148] S. Karan, Z. W. Jiang, A. G. Livingston, *Science* **2015**, 348, 1347.
[149] Z. Tan, S. Chen, X. Peng, L. Zhang, C. J. S. Gao, *Science* **2018**, 360, 518.
[150] J. Ye, A. C. Baumgaertel, Y. M. Wang, J. Biener, M. M. Biener, *ACS Nano* **2015**, 9, 2194.
[151] M. M. Biener, J. Ye, T. F. Baumann, Y. M. Wang, S. J. Shin, J. Biener, A. V. Hamza, *Adv. Mater.* **2014**, 26, 4808.
[152] A. Guinier, G. Fournet, *Small-angle scattering of X-rays*, Wiley, New York, 1955.
[153] S. Kim, F. Fornasiero, H. G. Park, J. Bin In, E. Meshot, G. Giraldo, M. Stadermann, M. Fireman, J. Shan, C. P. Grigoropoulos, O. Bakajin, *J. Membr. Sci.* **2014**, 460, 91.
[154] A. Pendse, S. Cetindag, M.-H. Lin, A. Rackovic, R. Debbarma, S. Almassi, B. P. Chaplin, V. Berry, J. W. Shan, S. Kim, *Small*, 0, 1904590.
[155] F. Fornasiero, J. Bin In, S. Kim, H. G. Park, Y. Wang, C. P. Grigoropoulos, A. Noy, O. Bakajin, *Langmuir* **2010**, 26, 14848.
[156] N. Y. Yip, A. Tiraferri, W. A. Phillip, J. D. Schiffman, M. Elimelech, *Environ. Sci. Technol.* **2010**, 44, 3812.
[157] S. E. Doris, A. L. Ward, P. D. Frischmann, L. Li, B. A. Helms, *J. Mater. Chem. A* **2016**, 4, 16946.
[158] I. Livsey, *J. Chem. Soc. Faraday Trans.* **1987**, 83, 1445.
[159] M. M. Islam, M. Calatayud, G. Pacchioni, *J. Phys. Chem. C* **2011**, 115, 6809.
[160] K. Sun, M. Kohyama, S. Tanaka, S. Takeda, *J. Phys. Chem. C* **2014**, 118, 1611.
[161] R. M. De Vos, H. Verweij, *Science* **1998**, 279, 1710.
[162] S. Huang, M. Dakhchoune, W. Luo, E. Oveisi, G. He, M. Rezaei, J. Zhao, D. T. Alexander, A. Züttel, M. S. Strano, *Nat. Commun.* **2018**, 9, 2632.
[163] X. Gao, J. C. D. da Costa, S. K. Bhatia, *J. Membr. Sci.* **2013**, 438, 90.
[164] J. K. Holt, H. G. Park, Y. Wang, M. Stadermann, A. B. Artyukhin, C. P. Grigoropoulos, A. Noy, O. Bakajin, *Science* **2006**, 312, 1034
[165] Y.-C. Chiang, Y.-Z. Hsub, R.-C. Ruaan, C.-J. Chuang, K.-L. Tung, *J. Membr. Sci.* **2009**, 326, 19.
[166] Y. Zhang, S. Zhang, T.-S. Chung, *Environ. Sci. Technol.* **2015**, 49, 10235.
[167] L. Ouyang, R. Malaisamy, M. L. Bruening, *J. Membr. Sci.* **2008**, 310, 76.
[168] C. C. Striemer, T. R. Gaborski, J. L. McGrath, P. M. Fauchet, *Nature* **2007**, 445, 749.
[169] K. C. Akratopulu, C. Kordulis, A. Lycourghiotis, *J. Chem. Soc. Faraday Trans.* **1990**, 86, 3437.
[170] F. Fornasiero, H. G. Park, J. K. Holt, M. Stadermann, C. P. Grigoropoulos, A. Noy, O. Bakajin, *Proc. Natl. Acad. Sci. U. S. A.* **2008**, 105, 17250.
[171] H. Huang, Z. Song, N. Wei, L. Shi, Y. Mao, Y. Ying, L. Sun, Z. Xu, X. Peng, *Nat. Commun.* **2013**, 4, 2979.
[172] L. Sun, Y. Ying, H. Huang, Z. Song, Y. Mao, Z. Xu, X. Peng, *ACS nano* **2014**, 8, 6304.
[173] Y. Yang, G. Zheng, Y. Cui, *Chem. Soc. Rev.* **2013**, 42, 3018.
[174] J. Nyengaard, T. Bendtsen, *Anat. Rec.* **1992**, 232, 194.
[175] A. Ruggiero, C. H. Villa, E. Bander, D. A. Rey, M. Bergkvist, C. A. Batt, K. Manova-Todorova, W. M. Deen, D. A. Scheinberg, M. R. McDevitt, *Proc. Natl. Acad. Sci. U. S. A.* **2010**, 107, 12369.
[176] E. Klein, F. Holland, A. Donnaud, A. Lebeouf, K. Eberle, *J. Membr. Sci.* **1977**, 2, 349.

[177] R. Wendt, E. Klein, E. Bresler, F. Holland, R. Serino, H. Villa, *J. Membr. Sci.* **1979**, 5, 23.
[178] P. Zhao, B. Gao, Q. Yue, J. Kong, H. K. Shon, P. Liu, Y. Gao, *Chem. Eng. J.* **2015**, 273, 316.
[179] R. Chang, I. Ueki, J. Troy, W. Deen, C. R. Robertson, B. Brenner, *Biophys. J.* **1975**, 15, 887.
[180] T.-Z. Ren, Z.-Y. Yuan, B.-L. Su, *Colloids Surf. A Physicochem. Eng. Asp.* **2007**, 300, 79.
[181] N. Wang, J. Yu, Z. Zhou, D. Fang, S. Liu, Y. Liu, *J. Membr. Sci.* **2013**, 437, 114.
[182] W. Dai, Y. Shen, Z. Li, L. Yu, J. Xi, X. Qiu, *J. Mater. Chem. A* **2014**, 2, 12423.
[183] D. Chen, S. Wang, M. Xiao, Y. Meng, *Energy Conversion and Management* **2010**, 51, 2816.
[184] L. Ding, X. Song, L. Wang, Z. Zhao, *J. Membr. Sci.* **2019**, 578, 126.
[185] X. Zhou, T. Zhao, L. An, Y. Zeng, X. Zhu, *Applied Energy* **2016**, 180, 353.
[186] W. Xie, R. M. Darling, M. L. Perry, *J. Electrochem. Soc.* **2016**, 163, A5084.
[187] D. Chen, S. Wang, M. Xiao, Y. Meng, *J. Power Sources* **2010**, 195, 2089.
[188] M. S. Cha, S. W. Jo, S. H. Han, S. H. Hong, S. So, T.-H. Kim, S.-G. Oh, Y. T. Hong, J. Y. Lee, *J. Power Sources* **2019**, 413, 158.
[189] S. Yun, J. Parrondo, V. Ramani, *J. Mater. Chem. A* **2014**, 2, 6605.
[190] Y. Chen, S. Zhang, J. Jin, C. Liu, Q. Liu, X. Jian, *ACS Appl. Energy Mater.* **2019**, 2, 8207.
[191] Y. Ahn, D. Kim, *J. Ind. Eng. Chem.* **2019**, 71, 361.
[192] C.-N. Sun, Z. Tang, C. Belcher, T. A. Zawodzinski, C. Fujimoto, *Electrochem. commun.* **2014**, 43, 63.
[193] J. J. Min-suk, J. Parrondo, C. G. Arges, V. Ramani, *J. Mater. Chem. A* **2013**, 1, 10458.
[194] S. Zhang, B. Zhang, D. Xing, X. Jian, *J. Mater. Chem. A* **2013**, 1, 12246.
[195] Z. Mai, H. Zhang, X. Li, C. Bi, H. Dai, *J. Power Sources* **2011**, 196, 482.
[196] F. Zhang, H. Zhang, C. Qu, *J. Phys. Chem. B* **2012**, 116, 9016.
[197] S. Yang, Y. Ahn, D. Kim, *J. Mater. Chem. A* **2017**, 5, 2261.
[198] Y. Zhang, L. Zheng, B. Liu, H. Wang, H. Shi, *J. Membr. Sci.* **2019**, 584, 173.
[199] L. Wang, L. Yu, D. Mu, L. Yu, L. Wang, J. Xi, *J. Membr. Sci.* **2018**, 552, 167.
[200] J. Qiu, M. Zhai, J. Chen, Y. Wang, J. Peng, L. Xu, J. Li, G. Wei, *J. Membr. Sci.* **2009**, 342, 215.
[201] S. Zhang, C. Yin, D. Xing, D. Yang, X. Jian, *J. Membr. Sci.* **2010**, 363, 243.
[202] N. Wang, F. Zhang, R. Zhang, W. Zhou, D. Lu, *Int. J. Electrochem. Sci* **2019**, 14, 5508.
[203] R. Malaisamy, M. L. Bruening, *Langmuir* **2005**, 21, 10587.
[204] G. Zhao, R. Hu, Y. He, H. Zhu, *Advanced Materials Interfaces* **2019**, 1801742.
[205] I. AZELEE, P. Goh, W. Lau, B. Ng, A. Ismail, *Journal of Engineering Science and Technology* **2016**, 11, 974.
[206] Y. Han, Y. Jiang, C. Gao, *ACS applied materials & interfaces* **2015**, 7, 8147.
[207] E. Dražević, K. Košutić, V. Freger, *Water research* **2014**, 49, 444.
[208] H. S. Lee, S. J. Im, J. H. Kim, H. J. Kim, J. P. Kim, B. R. Min, *Desalination* **2008**, 219, 48.
[209] J. Wang, Y. Wang, Y. Zhang, A. Uliana, J. Zhu, J. Liu, B. Van der Bruggen, *ACS applied materials & interfaces* **2016**, 8, 25508.
[210] L. Ding, Y. Wei, Y. Wang, H. Chen, J. Caro, H. Wang, *Angewandte Chemie International Edition* **2017**, 56, 1825.
[211] S. J. Gao, H. Qin, P. Liu, J. Jin, *Journal of Materials Chemistry A* **2015**, 3, 6649.
[212] Q. Yang, Y. Su, C. Chi, C. Cherian, K. Huang, V. Kravets, F. Wang, J. Zhang, A. Pratt, A. Grigorenko, *Nature materials* **2017**, 16, 1198.
[213] L. Huang, J. Chen, T. Gao, M. Zhang, Y. Li, L. Dai, L. Qu, G. Shi, *Adv. Mater.* **2016**, 28, 8669.
[214] Y. Qin, Y. Hu, S. Koehler, L. Cai, J. Wen, X. Tan, W. L. Xu, Q. Sheng, X. Hou, J. Xue, *ACS applied materials & interfaces* **2017**, 9, 9239.
[215] Z. Zhou, Y. Ying, X. Peng, *Applied Materials Today* **2017**, 8, 54.
[216] E. J. Weil, K. V. Lemley, C. C. Mason, B. Yee, L. I. Jones, K. Blouch, T. Lovato, M. Richardson, B. D. Myers, R. G. Nelson, *Kidney Int.* **2012**, 82, 1010.

[217] H. Gundersen, R. Østerby, *Diabetologia* **1977**, 13, 43.
[218] A. Schmitz, H. J. G. Gundersen, R. Østerby, *Diabetes* **1988**, 37, 38.
[219] J. Kroustrup, H. Gundersen, R. Østerby, *Diabetologia* **1977**, 13, 207.
[220] I. Ichikawa, M. L. Purkerson, S. Klahr, J. L. Troy, M. Martinez-Maldonado, B. M. Brenner, *J. clin. Invest.* **1980**, 65, 982.
[221] O. Glatter, O. Kratky, *Small Angle X-Ray Scattering*, Academic Press, New York, New York, U.S.A 1982.
[222] M. Newville, T. Stensitzki, D. B. Allen, A. Ingargiola, *LMFIT: Non-Linear Least-Square Minimization and Curve-Fitting for Python*, Zenodo, 2014.
[223] J. A. Hammons, F. Zhang, J. Ilaysky, *Journal of Colloid and Interface Science* **2018**, 520, 81.
[224] M. Perry, 2017.
[225] J. K. Holt, H. G. Park, Y. Wang, M. Stadermann, A. B. Artyukhin, C. P. Grigoropoulos, A. Noy, O. J. S. Bakajin, *Science* **2006**, 312, 1034.
[226] N. Nonoyama, S. Okazaki, A. Z. Weber, Y. Ikogi, T. Yoshida, *J. Chem. SOC., Faraday Trans.* **2011**, 158, B416.
[227] T. Fujioka, B. E. O'Rourke, K. Michishio, Y. Kobayashi, N. Oshima, H. Kodamatani, T. Shintani, L. D. Nghiem, *J. Membr. Sci.* **2018**, 554, 301.
[228] L. Yan, Y. S. Li, C. B. Xiang, S. Xianda, *J. Membr. Sci.* **2006**, 276, 162.